NASA/CR-2002-211429

Analytical Modeling of Herschel-Quincke Concept Applied to Inlet Turbofan Engines

Raphael F. Hallez and Ricardo A. Burdisso
Virginia Polytechnic Institute and State University
Blacksburg, Virginia

March 2002

The NASA STI Program Office . . . in Profile

Since its founding, NASA has been dedicated to the advancement of aeronautics and space science. The NASA Scientific and Technical Information (STI) Program Office plays a key part in helping NASA maintain this important role.

The NASA STI Program Office is operated by Langley Research Center, the lead center for NASA's scientific and technical information. The NASA STI Program Office provides access to the NASA STI Database, the largest collection of aeronautical and space science STI in the world. The Program Office is also NASA's institutional mechanism for disseminating the results of its research and development activities. These results are published by NASA in the NASA STI Report Series, which includes the following report types:

- TECHNICAL PUBLICATION. Reports of completed research or a major significant phase of research that present the results of NASA programs and include extensive data or theoretical analysis. Includes compilations of significant scientific and technical data and information deemed to be of continuing reference value. NASA counterpart of peer-reviewed formal professional papers, but having less stringent limitations on manuscript length and extent of graphic presentations.

- TECHNICAL MEMORANDUM. Scientific and technical findings that are preliminary or of specialized interest, e.g., quick release reports, working papers, and bibliographies that contain minimal annotation. Does not contain extensive analysis.

- CONTRACTOR REPORT. Scientific and technical findings by NASA-sponsored contractors and grantees.

- CONFERENCE PUBLICATION. Collected papers from scientific and technical conferences, symposia, seminars, or other meetings sponsored or co-sponsored by NASA.

- SPECIAL PUBLICATION. Scientific, technical, or historical information from NASA programs, projects, and missions, often concerned with subjects having substantial public interest.

- TECHNICAL TRANSLATION. English-language translations of foreign scientific and technical material pertinent to NASA's mission.

Specialized services that complement the STI Program Office's diverse offerings include creating custom thesauri, building customized databases, organizing and publishing research results . . . even providing videos.

For more information about the NASA STI Program Office, see the following:

- Access the NASA STI Program Home Page at ***http://www.sti.nasa.gov***

- Email your question via the Internet to help@sti.nasa.gov

- Fax your question to the NASA STI Help Desk at (301) 621-0134

- Telephone the NASA STI Help Desk at (301) 621-0390

- Write to:
  NASA STI Help Desk
  NASA Center for AeroSpace Information
  7121 Standard Drive
  Hanover, MD 21076-1320

NASA/CR-2002-211429

Analytical Modeling of Herschel-Quincke Concept Applied to Inlet Turbofan Engines

Raphael F. Hallez and Ricardo A. Burdisso
Virginia Polytechnic Institute and State University
Blacksburg, Virginia

National Aeronautics and
Space Administration

Langley Research Center
Hampton, Virginia 23681-2199

Prepared for Langley Research Center
under Grant NAG1-2137

March 2002

Available from:

NASA Center for AeroSpace Information (CASI)
7121 Standard Drive
Hanover, MD 21076-1320
(301) 621-0390

National Technical Information Service (NTIS)
5285 Port Royal Road
Springfield, VA 22161-2171
(703) 605-6000

TABLE OF CONTENT

TABLE OF CONTENT 1

ABSTRACT 3

1. INTRODUCTION 5

2. HERSCHELQUINCKE-CONCEPT APPLIED TO INLETS 6

3. ANALYTICAL MODELING - THE INFINITE-DUCT MODEL 7

3.1. MODELING TECHNIQUE 8

3.2. MODAL AMPLITUDES AND TRANSMITTED SOUND POWER 13

3.3. OPTIMIZATION TECHNIQUE USING GENETIC ALGORITHMS 16

3.3.1 Encoding *17*
3.3.2 Fitness function *18*
3.3.3 Selection *19*
3.3.4 Crossover *19*
3.3.5 Mutation *19*
3.3.6 Replacement strategy *20*

3.4. NUMERICAL RESULTS 20

3.4.1 Engine Descriptions *21*
JT15D turbofan engine *21*
TFE731-60 engine *23*
3.4.2 Blade passage frequency results *24*
JT15D engine Results *24*
TFE731-60 engine Results *26*
3.4.3 Broadband results *26*
JT15D engine results *26*
TFE731-60 engine results *29*
3.4.4 Convergence of the predicted results *29*

3.5. NOISE CONTROL MECHANISMS 35

3.5.1 Impedance analysis *36*
3.5.2 Radial scattering *38*
3.5.3 Circumferential Scattering *41*

3.6. ADVANCED HQ SYSTEM CONFIGURATIONS 47

3.6.1 Propagation of modes along a helix *48*
3.6.2 Array in a helix pattern with tubes parallel to the engine axis *50*
3.6.3 Circumferential array with tubes at an angle with respect to the engine axis *56*
3.6.4 Array in a helix pattern with tubes rotated at the same angle *61*

4. ANALYTICAL MODELING-BOUNDARY INTEGRAL METHOD 64

4.1. DESCRIPTION OF TBIEM CODE 64

4.2. MODELING TECHNIQUE 65
4.2.1 Auto and Cross Source Impedance *65*
4.2.2 Average pressure due to fan *70*
4.2.3 Transmitted sound power. *70*
4.3. NUMERICAL RESULTS 71
5. CONCLUSIONS 75
6. RECOMMENDATIONS FOR FUTURE RESEARCH 76
ACKNOWLEDGEMENTS 77
REFERENCES 77
APPENDIX A 78

ABSTRACT

This report presents the key results obtained by the Vibration and Acoustics Laboratories at Virginia Tech over the period from January 1999 to December 2000 on the project "***Investigation of an Adaptive Herschel-Quincke Tube Concept for the Reduction of Tonal and Broadband Noise From Turbofan Engines***" funded by NASA Langley Research Center. The Herschel-Quincke (HQ) tube concept is a developing technique that consists of installing circumferential arrays of HQ tubes around the inlet of a turbofan engine. This research is a continuation of previous efforts in which the HQ concept was preliminarily validated on the JT15D engine [1].

This final project report is organized in three separate reports. The research presented in these reports summarizes both analytical and experimental investigations of the HQ concept for reducing turbofan radiated inlet noise. The analytical part of the project involves two different three-dimensional modeling techniques to provide prediction and design guidelines for the application of the HQ-concept to turbofan engine inlets. First, an infinite-duct model was developed and used to provide insight into the attenuation mechanisms of the HQ systems and design strategies. Second, the NASA-developed TBIEM3D code was modified to allow numerical modeling of HQ systems. This model allows for the investigation of the HQ system when combined within a passive liner. The experimental part of this work includes data for "fixed" HQ tubes on the JT15D engine with different inlet acoustic modal content than previously tested. Experimental results for fixed HQ tubes on a full-scale Honeywell TFE731-60 engine are also presented. Also included here is the first set of results of an experimental investigation into adaptive HQ configuration on the JT15D engine. The parameters of the HQ tubes are changed to optimize the attenuation as the engine speed is changed.

The first report presents the analytical modeling and simulation results. The second report describes the experimental results with both fixed and adaptive HQ-tubes on the JT15D engine. Finally, the third report describes the most important results with fixed tubes on the Honeywell TFE731-60 engine. The three parts of this final report are written such that each part is a complete and separate document that can be reviewed independently from the others.

1. INTRODUCTION

The Herschel-Quincke (HQ) tube concept consists of installing circumferential arrays of HQ tubes around the inlet and/or the bypass duct of a turbofan engine. The application of HQ tubes to turbofan engine inlet noise is a developing technique originally pioneered at Virginia Tech. The research presented in this report is a continuation of previous efforts in which the HQ concept was preliminarily validated on the JT15D engine [1]. The accomplishments of the previous research efforts are summarized in an earlier report [1]. The main previous achievements include:

- Experimental results on the JT15D engine inlet demonstrated blade passage frequency (BPF) tone power attenuation of up to 8 dB with fixed arrays of HQ tubes.
- The HQ tube concept also provides significant attenuation of the broadband component (~ 3 dB power reduction over 0-3200 Hz band.)
- An initial analytical model was developed to investigate the noise control mechanisms of the HQ tube concept and to guide in the design of experiments.

An overview of the tasks involved in this project is shown in Figure 1.1. The project has analytical and experimental components. The analytical part involves the development of two modeling tools for the HQ-tube concept applied to turbofan engine inlets. The experimental part consists of validation of the approach in two engines, i.e. Pratt&Whitney JT15D and Honeywell TFE731-60 engines, for various HQ-tube configurations. The main objectives of this continuing research effort are:

- To further develop modeling techniques for the design, prediction, and optimization of the Herschel-Quincke (HQ) tube concept for application to turbofan engine noise.

- To experimentally investigate both fixed and adaptive HQ-systems for useful reduction of turbofan inlet noise with realistic components on a running turbofan engine.

This final report is organized in three parts devoted to the various components of the research endeavor. This report corresponds to ***Part I,*** which describes the development of analytical tools for the design, prediction, and optimization of HQ-inlet systems. Two analytical models are presented. The first model is based on assuming the inlet to be part of an infinite cylindrical duct. This model was used to investigate the noise control mechanisms associated with the HQ-concept by investigating the effect on the amplitude of the duct modes. A Genetic optimization routine was developed to use in conjunction with the infinite duct model for system design. Finally, this model was used to investigate advanced configurations for the HQ-system. The second model consists of modifying the code TBIEM3D developed at NASA [2] to account for the effect of HQ-arrays. This model has the advantage of considering a finite length duct with the sound field inside

and outside the duct to be fully coupled. In addition, the effect of a lined duct can be easily incorporated in the analysis.

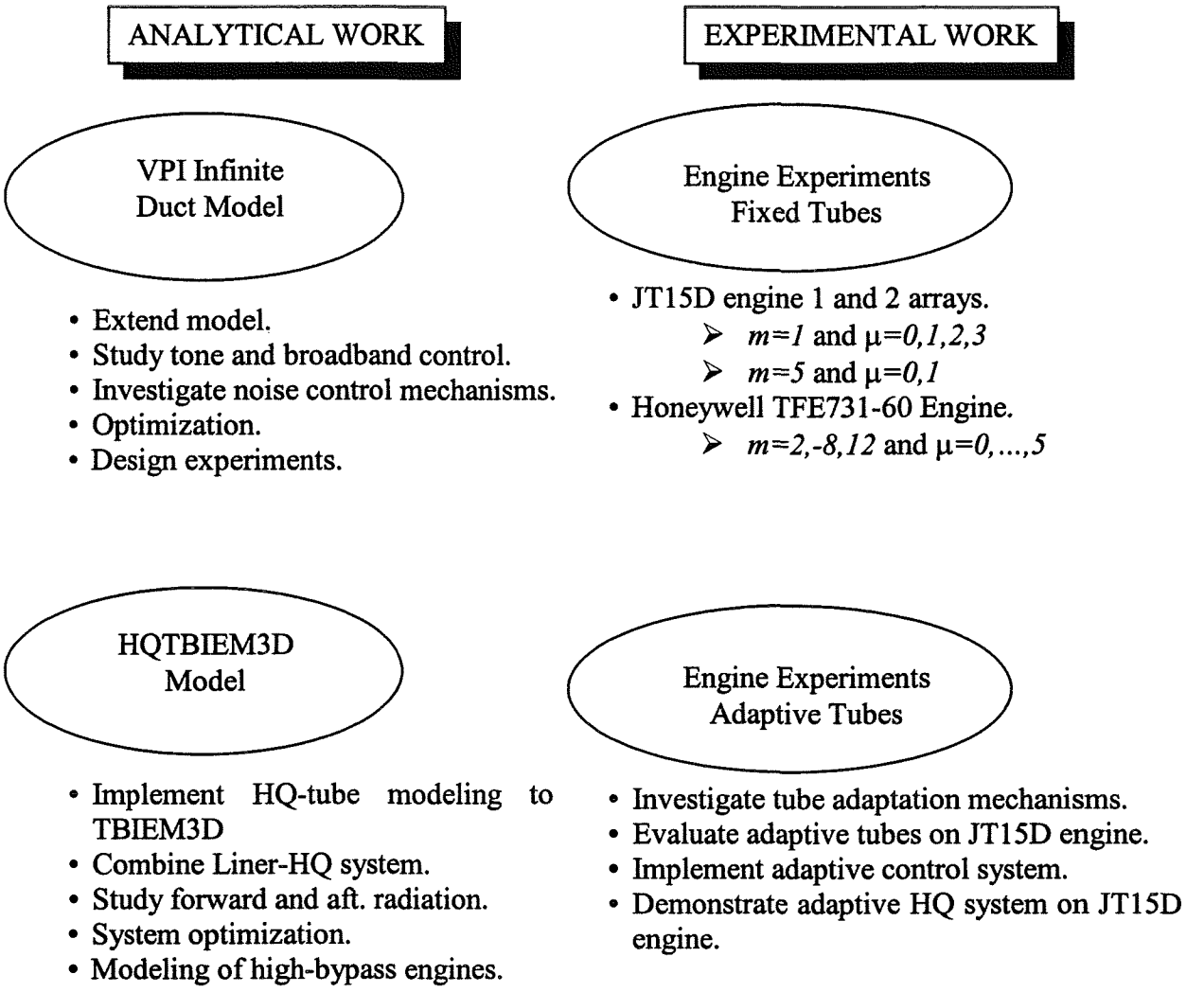

Figure 1.1: Overview of project tasks.

2. HERSCHELQUINCKE-CONCEPT APPLIED TO INLETS

The implementation of the HQ-tube concept on the inlet of a turbofan engine is illustrated in Figure 2.1. The basic technique to model the effect of the HQ-tubes on the inlet sound field was based on separating the tubes from the inlet. Models were then independently developed for the sound field inside the HQ-tubes and for the inlet duct. The effect of the HQ-tubes on the inlet acoustic field was accounted for by considering the interface between the tube's opening and the inlet duct as finite pistons with unknown velocity radiating into the duct. The unknown velocity of these pistons was solved by

matching the acoustic variables at the duct-tube interfaces to the HQ-tube variables, i.e. matching of the impedance at the duct-tube interfaces. Once the piston velocities were solved, the sound field including the effect of the HQ-tubes was easily obtained. Thus, the key step in this modeling approach was to find the pressure field generated by a piston source on the duct wall.

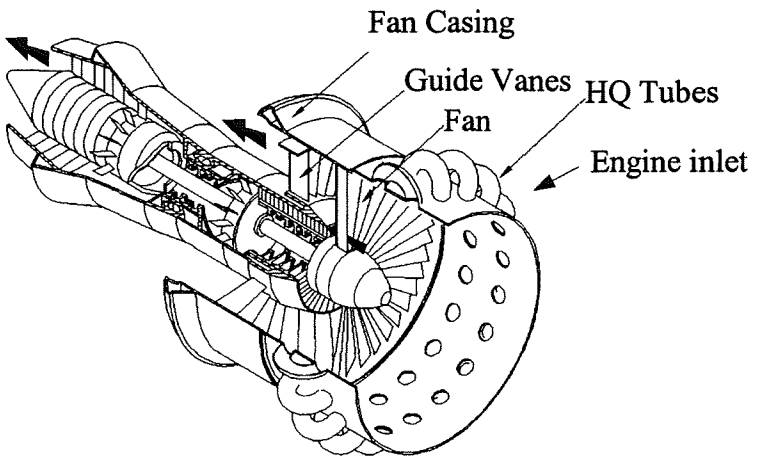

Figure 2.1: HQ system mounted on the inlet of the turbofan engine

The analytical effort on this project consisted of two modeling approaches of the HQ-tube concept applied to the noise reduction of inlet fan noise. The first modeling technique was based on considering the inlet as a segment of an infinite rigid wall duct. The sound field is then expanded in terms of the infinite duct circumferential and radial duct acoustic modes. The main advantage of this approach is that a detailed study of the effect of the HQ-system on the modes is feasible. The second modeling approach was based on the Boundary Integral Equation Method (TBIEM) previously developed by Dunn et. al. [3]. This modeling approach has the advantage that the acoustic fields inside the inlet duct and outside are fully coupled. In addition, the inlet duct wall can be either hard-walled or lined. In the following sections, these modeling approaches are described.

3. ANALYTICAL MODELING - THE INFINITE-DUCT MODEL

The work on the infinite duct model is based on Hallez's Master thesis [4]. The most important results will be described here and readers interested in additional details can refer to reference [4].

The modeling effort of the HQ-tube based on the infinite duct assumption was first initiated on a previous NASA funded research [1]. Thus, it is important to describe the limitations of the first model and the enhancement to this model developed in the current research effort. The most significant assumption on the first model was that the number of tubes, N, in the circumferential array was much larger than the circumferential order of the disturbance modes m_d, i.e. higher $N+1>4m_d$. This assumption allowed using the axis-symmetry of the system to greatly simplify the formulation. However, there were

limitations associated to this approximation such as only evenly distributed circumferential arrays of HQ tubes could be investigated and the interaction effects between the tubes was not completely accounted for. The new model has removed this assumption and its limitations. The other enhancements to the model will be described through the development of the formulation.

The model was validated by comparing the predicted results to the experimentally measured data on two different engines. The model was then used to investigate the noise control mechanisms involved in the HQ system. An impedance analysis is first described that shows that the frequencies of attenuation occur near the resonances of the tubes. The radial and circumferential modes scattering mechanisms are then presented. Finally, advanced configurations for the HQ system are investigated. These configurations take advantage that the acoustic inlet modes are spinning and thus propagate forming helix patterns.

3.1. MODELING TECHNIQUE

In this section, the modeling of the HQ tube system mounted on the engine inlet was attained by assuming the inlet to be part an infinite cylindrical duct as shown in Figure 3.1a. The fan noise source was modeled as a set of modes propagating with known amplitude. The HQ-tubes were then separated from the infinite duct and models were developed for the tubes and the duct independently as indicated in figure 3.1b and c. Then, the sound field generated by a piston source in the infinite duct was required. To this end, the acoustic eigenvalue problem was solved for the rigid-wall infinite duct to find the acoustics modes. These were then used to expand the pressure field inside the duct. The acoustic modes are also used to expand the Green's function, i.e. pressure field generated by a point source. The Green's function was then used to find the expression for the sound field radiated by a finite piston source on the duct wall. For the sake of completeness, these derivations are presented in detail in the Appendix A while only the final expressions are presented in this section.

The pressure due to the fan, i.e. disturbance p_d, at any point in the duct can be expressed as the sum of a set of positive and negative spinning modes traveling in the positive z-direction as

$$p_d(r,\theta,z) = \sum_{m=0}^{M_d}\sum_{n=0}^{N_d}\left((A_{mn}^d)^{pos}e^{-im\theta} + (A_{mn}^d)^{neg}e^{im\theta}\right)J_m\left(k_{mn}r\right)e^{-ik_z^{(+)}z} \tag{3.1}$$

where $A_{mn}^{d(+)}$ and $A_{mn}^{d(-)}$ are the complex amplitude of the positive and negative disturbance mode (m,n), $k_z^{(+)}$ is the axial wavenumber of a positive z-direction traveling wave, and M_d and N_d are the number of m and n modes included in the disturbance. The indexes m and n refer to circumferential and radial mode orders, respectively. The propagation characteristics of the modes are given by the axial wavenumber $k_z^{(+)}$ (see Appendix A).

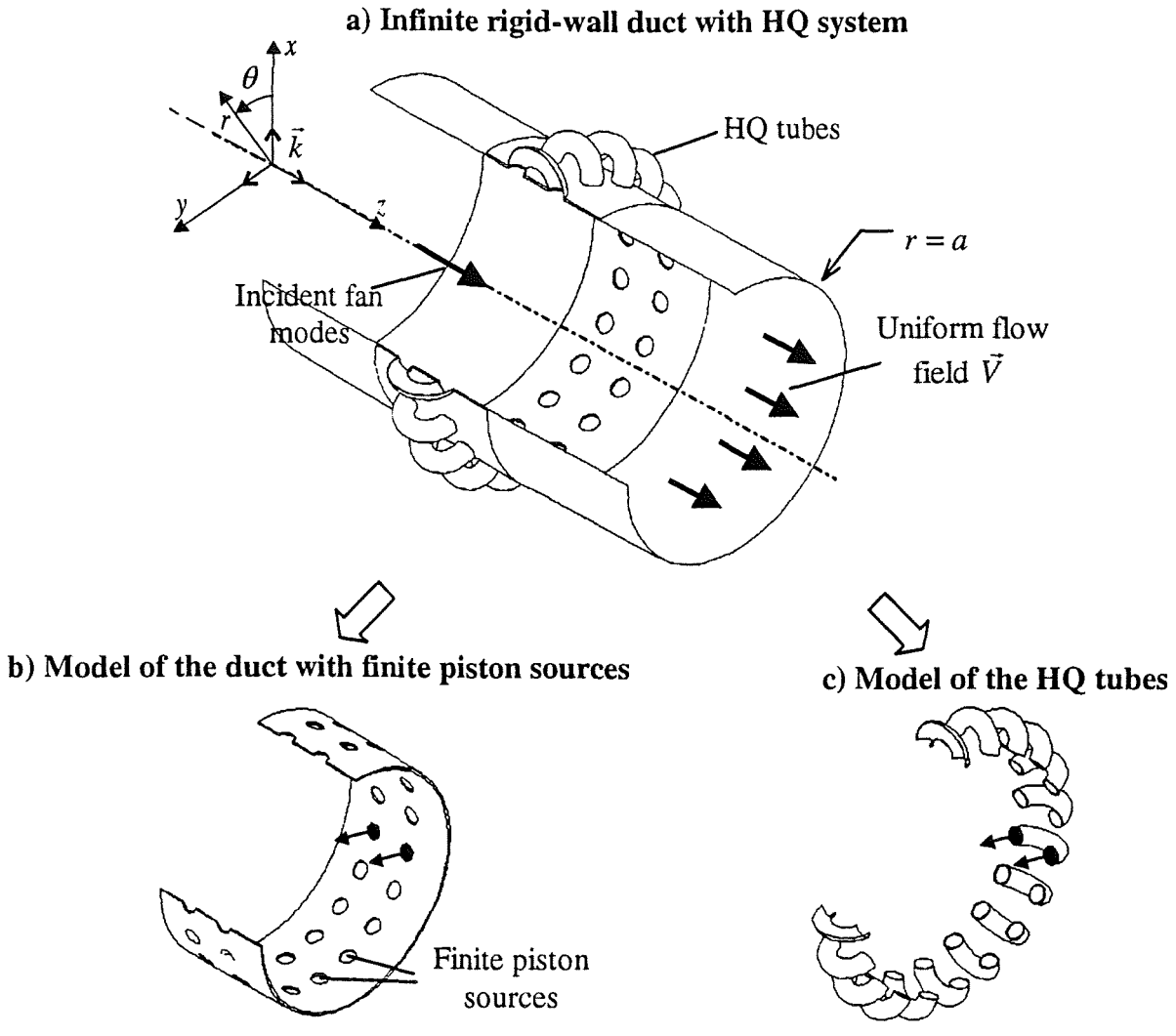

Figure 3.1: a) Engine inlet mounted with HQ tubes modeled as an infinite duct. Model of sound fields b) inside the duct and c) inside the HQ tubes are developed individually.

The acoustic field inside the duct including the effect of the tubes was obtained from the superposition of the sound pressure due to the disturbance and due to the N_s finite piston "sources" that represents the tube-duct interfaces. The number of piston sources is twice the number of tubes. The two piston sources corresponding to the ℓ^{th} tube will be identified by the subscripts "i" (input or tube's end closer to the fan) and "o" (output or tube's end way from the fan) as shown in Figure 3.2. The piston sources have unknown radial velocities. That is $v_{\ell i}$ and $v_{\ell o}$ are the input and output velocities of the ℓ^{th} tube sources, respectively.

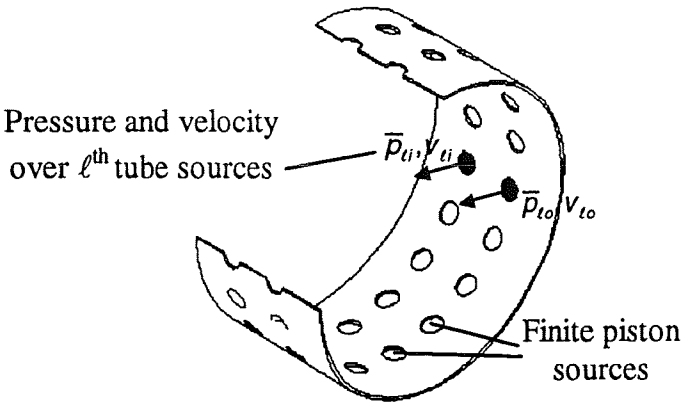

Figure 3.2: Duct with finite piston sources modeling the effect of HQ tubes on duct.

To solve for these piston velocities, the average pressure over each piston source was computed. The average pressure over the pistons can be expressed in the following matrix form as

$$\begin{Bmatrix} \overline{p}_{1i} \\ \overline{p}_{1o} \\ \vdots \\ \overline{p}_{ti} \\ \overline{p}_{to} \\ \vdots \\ \overline{p}_{Ni} \\ \overline{p}_{No} \end{Bmatrix} = \begin{bmatrix} Z_{1i1i} & Z_{1i1o} & Z_{1i2i} & Z_{1i2o} & \cdots & Z_{1iNi} & Z_{1iNo} \\ Z_{1o1i} & Z_{1o1o} & Z_{1o2i} & Z_{1o2o} & \cdots & Z_{1oNi} & Z_{1oNo} \\ \vdots & \vdots & & & & \vdots & \vdots \\ & & & Z_{titi} \; Z_{tito} & & & \\ & & & Z_{toti} \; Z_{toto} & & & \\ \vdots & \vdots & & & & \vdots & \vdots \\ Z_{Ni1i} & Z_{Ni1o} & \cdots & & & Z_{NiNi} & Z_{NiNo} \\ Z_{No1i} & Z_{No1o} & \cdots & & & Z_{NoNi} & Z_{NoNo} \end{bmatrix} \begin{Bmatrix} v_{1i} \\ v_{1o} \\ \vdots \\ v_{ti} \\ v_{to} \\ \vdots \\ v_{Ni} \\ v_{No} \end{Bmatrix} + \begin{Bmatrix} \overline{p}^d_{1i} \\ \overline{p}^d_{1o} \\ \vdots \\ \overline{p}^d_{ti} \\ \overline{p}^d_{to} \\ \vdots \\ \overline{p}^d_{Ni} \\ \overline{p}^d_{No} \end{Bmatrix} \tag{3.2}$$

where $\overline{p}^d_{ti}$ and $\overline{p}^d_{to}$ are the average pressures over the sources of the ℓ^{th} tube due to the disturbance, and N is the number of HQ tubes. The average pressure over the piston sources of the ℓ^{th} tube due to the disturbance is described in Appendix A.

On the other hand, a general element Z_{rs} of the matrix in equation (3.2) represents the average pressure over the "r" piston source due to a unit velocity of the "s" piston source, i.e. impedance function. These impedance functions are derived in Appendix A and their expression depends on the relative positions of the sources.

The next step is to model the sound field inside each tube. In practice, the HQ tubes are constructed as a semi-circle or other smooth shapes. However, for modeling purposes they are considered as straight tubes with uniform cross-section including the perforated screen used in practice at the tube-inlet interfaces. In addition, the sound field inside a

tube is assumed to consist of plane waves only, a valid assumption below the first cut-off frequency of the tube. It is also assumed that there is no flow in the tube. Thus, the tube ends are considered to be piston sources with velocity v^t and constant pressure p^t as shown in Figure 3.3.

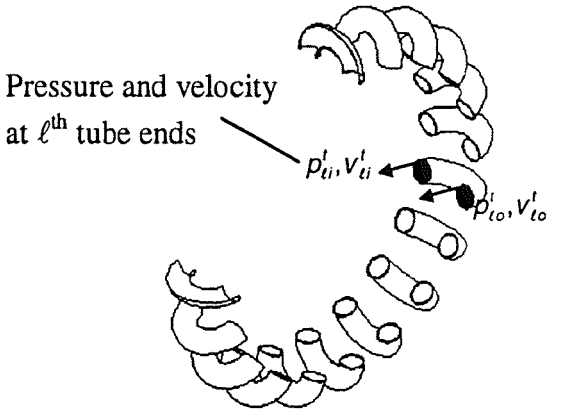

Figure 3.3: Model of the HQ tubes.

The relation between the pressure and particle velocity at the tube's ends is obtained in terms of an impedance matrix for the ℓ^{th} tube that can be expressed as

$$\begin{Bmatrix} p^t_{ti} \\ p^t_{to} \end{Bmatrix} = \begin{bmatrix} Z^{tt}_{ii} & Z^{tt}_{io} \\ Z^{tt}_{oi} & Z^{tt}_{oo} \end{bmatrix} \begin{Bmatrix} v^t_{ti} \\ v^t_{to} \end{Bmatrix} \tag{3.3}$$

The impedance matrix in (3.3) is derived in Appendix A and includes the effect of the perforated screen used in practice at the tube-inlet interfaces to prevent flow separation.

Equation (3.3) gives the impedance matrix for the ℓ^{th} tube alone. Once the tubes are put together in the inlet in some configuration around the duct, the pressure at the end of the tubes can be written in matrix form as

$$\begin{Bmatrix} \overline{p}^t_{1i} \\ \overline{p}^t_{1o} \\ \vdots \\ \overline{p}^t_{\ell i} \\ \overline{p}^t_{\ell o} \\ \vdots \\ \overline{p}^t_{Ni} \\ \overline{p}^t_{No} \end{Bmatrix} = \begin{bmatrix} Z^{t1}_{ii} & Z^{t1}_{io} & 0 & 0 & \cdots & 0 & 0 \\ Z^{t1}_{oi} & Z^{t1}_{oo} & 0 & 0 & & 0 & 0 \\ 0 & 0 & & & & & \\ 0 & 0 & & & & & \\ & & & Z^{t\ell}_{ii} & Z^{t\ell}_{io} & & \\ & & & Z^{t\ell}_{oi} & Z^{t\ell}_{oo} & & \\ 0 & 0 & \cdots & & & Z^{tN}_{ii} & Z^{tN}_{io} \\ 0 & 0 & & & & Z^{tN}_{oi} & Z^{tN}_{oo} \end{bmatrix} \begin{Bmatrix} v^t_{1i} \\ v^t_{1o} \\ \vdots \\ v^t_{\ell i} \\ v^t_{\ell o} \\ \vdots \\ v^t_{Ni} \\ v^t_{No} \end{Bmatrix} \tag{3.4}$$

The main impedance matrix consists of the impedance matrices of each HQ tube on its diagonal and of zeros everywhere else since there is no connection between the tubes.

The sound fields inside the duct and inside the HQ tubes that were developed independently are now assembled to find an expression for the particle velocity at the ends of each tube. The model for the coupled tube-duct system is obtained by matching:

(i) the average pressure on the surface of the source to the pressure in the tube, i.e. $\overline{p}_{\ell i} = p^t_{\ell i}$ and $\overline{p}_{\ell o} = p^t_{\ell o}$, and

(ii) the source velocity to the particle velocity in the tube, $v_{\ell i} = v^t_{\ell i}$ and $v_{\ell o} = v^t_{\ell o}$.

Thus, replacing equation (3.4) into the left-hand side of equation (3.2) the unknown source velocities are written in terms of the impedance functions and of the pressure due to the disturbance as

$$
\begin{Bmatrix} v_{1i} \\ v_{1o} \\ \vdots \\ v_{\ell i} \\ v_{\ell o} \\ \vdots \\ v_{Ni} \\ v_{No} \end{Bmatrix} = \left(\begin{bmatrix} Z_{ii}^{t1} & Z_{io}^{t1} & 0 & 0 & \cdots & 0 & 0 \\ Z_{oi}^{t1} & Z_{oo}^{t1} & 0 & 0 & & 0 & 0 \\ 0 & 0 & \ddots & & & & \\ 0 & 0 & & Z_{ii}^{t\ell} & Z_{io}^{t\ell} & & \vdots \\ \vdots & & & Z_{oi}^{t\ell} & Z_{oo}^{t\ell} & \ddots & \\ & & & & \ddots & Z_{ii}^{tN} & Z_{io}^{tN} \\ 0 & 0 & \cdots & & & Z_{oi}^{tN} & Z_{oo}^{tN} \end{bmatrix} - \right.
$$

$$
\left. \begin{bmatrix} Z_{1i1i} & Z_{1i1o} & Z_{1i2i} & Z_{1i2o} & \cdots & Z_{1iNi} & Z_{1iNo} \\ Z_{1o1i} & Z_{1o1o} & Z_{1o2i} & Z_{1o2o} & & Z_{1oNi} & Z_{1oNo} \\ \vdots & & \ddots & & & & \\ & & & Z_{\ell i\ell i} & Z_{\ell i\ell o} & & \vdots \\ & & & Z_{\ell o\ell i} & Z_{\ell o\ell o} & \ddots & \\ \vdots & & & & \ddots & Z_{NiNi} & Z_{NiNo} \\ Z_{No1i} & Z_{No1o} & \cdots & & & Z_{NoNi} & Z_{NoNo} \end{bmatrix} \right)^{-1} \begin{Bmatrix} \overline{p}_{1i}^{d} \\ \overline{p}_{1o}^{d} \\ \vdots \\ \overline{p}_{\ell i}^{d} \\ \overline{p}_{\ell o}^{d} \\ \vdots \\ \overline{p}_{Ni}^{d} \\ \overline{p}_{No}^{d} \end{Bmatrix} \tag{3.5}
$$

Once the velocity of each source is found, the pressure at any point in the duct can easily be calculated as the superposition of the disturbance and piston sources. An expression for the sound field and transmitted acoustic power upstream of the HQ-tube arrays is found to determine the performance of the HQ system.

3.2. MODAL AMPLITUDES AND TRANSMITTED SOUND POWER

The pressure field in the duct downstream of the HQ tubes, i.e. transmitted field, is computed by adding the pressure due to each piston source and due to the incident disturbance. That is

$$
p_{trans}(r,\theta,z) = p_d(r,\theta,z) + \sum_{r=1}^{N_s} p\ (r,\theta,z|r_r,\theta_r,z_r) \tag{3.6}
$$

where the pressure due to the disturbance $p_d(r,\theta,z)$ is given in (3.1) and the pressure due to a unit velocity of the r^{th} source is obtained as (see Appendix A)

$$p\ (r,\theta,z|r_r,\theta_r,z_r) = \sum_{m=0}^{M_g}\sum_{n=0}^{N_g}(A_{mn}^{(+)})_r \cos m(\theta-\theta_r) J_m(k_{mn}r)\ e^{-ik_z^{(+)}z} \tag{3.7}$$

The pressure due to the piston sources is a stationary pattern that can be represented into positive and negative spinning modes. Thus, equation (3.7) is written as

$$\begin{aligned} p\ (r,\theta,z|r_r,\theta_r,z_r) = &\sum_{m=0}^{M_g}\sum_{n=0}^{N_g}(A_{mn}^{(+)})_r^{pos} J_m(k_{mn}r)\ e^{-im\theta}e^{-ik_z^{(+)}z} \\ &+\sum_{m=0}^{M_g}\sum_{n=0}^{N_g}(A_{mn}^{(+)})_r^{neg} J_m(k_{mn}r)\ e^{+im\theta}e^{-ik_z^{(+)}z} \end{aligned} \tag{3.8}$$

where $\left(A_{mn}^{(+)}\right)_r^{pos}$ and $\left(A_{mn}^{(+)}\right)_r^{neg}$ are the complex amplitude of transmitted modes spinning in the positive and negative direction, respectively, due to source "*r*". These amplitudes are given as (See Appendix)

$$(A_{mn}^{(+)})_r^{pos} = \frac{v_r k_o \rho c}{\pi a^2}\frac{J_m(k_{mn}a)}{\Lambda_{mn}(1-M^2)(k_z^{(+)}-k_z^{(-)})}\frac{2a\alpha_r \sin(m\alpha_r)}{m\alpha_r}\frac{2d_r \sin(k_z^{(+)}d_r)}{k_z^{(+)}d_r}e^{ik_z^{(+)}z_r}\frac{e^{+im\theta_r}}{2} \tag{3.9}$$

$$(A_{mn}^{(+)})_r^{neg} = \frac{v_r k_o \rho c}{\pi a^2}\frac{J_m(k_{mn}a)}{\Lambda_{mn}(1-M^2)(k_z^{(+)}-k_z^{(-)})}\frac{2a\alpha_r \sin(m\alpha_r)}{m\alpha_r}\frac{2d_r \sin(k_z^{(+)}d_r)}{k_z^{(+)}d_r}e^{ik_z^{(+)}z_r}\frac{e^{-im\theta_r}}{2} \tag{3.10}$$

The mode of circumferential order $m=0$ is not spinning; therefore, there is no use of defining positive and negative spinning amplitudes for this mode. However, in order to stay consistent with the previous notations, it can simply be assumed that, for mode m=0, $(A_{0n}^{(+)})_r^{neg}$ is equal to zero and $(A_{0n}^{(+)})_r^{pos}$ is given by the equation

$$(A_{0n}^{(+)})_r^{pos} = \frac{v_r k_o \rho c}{\pi a^2}\frac{J_0(k_{0n}a)}{\Lambda_{0n}(1-M^2)(k_z^{(+)}-k_z^{(-)})}2a\alpha_r \frac{2d_r \sin(k_z^{(+)}d_r)}{k_z^{(+)}d_r}e^{ik_z^{(+)}z_r} \tag{3.11}$$

The source velocity v_r in the previous equations (3.9), (3.10) and (3.11) is obtained from the solution of the system of equations in (3.5). Replacing (3.1) and (3.8) into (3.6), the transmitted pressure upstream of the tubes can be written as

$$p_{trans}(r,\theta,z) = \sum_{m=0}^{M_g}\sum_{n=0}^{N_g}(A_{mn}^{(+)})_{hq}^{pos} J_m(k_{mn}r)e^{-im\theta}e^{-ik_z^{(+)}z} + \sum_{m=0}^{M_g}\sum_{n=0}^{N_g}(A_{mn}^{(+)})_{hq}^{neg} J_m(k_{mn}r)e^{+im\theta}e^{-ik_z^{(+)}z} \tag{3.12}$$

where

$$(A_{mn}^{(+)})_{hq}^{pos} = \left(A_{mn}^{d}\right)^{pos} + \sum_{r=1}^{N_s}(A_{mn}^{(+)})_r^{pos} \tag{3.13}$$

$$(A_{mn}^{(+)})_{hq}^{neg} = (A_{mn}^{d})^{neg} + \sum_{r=1}^{N_s} (A_{mn}^{(+)})_{r}^{neg} \tag{3.14}$$

are the modal amplitudes of the transmitted mode (m,n) spinning in positive and negative direction, respectively, due to all sources and the fan disturbance. The pressure reflected downstream of the HQ tubes can be similarly computed to give

$$p_{ref}(r,\theta,z) = \sum_{m=0}^{M_g}\sum_{n=0}^{N_g} (A_{mn}^{(-)})_{hq}^{pos} J_m(k_{mn}r)\, e^{-im\theta} e^{-ik_z^{(-)}z} + \sum_{m=0}^{M_g}\sum_{n=0}^{N_g} (A_{mn}^{(-)})_{hq}^{neg} J_m(k_{mn}r)\, e^{+im\theta} e^{-ik_z^{(-)}z} \tag{3.15}$$

where

$$(A_{mn}^{(-)})_{hq}^{pos} = \sum_{r=1}^{N_s} (A_{mn}^{(-)})_{r}^{pos} \tag{3.16}$$

$$(A_{mn}^{(-)})_{hq}^{neg} = \sum_{r=1}^{N_s} (A_{mn}^{(-)})_{r}^{neg} \tag{3.17}$$

are the amplitudes of the reflected mode (m,n), spinning in the positive and negative direction, respectively, due to the radiation of all sources, and $\left(A_{mn}^{(-)}\right)_r^{pos}$ and $\left(A_{mn}^{(-)}\right)_r^{neg}$ are the amplitudes of mode (m,n) spinning in the positive and negative direction, respectively, due to an individual source "r" given as

$$(A_{mn}^{(-)})_{r}^{pos} = \frac{v_r k_o \rho c}{\pi a^2} \frac{J_m(k_{mn}a)}{\Lambda_{mn}(1-M^2)(k_z^{(+)} - k_z^{(-)})} \frac{2a\alpha_r \sin(m\alpha_r)}{m\alpha_r} \frac{2d_r \sin(k_z^{(-)}d_r)}{k_z^{(-)}d_r} e^{ik_z^{(-)}z_r} \frac{e^{+im\theta_r}}{2} \tag{3.18}$$

$$(A_{mn}^{(-)})_{r}^{neg} = \frac{v_r k_o \rho c}{\pi a^2} \frac{J_m(k_{mn}a)}{\Lambda_{mn}(1-M^2)(k_z^{(+)} - k_z^{(-)})} \frac{2a\alpha_r \sin(m\alpha_r)}{m\alpha_r} \frac{2d_r \sin(k_z^{(-)}d_r)}{k_z^{(-)}d_r} e^{ik_z^{(-)}z_r} \frac{e^{-im\theta_r}}{2} \tag{3.19}$$

The radiated sound power can now be computed. To this end, the acoustic intensity in the z-direction is written as

$$I_z = \frac{1}{2} Real\left[p v_z^* + \rho c |v_z|^2 M + \frac{|p|^2}{\rho c} M + v_z p^* M^2 \right] \tag{3.20}$$

where v_z is the particle velocity in the z-direction and asterisk (*) denotes complex conjugate.

The acoustic power is obtained by integrating the intensity over the cross sectional area of the duct as

$$W = \int_0^a \int_0^{2\pi} I_z r dr d\theta \tag{3.21}$$

Considering the orthogonality condition of the modes results in the total transmitted power to be given as

$$W = \sum_{m=0}^{M_g} \sum_{n=0}^{N_g} W_{mn}^T \tag{3.22}$$

Therefore, the total sound power transmitted downstream of the HQ system is expressed in terms of the modal amplitudes as

$$W_{mn}^T = \frac{\pi a^2 \Lambda_{mn}}{\rho c} \left(\left| \left(A_{mn}^{(+)} \right)_{hq}^{pos} \right|^2 + \left| \left(A_{mn}^{(+)} \right)_{hq}^{neg} \right|^2 \right) \times \left\{ \left(1 + M^2\right) Real \left[\frac{\left(k_z^{(+)}\right)}{\left(k_o - k_z^{(+)} M\right)} \right] + \frac{M \left| k_z^{(+)} \right|^2}{\left| k_o - k_z^{(+)} M \right|^2} + M \right\} \tag{3.23}$$

where

$$\Lambda_{mn} = \begin{cases} \frac{1}{2} J_m^2 \left(k_{mn} a\right) & \text{if} \quad m = 0 \\ \frac{1}{2} \left[1 - \frac{m^2}{\left(k_{mn} a\right)^2} \right] J_m^2 \left(k_{mn} a\right) & \text{if} \quad m \neq 0 \end{cases} \tag{3.24}$$

The transmitted acoustic power is the metric used to determine the performance of the HQ-tube system. The far-field radiation pattern resulting from the implementation of the HQ-tube system is not predicted using this infinite duct model.

3.3. OPTIMIZATION TECHNIQUE USING GENETIC ALGORITHMS

In the previous section, the modeling technique was presented. The model allows predicting the sound power reduction provided by the HQ system. However, since the performance of the HQ tube system depends on several parameters, it would be useful to develop an optimization technique to find the set of parameters that gives the best noise reduction. This technique will be based on the genetic algorithms (GA) and is presented in this section. Genetic algorithms use probabilistic search methods to minimize a specified cost or fitness function. The method is based upon an abstraction of the process of natural selection and was developed by Goldberg in 1989 [5]. The main advantage of the genetic algorithm is that it allows seeking for the global optimum, whereas traditional optimization methods can converge toward a local minimum, and miss the global optimum. Genetic algorithms are used here to find the optimal set of parameters that will minimize the cost function. In our case, this function is the radiated sound power upstream of the HQ system and the parameters to optimize are the dimensions of the HQ system such as centerline tube length, tube cross sectional area, axial location and so forth.

The fundamental characteristics of this optimization technique is that (i) the algorithm does not work with the parameters themselves but with a coding of them, (ii) the optimum search operates on a population of solution points, (iii) there is no need for

knowing the derivatives of the fitness function and (iv) the algorithm uses probabilistic transition rules rather than deterministic ones. The optimization process used by the GA is illustrated in the flow chart, Figure 3.4. The main steps are explained in the following sections.

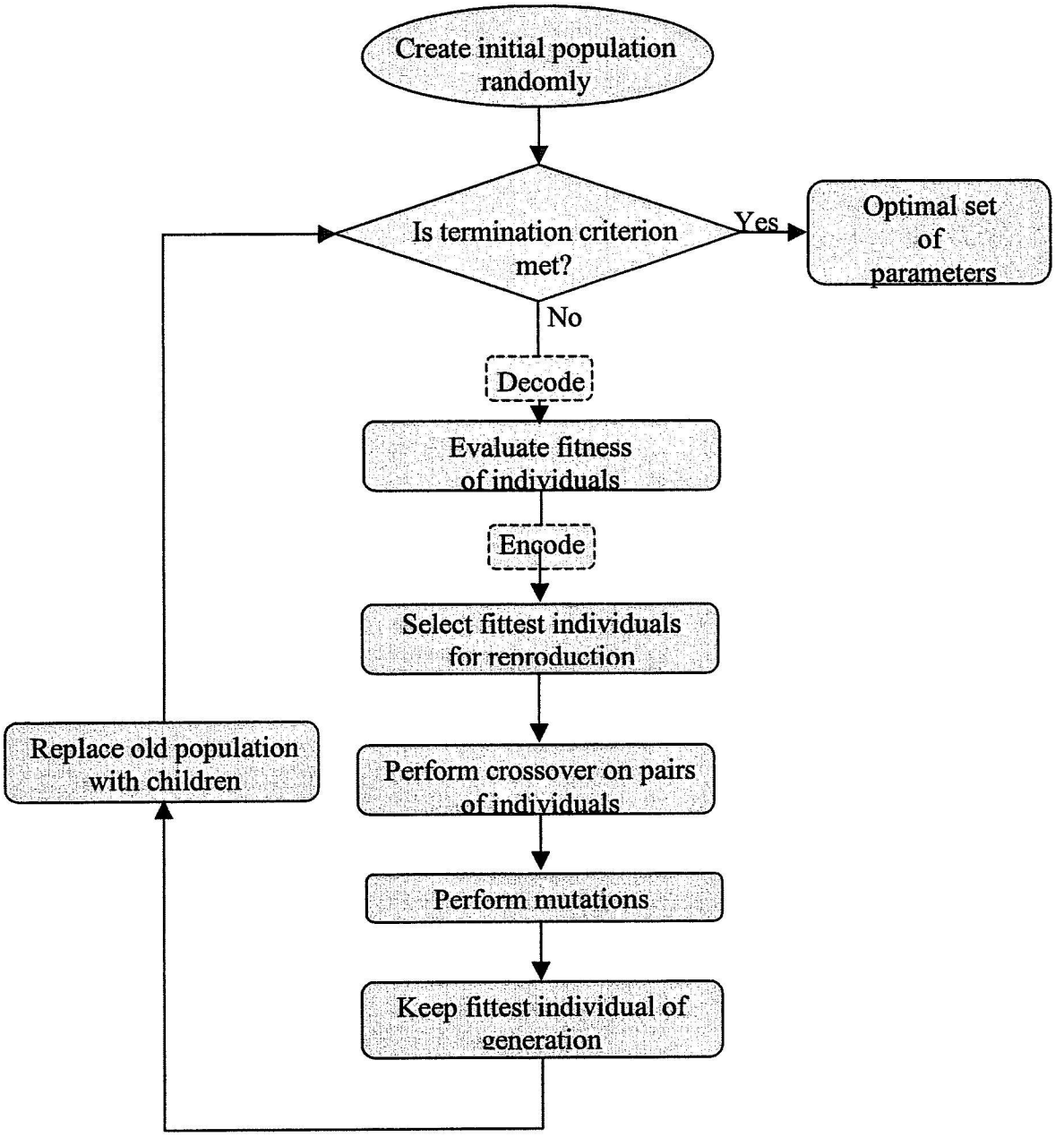

Figure 3.4: Main steps of the optimization process using genetic algorithms.

3.3.1 Encoding

The main idea of the GA consists of representing the input parameters by a binary string and manipulating this string until the optimal value is found. Each parameter to be optimized is discretized using a set of possible values within a specified range. The

chosen parameter value is then written as a binary number coded on n bits. Thus, the total number of possible values is 2^n. The same principle is applied to each parameter and by concatenating the binary strings corresponding to a set of parameter values, an individual or chromosome is formed. Each binary number 0 or 1 is called gene. Figure 3.5 illustrates this mechanism where 2 parameters are to be optimized and each parameter is encoded on 4 bits. Therefore, there are 2^4=16 possible discrete values for each parameter. A particular value is chosen for each of these two parameters and the two corresponding binary strings are concatenated producing an individual of 2x4=8 bits. Therefore, the total possible number of individuals that can be created is $2^{(2x4)}$=256 individuals.

Each individual has to be encoded for genetic manipulations such as selection, crossover and mutations. The binary string is then decoded to find the value of the corresponding parameters and to evaluate the corresponding fitness.

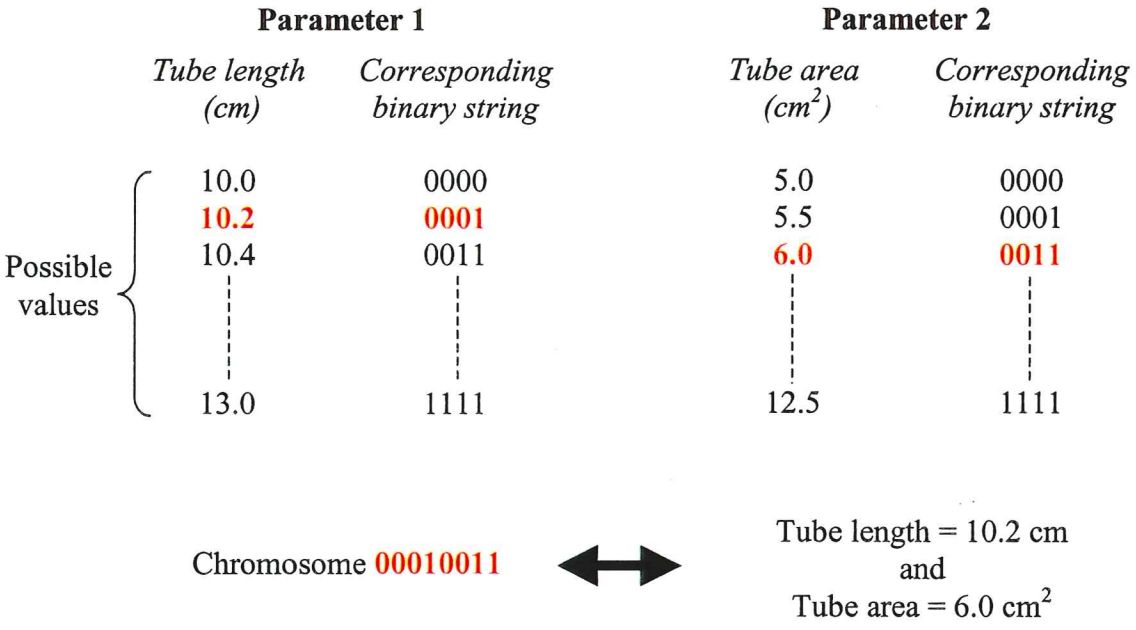

Figure 3.5: Encoding of parameters into chromosomes.

3.3.2 Fitness function

The fitness function is the link between the genetic algorithm and the system. It gives the information on how suitable an individual is for the goal of the optimization. In our case, the fitness function will be the sound power radiated at the end of the engine inlet and the goal of the optimization is to minimize its value. The key advantage of the GA is that it does not require information about the fitness function (such as derivatives like in the typical optimization techniques). The only required information is the fitness value associated with an individual. The fitness of a chromosome is a determinant criterion for the selection process.

3.3.3 Selection

The initial population is chosen such that each parameter takes a random value in a specified range. In this study, the range of each parameter is selected such that unrealistic tubes cannot be generated (i.e. for instance tubes with centerline length smaller than the distance between tube ends). Whereas the initial population is chosen randomly, one needs to find a way to decide which of the individuals in the current population will be allowed to pass their genetic material to the following generations. This is the role of the selection process. The key assumption is to give preference to fitter individuals. In our case, the tournament selection will be used. Two chromosomes are selected randomly from the current population, but only the one with the higher fitness value is inserted into the mating pool. The mating pool constitutes the group of individuals that will be mated to create the new generation. This process is repeated until the number of chromosome chosen for reproduction is the same as the initial number of individuals in the population.

3.3.4 Crossover

The crossover operator is the key operator to generate new individuals. This operator is applied to each pair of the mating pool to produce one or two children. The pairs of parent chromosomes, which the crossover applies on, are chosen randomly among the mating pool. In our case, the uniform crossover technique will be applied. Therefore, every gene will exchange genetic material with the other parent's gene of the same location with a probability p_c (p_c is equal to 0.5 here). This process is illustrated in the following example, Figure 3.6. For each gene of the parent chromosomes, a random number is chosen between 0 and 1 and if this number is higher than p_c, the gene is exchanged with the gene from the other parent. This happens on the genes at position 1, 4, 5 and 7 in the example. This way, the children receive genetic information coming from their two parents.

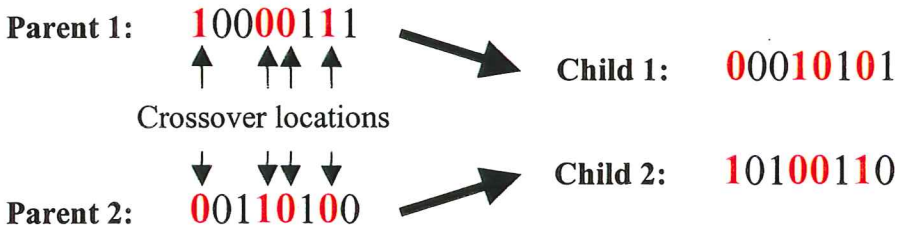

Figure 3.6: Example of uniform crossover.

3.3.5 Mutation

The final operation of the mating process is the mutation and is applied to the generation produced after the crossover. This process should allow to find solutions which contain genes that are nonexistent in the initial population. There are two kinds of mutation. First of all, the **jump** mutation directly acts on the chromosome and consists of changing the value of a gene, i.e. 0 is changed to 1 or vice-versa. On the other hand, the **creep** mutation consists of decoding the value of the chromosome and changing it by a small discrete increment (range of the parameter value divided by the number of possible

values). This last type of mutation directly acts on the discrete value of the parameter (decimal value). The mutation process is illustrated in Figure 3.7. The chance that a creep or jump mutation will occur is determined by the mutation probability. While a high probability can transform the GA into a kind of random search algorithm, it has to be kept high enough to avoid premature convergence into a non-optimum zone. Here, the jump and creep mutations probability will both be kept under 0.05.

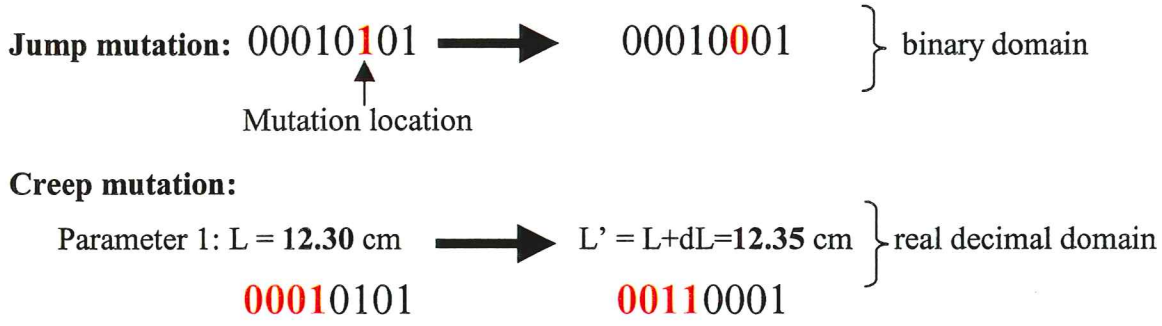

Figure 3.7: Example of jump and creep of mutation.

3.3.6 Replacement strategy

Once the operations of selection, crossover and mutation are completed, the current population is replaced with the children just created. However, an elitist strategy will be used here, therefore, all but one individuals are replaced by children. The individual from the old generation with the highest fitness value is directly transferred to the new generation. This way, the best genetic information of a population is maintained through the generations.

The creation of new individuals and replacement of the old population process will continue until the termination criterion is met. In our case, this criterion will be the maximum number of generations (usually set to 100), which is limited mainly for a computation time reason.

3.4. NUMERICAL RESULTS

In section 3.1, an infinite-duct based modeling technique was developed to predict the effect of the HQ tubes applied to the inlet of an engine. In order to validate this analytical approach, the predicted results will be compared to experimental data measured on two real engines, the Pratt and Whittney JT15D [1] and the Honeywell TFE731-60 [6]. A circumferential array of 20 and 27 tubes were used on these engines, respectively. Analytical and experimental results will be compared for the BPF tone reduction and then for the broadband reduction. Finally, a convergence study will be performed to investigate the effect of the number of modes included in the Green's function. This study will show the number of modes to include in the calculations in order to have accurate predictions.

3.4.1 Engine Descriptions

JT15D turbofan engine

The Pratt and Whitney JT15D turbofan engine is a twin spool turbofan engine with a full-length bypass duct and a maximum bypass ratio of 2.7. The thrust for this engine ranges from 2200 to 3350 lbs. There is a single-stage axial flow fan with 28 blades and a centrifugal high-pressure compressor with 16 full vanes and 16 splitter vanes. There are 33 exit guide vanes (EGV) and no inlet vanes. The diameter at the fan stage location is *0.53 m*. The length of the inlet in the axial direction is *0.46 m*. Experimental results were obtained by operating the engine at various speeds near idle condition yielding a BPF ranging from 2260 to 2420 Hz. However, the design speed for the HQ system tested on this engine corresponds to a BPF of about 2320 Hz. Near this condition, the inlet intake flow speed is about *42.5 m/s* which yields a Mach number of M=*-0.12*. Given these dimensions and Mach number, a large number of modes are in cut-on condition near the BPF range. The cut-off frequencies of the lower modes existing in this inlet are shown in Table 3-1.

To enhance the tonal nature of the inlet radiated sound and to excite the m=*1* modes to dominance, a set of 27 exciter rods is mounted upstream of the fan stage. The wakes from the rods interact with the fan blades to produce tones which are significantly higher in sound level than without the rod interactions, and thus emulate strong wake-stator interactions. The modes generated by the fan-EGV are cut-off at the BPF frequencies considered. The modal amplitudes of these dominant modes were measured at a BPF of 2320 Hz and are shown in Table 3-2. For the sake of simplicity, these modal amplitudes are assumed to remain constant over the BPF range from 2260 up to 2381 Hz. This last frequency corresponds to the cut-off frequency of the next radial mode of order (1,3).

As an illustration, Figure 3.8 shows the inlet of the JT15D engine mounted with two arrays of tubes.

Table 3-1: Inlet mode analytical cut-off frequencies in Hertz for the JT15D engine.

		Radial order *n*				
		0	**1**	**2**	**3**	**4**
Circumferential order *m*	**0**	0	779	1427	2069	2710
	1	374	1084	1736	2381	3023
	2	621	1364	2027	2678	3324
	3	854	1630	2307	2966	3618
	4	1081	1888	2579	3246	3904
	5	1305	2139	2844	3521	4184
	6	1525	2386	3105	3790	4460
	7	1744	2630	3361	4055	4732
	8	1962	2871	3615	4317	5000
	9	2178	3109	3865	4576	5265
	10	2394	3345	4113	4832	5528

Table 3-2: Inlet fan mode amplitudes for the JT15D engine.

Fan mode	**Amplitude (Pa)**
(1,0)	56.3
(1,1)	$55.5e^{-4.9i}$
(1,2)	$111.0e^{0.1i}$

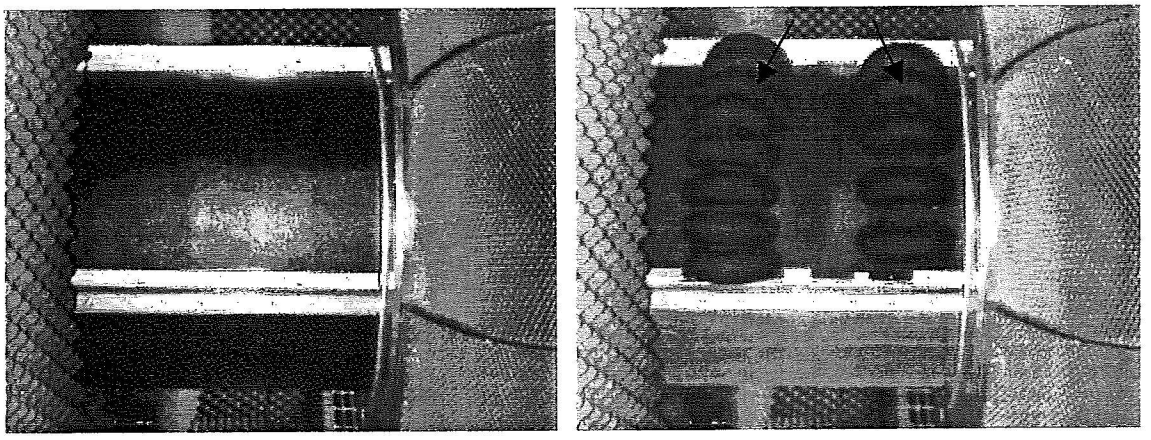

Figure 3.8: Pictures of the JT15D inlet configured (a) as a hard wall and (b) with two arrays of HQ tubes.

TFE731-60 engine

The Honeywell TFE 731-60 turbofan engine has a 4-stage axial compressor, and a centrifugal high-pressure compressor. The maximum bypass ratio is 3.9. There is a single-stage axial flow fan with 22 blades and 10 bypass struts. The diameter at the fan stage location is *0.787 m* and the length of the inlet in the axial direction is *0.51 m*. The thrust for this engine ranges from 3500 to 5000 lbs. Experimental results were obtained by operating the engine at various power settings (60, 81, 88, 92, 98 %) yielding a BPF ranging from 2250-3730 Hz. The power setting selected for the design of the HQ tube system was 60% corresponding to a BPF of 2250 Hz. Near this condition, the inlet intake flow speed yields a Mach number of *M=-0.29* [6]. The cut-off frequencies of the lower modes existing in this inlet are shown in Table 3-3 (as an illustration, modes cut-on at a BPF of 2250 Hz are written in bold in the table).

Table 3-3: Inlet mode analytical cut-off frequencies in Hertz for the TFE731-60 engine.

		Radial order *n*					
		0	**1**	**2**	**3**	**4**	**5**
Circumferential order *m*	**0**	0	527	965	1400	1833	2266
	1	253	734	1175	1611	2045	2479
	2	420	923	1372	1812	2249	2685
	3	578	1103	1561	2007	2448	2886
	4	732	1277	1745	2197	2641	3082
	5	883	1448	1925	2382	2831	3275
	6	1032	1615	2101	2565	3018	3465
	7	1180	1780	2274	2744	3202	3653
	8	1327	1942	2446	2921	3383	3838
	9	1474	2103	2615	3096	3563	4021
	10	1620	2263	2783	3270	3740	4202
	11	1765	2422	2949	3441	3916	4381
	12	1910	2579	3114	3612	4091	4559
	13	2054	2736	3278	3781	4264	4736
	14	2198	2892	3440	3948	4436	4911
	15	2342	3047	3602	4115	4607	5085

This particular engine has characteristics that make it very interesting for the present study. The rotor-strut interaction is such that the dominant modes propagating at the BPF frequency are of different circumferential order, i.e. *m*=-8, 2 and 12. Again the rotor-EGV interaction results in cut-off modes. The modal amplitudes of the dominant modes at a BPF of 2250 Hz were measured and are shown in Table 3-4.

Table 3-4: Inlet fan mode amplitudes for the TFE731-60 engine.

Fan mode	Amplitude (Pa)
(-8,0)	1.2
(-8,1)	$1.0^{e-2.4i}$
(2.0)	$1.9^{e-1.0i}$
(2.1)	$0.8^{e0.4i}$
(2.2)	$3.3^{e-4.6i}$
(2.3)	$0.5^{e-4.0i}$
(12,0)	$3.2^{e1.2i}$

Pictures of the TFE731-60 inlet mounted with 2 arrays of HQ tubes are shown in Figure 3.9.

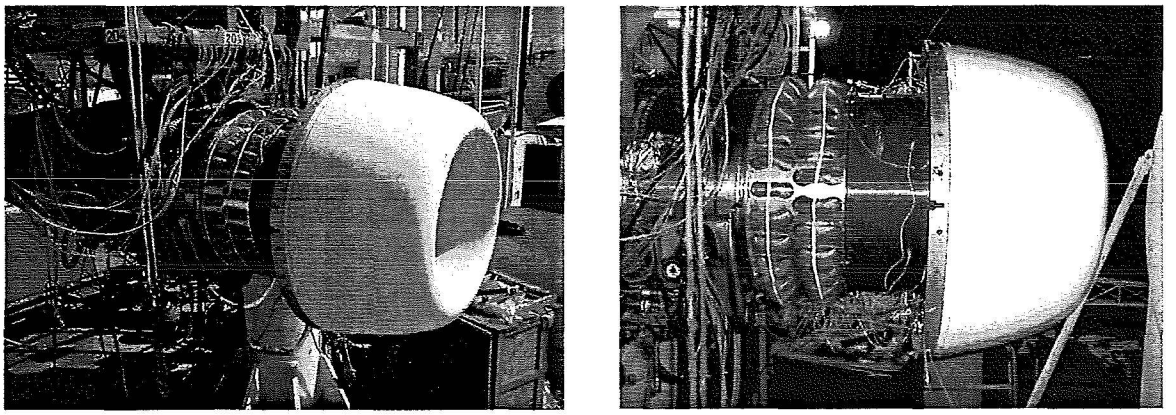

Figure 3.9: Pictures of the TFE731 inlet configured with two arrays of HQ tubes.

3.4.2 Blade passage frequency results

JT15D engine Results

In order to investigate the accuracy of the model, results predicted by the computer code will be compared to experimental results measured on the engine. The comparison will first be done on the JT15D turbofan engine.

For these experiments, the HQ tube system consists of a single array of 20 tubes positioned at *0.35 m* upstream from the fan. The HQ tubes were designed to provide an optimal reduction at 2320 Hz, which is near the tube second resonance frequency. That is, the centerline tube length and distance between tube ends were chosen using the

modeling technique such that the HQ system provides reduction at 2320 Hz The centerline tube length is *0.118 m*. The distance between the two tube ends is *0.092 m* and the tube diameter is *0.038 m*. A perforated screen was placed at the ends of the tubes to minimize the undesirable flow separation at the tube-inlet interfaces. The parameters of the screen are given by the thickness t_{ps}=*0.00075 m*, the orifice radius a_{orif}=*0.00075 m*, and the screen open area ratio σ=*25%*.

The experimentally measured power attenuation of the BPF tone is presented in Figure 3.10 for a range of BPF tone frequencies from 2240 to 2380 Hz. Three different measurements for the same system are shown on this plot. Although the test setup is the same for the three cases, the radiated sound power is not exactly the same because the engine rotation speed is fluctuating. The HQ tube system is very efficient at these BPF frequencies and provides a maximum power level reduction of 6.0 dB at 2312 Hz.

Using the parameters from the experiment, the predicted sound power reduction is also computed to validate the accuracy of the model. The cut-off frequencies of the first radial modes (*m=1*, μ=*0,1,2,3*) are 374, 1084, 1736, and 2381 Hz, respectively. Therefore, there are 3 propagating modes at a BPF lower than 2381 Hz. The amplitudes of these first three fan modes have been experimentally determined for a BPF of 2320 Hz, as explained in the previous section. These amplitudes were used in the model for a frequency range from 2240 to 2380 Hz. Since the amplitude of the fourth radial mode, cut-on at 2381 Hz, is unknown, the analysis was not performed above this frequency.

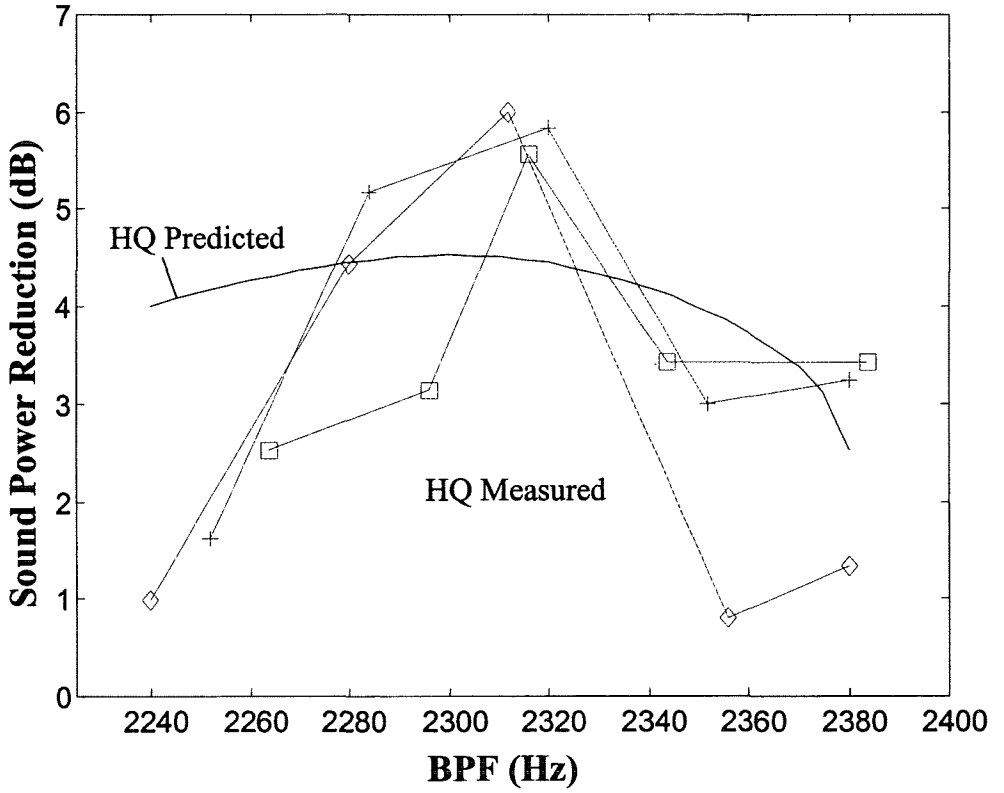

Figure 3.10: Comparison of the predicted and measured BPF sound power reduction level with one array of 20 tubes mounted on the inlet of the JT15D engine.

The predicted sound power reduction shows that there is an optimal frequency of attenuation at about 2300 Hz with a power reduction of about 4.5 dB. The analytical and experimental results show good agreement in both the optimum frequency of attenuation and the level of sound power reduction. However, the model predicts good attenuation over a wider frequency range than the experiments. This is probably due to the fact that the mode amplitudes are assumed to remain constant over the BPF range, which is probably not the case in reality.

TFE731-60 engine Results

The experiments run on the TFE731-60 were slightly different from the previous ones. Here, an array of 27 HQ tubes was mounted on the inlet of the engine. The array was positioned at *0.30 m* upstream from the fan. The centerline tube length was *0.135 m*. The distance between the two tube ends is *0.104 m* and the tube diameter was *0.042 m*. The parameters of the perforated screen were given by the thickness t_{ps}= *0.0015 m,* the orifice radius a_{orif}=*0.0016 m*, and the screen open area ratio σ=*21%*. The sound power reduction provided by the HQ tubes was experimentally measured at BPF of 2250 Hz to be 2.6 dB while the predicted sound power reduction at this frequency was 0.4 dB. It is clear that the model underestimates the sound power reduction. This difference between the experimental and predicted results is probably due to inaccurate measurements of the mode amplitudes present on the real engine.

3.4.3 Broadband results

The HQ concept applied to turbofan engine noise was primarily envisioned as a tonal noise reduction strategy, with the intent that designing the HQ inlet so that the frequencies at which reduction is achieved correspond to the BPF tone and harmonics. However, the HQ inlet also results in significant attenuation in the broadband noise levels radiated from the engine inlet. In this section, the predicted results will be compared to the measured data for both engines.

In the case of a BPF analysis, the complex amplitudes of the few dominant modes propagating at the BPF frequency could be measured and used as input in the model. However, in the case of a broadband study, the amplitudes of all the propagating modes are not available. Therefore, there are usually two kinds of assumptions that can be made to find the modal amplitudes. At each frequency, either all cut-on modes have the same amplitude or each mode will equally contribute to the total sound power. In both cases, the phase of the modes is chosen randomly. Results for both approaches will be shown in this section.

JT15D engine results

The experimentally measured inlet broadband sound power for both the rigid wall inlet and the inlet with a single array of 20 HQ tubes is shown in Figure 3.11a for a BPF at 2320 Hz. Figure 3.11a also shows the analytical broadband prediction using the equal modal amplitude approach. The prediction based on the equal modal power technique is shown in Figure 3.11b.

The HQ array resulted in significant broadband reduction, primarily in the vicinity of the first and second resonances of system (i.e., approximately 1200 and 2400 Hz). It is also clear in Figure 3.11 that the predicted results using the equal modal power approach are closer to the experimental data than the predictions using equal modal amplitudes. The overall A-weighted measured sound power reduction over the frequency range from 500 to 3200 Hz was 1.5 dB. The overall predicted reductions were 0.3 dB and 1.0 dB for the equal amplitude and equal power approach, respectively. In the case of the equal modal power, the model predict the broadband reduction very well, however, the analytical results seemed to under predict the reduction, especially in the frequency range from 1200 to 1800 Hz.

It is important to notice that the previous plots show the broadband sound power levels and are to be differentiated from the BPF plots in the previous section. When the broadband noise is considered, it is assumed that all cut-on modes (21 modes) are present in the disturbance and contribute to the propagation of acoustic energy with a relatively equal influence (modes have same amplitudes or generate same power). However, in the case of a BPF or tone analysis, most of the acoustic energy is propagated through a few dominant modes, whose amplitudes are much higher than the amplitudes of the rest of the cut-on modes. This is the reason why the plots in Figure 3.11 should not be considered at the frequency of the BPF, i.e. 2320 Hz.

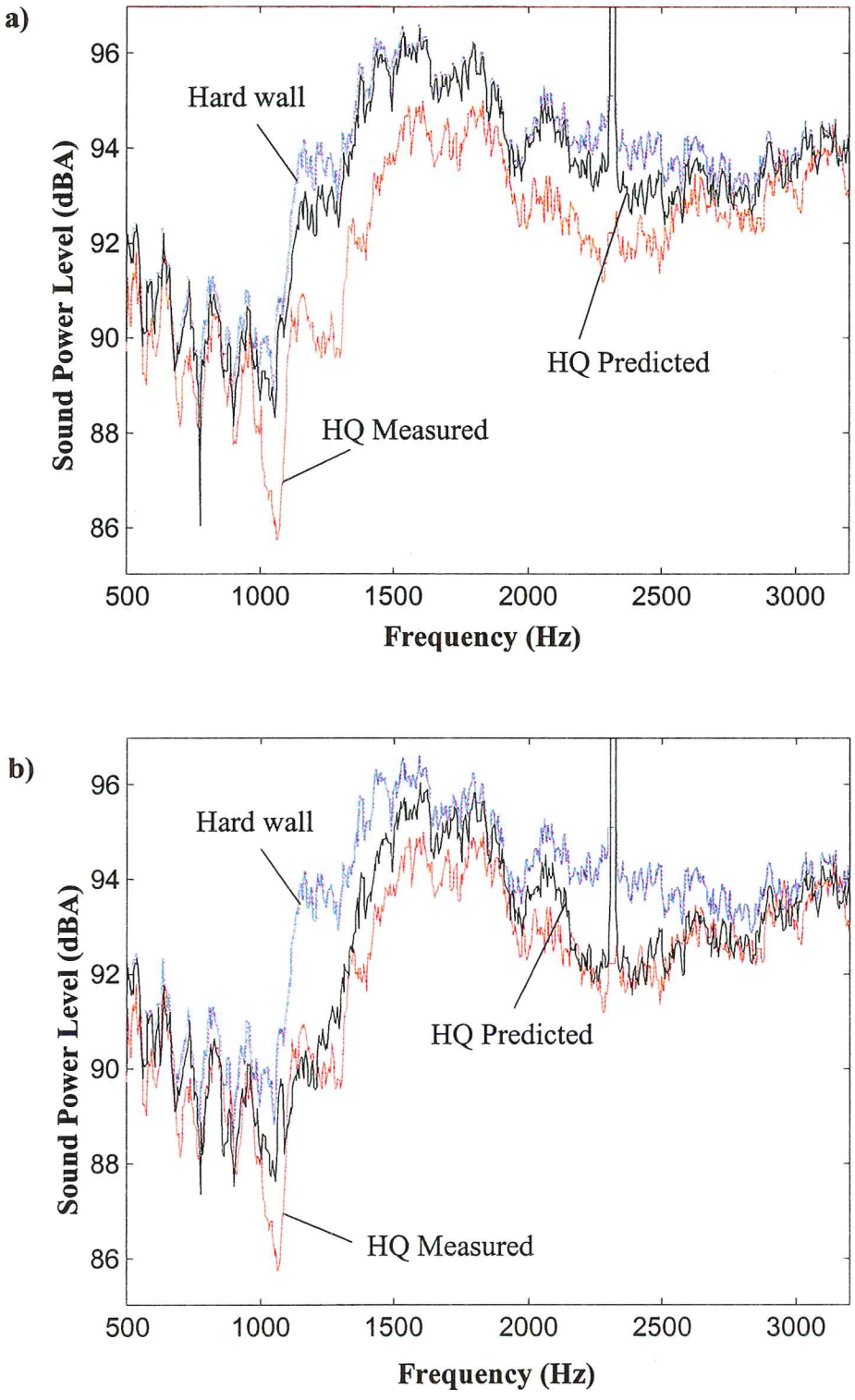

Figure 3.11: Comparison of the predicted and measured sound power levels with one array of 20 tubes mounted on the inlet of the JT15D engine a) equal modal amplitudes approach b) equal modal power approach.

TFE731-60 engine results

The broadband sound power levels were also measured for the TFE731-60 engine at a BPF of 2560 Hz of. In this case, there is a single array of 27 tubes mounted on the inlet of the engine. Figure 3.12 shows these experimental results. Once again, the predicted results using the equal amplitudes and equal modal power approaches are shown in Figure 3.12 a and b, respectively.

Figure 3.12 shows that, again, the equal modal power approach provides results closer to the experimental data. The overall A-weighted measured sound power reduction over the frequency range from 500 to 3000 Hz is 0.8 dB. The overall predicted reductions are 0.2 dB and 0.5 dB for the equal amplitude and equal power approach, respectively.

The previous comparisons showed that the experimental and predicted results were in good agreement, allowing to validate the model, although, the code seemed to underpredict slightly the reduction provided by the HQ tube system. Thus, the model will be used in the next chapter to study the noise control mechanisms involved in the HQ tube system.

3.4.4 Convergence of the predicted results

In the modeling technique presented in Section 3.1, the model of the HQ tube in the duct was based on the Green's function. The Green's function is expanded in terms of the duct modes as an infinite series. In practice, a finite number of modes are included in the calculations. The aim of this study is to help choosing an appropriate number of modes to include in the computations.

In the case of the HQ system, the source is not a point source but a piston source located on the duct wall at each end of the tubes. Therefore, the influence of the number of modes on the impedance function of a piston source viewed by another piston source will be investigated here. This impedance function is simply the average sound pressure over the surface of an observer source due to the same or another piston source with unit velocity. The expression for this impedance function is given in Appendix A and depends on the relative position of the observation and source pistons. The contribution of each mode to the impedance function will first be studied for different positions of the observer source. Then, the influence of the number of modes in terms of sound power level will be investigated. The parameters of the JT15D engine were used in this study.

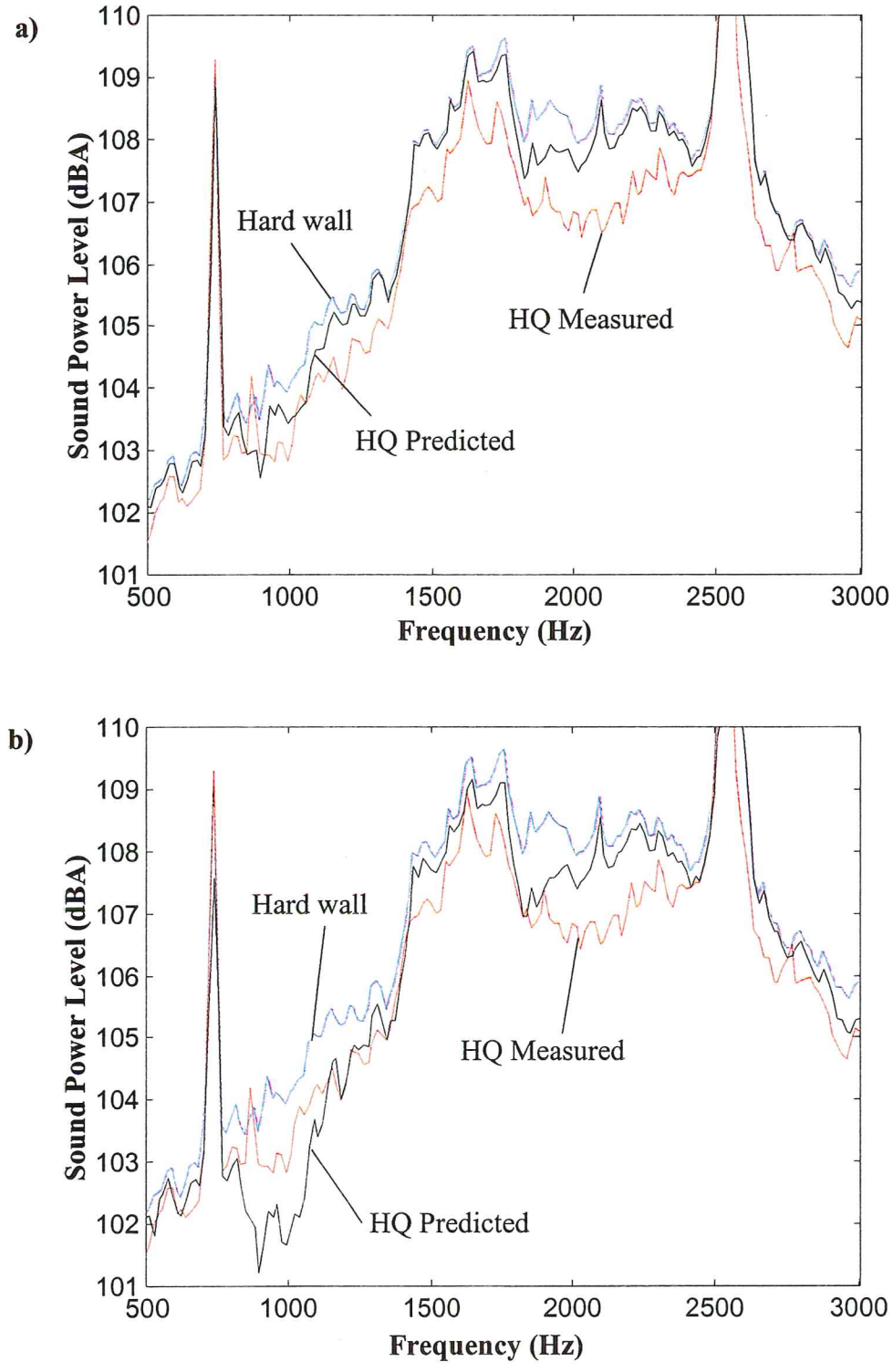

Figure 3.12: Comparison of the predicted and measured sound power levels with one array of 27 tubes mounted on the inlet of the TFE731 engine a) equal modal amplitudes approach b) equal modal power approach.

The average pressure over a piston due to its motion, i.e. input or auto impedance, was first investigated at a frequency of 2320 Hz. The expression for this impedance function is given in Appendix A. Figure 3.13 Shows the magnitude of the impedance as a function of the cumulative number of radial and circumferential modes included in the analysis. Thus, it is important to remark that this figure does not show the individual contributions of each mode to the impedance. For a given number of radial N and circumferential modes M, the corresponding value of the impedance shown in the figure is the sum of the contributions due to all modes (m,n) for $n \leq N$ and $m \leq M$. Therefore, the magnitude of the impedance is expected to converge towards a value, as more and more modes are included. This figure shows that a large number of both radial and circumferential modes is required to achieve convergence of the auto impedance function.

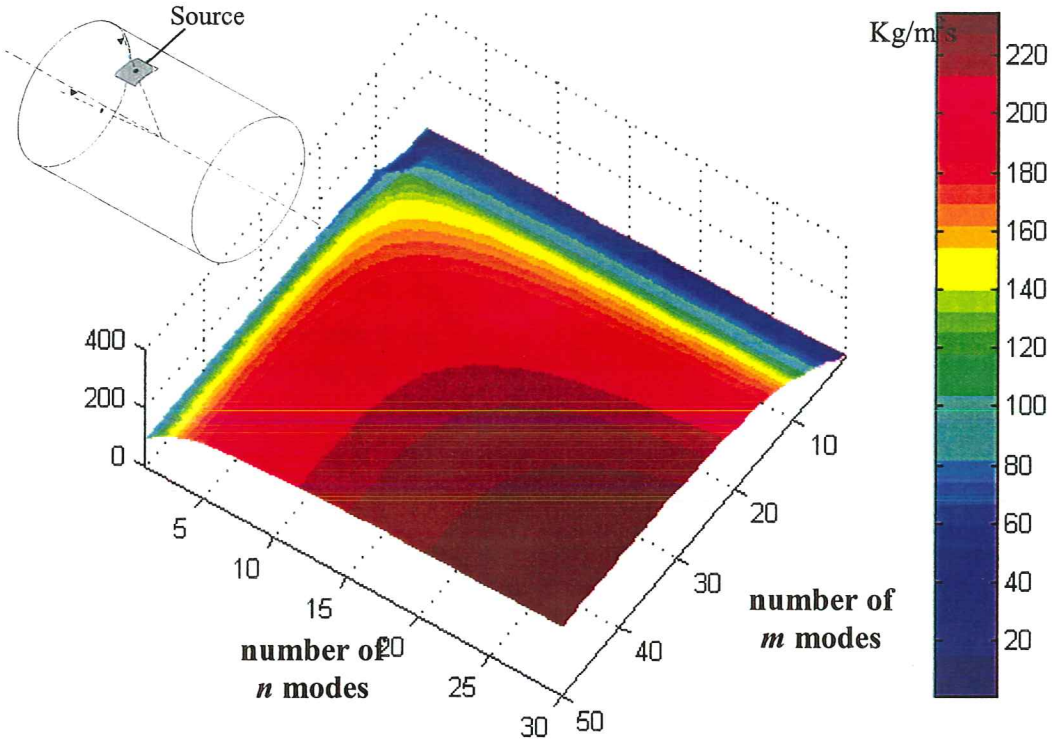

Figure 3.13: Total magnitude of the input impedance function of a piston source.

The impedance of a piston source viewed by another source located upstream at 9.2 cm is shown in Figure 3.14. This figure shows the total magnitude of the impedance function as a function of the radial and circumferential modes included in the computation. As seen in Figure 3.14, the impedance function rapidly converges as more radial and circumferential modes are included in the calculation. A steady value is reached when more than 5 radial and 15 circumferential modes are included. In this configuration, the cut-on modes and modes that are just cut-off have a significant

contribution to the impedance function. However, modes that are well cut-off rapidly vanish and their effect on the observer source 9.2 cm further upstream is negligible.

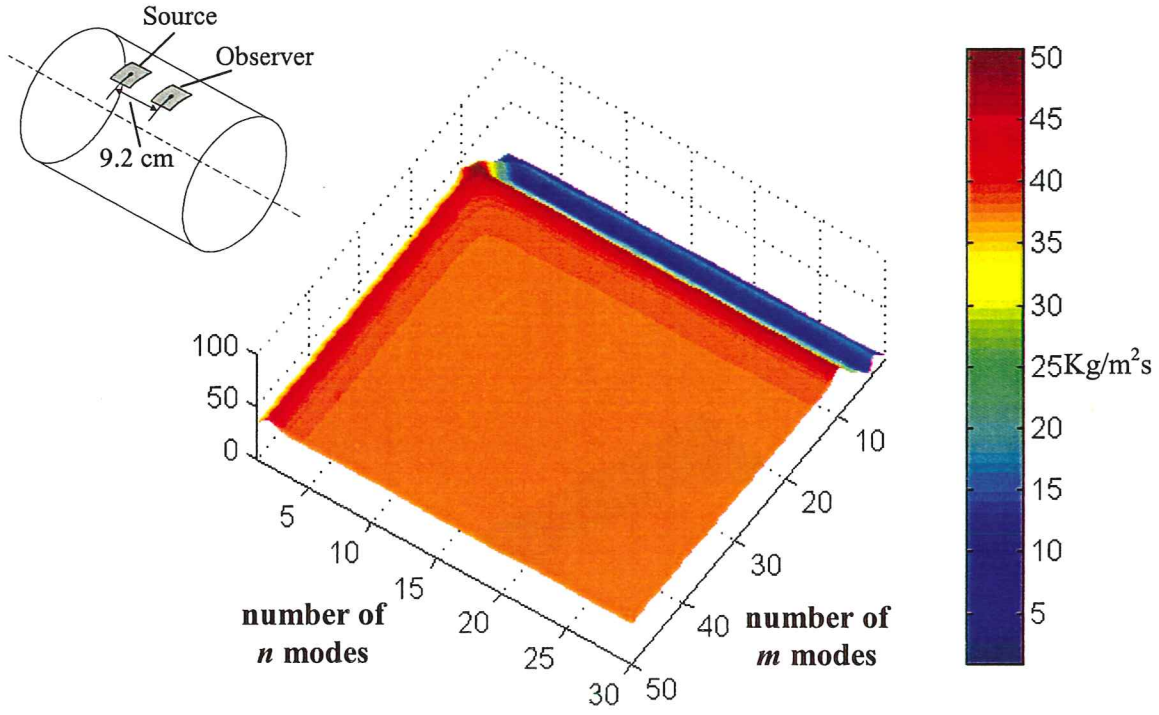

Figure 3.14: Total magnitude of the impedance function of a piston source viewed by another source located upstream at 9.2 cm – BPF frequency is 2320 Hz.

The same study is next performed for an observer source at the same axial location as the "source" piston source but at an angle of 18° relative to the position of the "source" piston. This angle corresponds to the distance between two tubes in the circumference. The magnitude of the impedance in this case is shown in Figure 3.15, as a function of the number of modes included in the calculation. As seen in figure 3.15, when the sources are in the same cross-sectional plane, the number of circumferential modes that need to be included in the calculation to reach convergence is very large. Even if 50 circumferential modes are included, the impedance value is not yet constant. This is due to the fact that cut-off modes have a great influence in this case. Cut-off modes actually decay as they travel along the duct axis; however, these modes do not have a decay characteristic in the azimuth direction. This suggests that a very large number of circumferential modes would need to be included to obtain accurate results. It is interesting to look at the impedance of a piston viewed by another piston on the circumference at higher angles. This is shown in figure 3.16a and b, where the observer source is located at 54° and 90°, respectively. These figures show that even when the spacing between the sources increases, the influence of the cut-off modes remains significant and causes the impedance function to oscillate. However, the magnitude of the

impedance clearly convergences towards a constant value when the number of modes increases. Moreover, including a low number of radial modes is enough to reach the convergence.

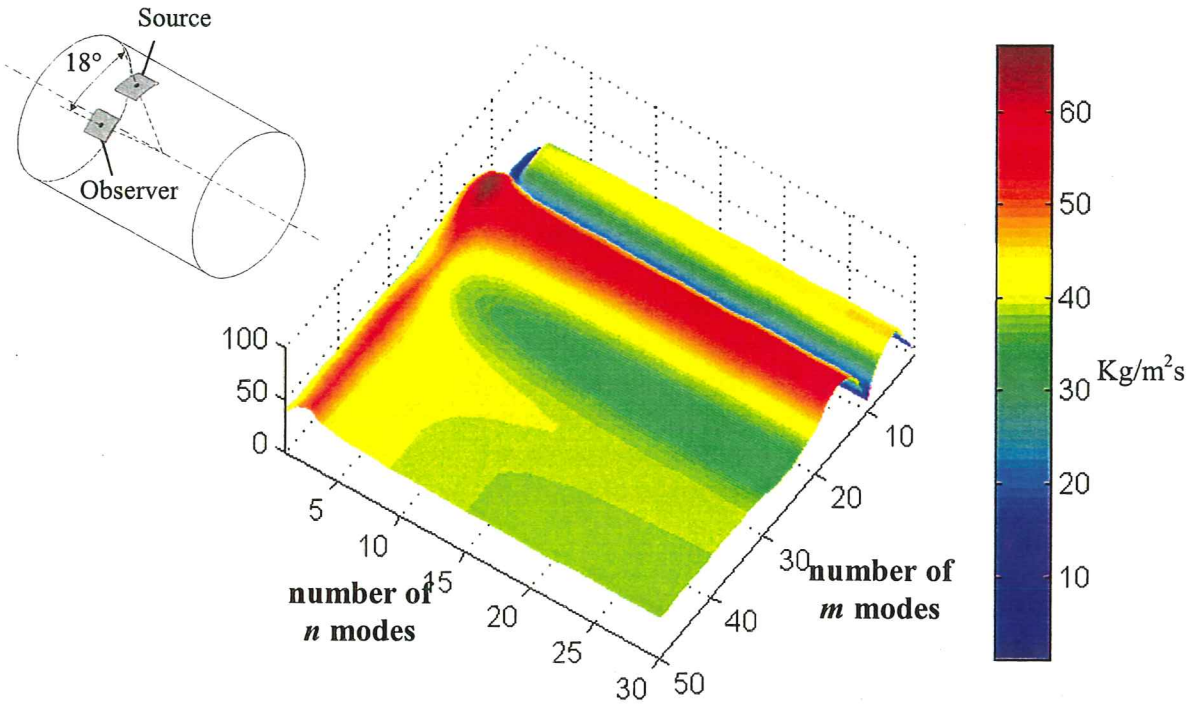

Figure 3.15: Total magnitude of the impedance function of a piston source viewed by another source at 18° in the same cross-sectional plane.

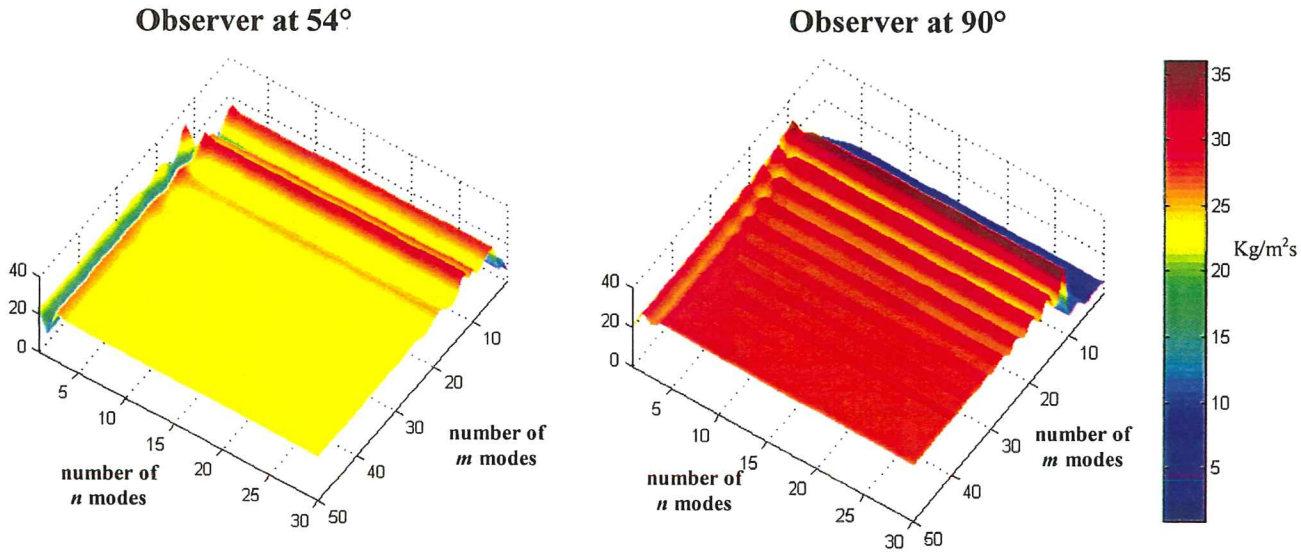

Figure 3.16: Total magnitude of the impedance function of a piston source viewed by another source in the same cross-sectional plane at a) 54° b) 90° apart.

The influence of the number of modes will now be investigated by looking directly at the predicted sound power level. For this study, the HQ system was made of a circumferential array of 20 tubes. The centerline tube length is 11.8 cm and the disturbance is made of three incident mode of order (1,0), (1,1) and (1,2). The effect of the number of modes included in the calculations will be studied individually for radial and circumferential modes. In the first example, the number of circumferential modes was chosen to be very high and the effect of radial modes will be studied. Then, the influence of the circumferential modes will be shown while a high number of radial modes is chosen.

The results of the first study are presented in Figure 3.17 where the sound power reduction is plotted as a function of BPF frequency. There are 40 circumferential modes included in the calculation of the impedance function and the number of radial modes changes from 6 to 40. As seen in Figure 3.17, the number of radial modes included in the calculation does not seem to affect dramatically the sound power reduction level. However, it can be noticed that the optimum frequency of attenuation is slightly shifted down as the number of radial modes increases. In this case, choosing a number of radial modes higher than 20 seems to give reasonably accurate results.

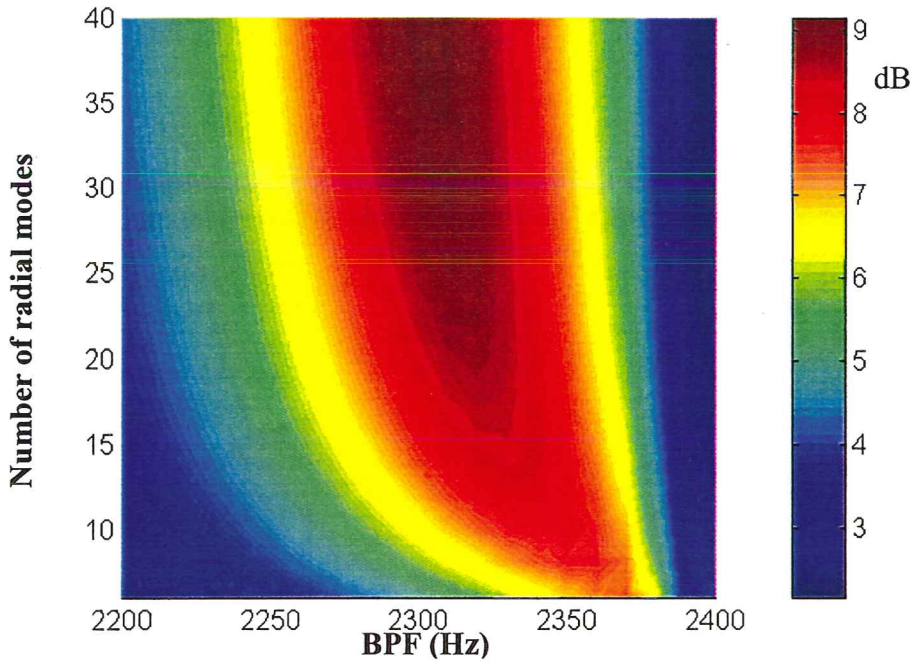

Figure 3.17: Influence of number of radial modes on the sound power reduction when 40 circumferential modes are included in the calculations.

The influence of the total number of circumferential modes is shown in Figure 3.18 where 40 radial modes were included in the computations. Figure 3.18 clearly shows that the sound power reduction level reaches a steady value when more than 22 circumferential modes are included in the computation. Although the contributions of

higher-order modes to the impedance function previously studied was noticeable, including more than 22 circumferential modes does not seem to affect the sound power reduction.

In order to limit the computing time and obtain accurate results, the number of modes included in the calculations in the case of an array of 20 tubes was chosen as 25 circumferential and 20 radial modes unless otherwise specified.

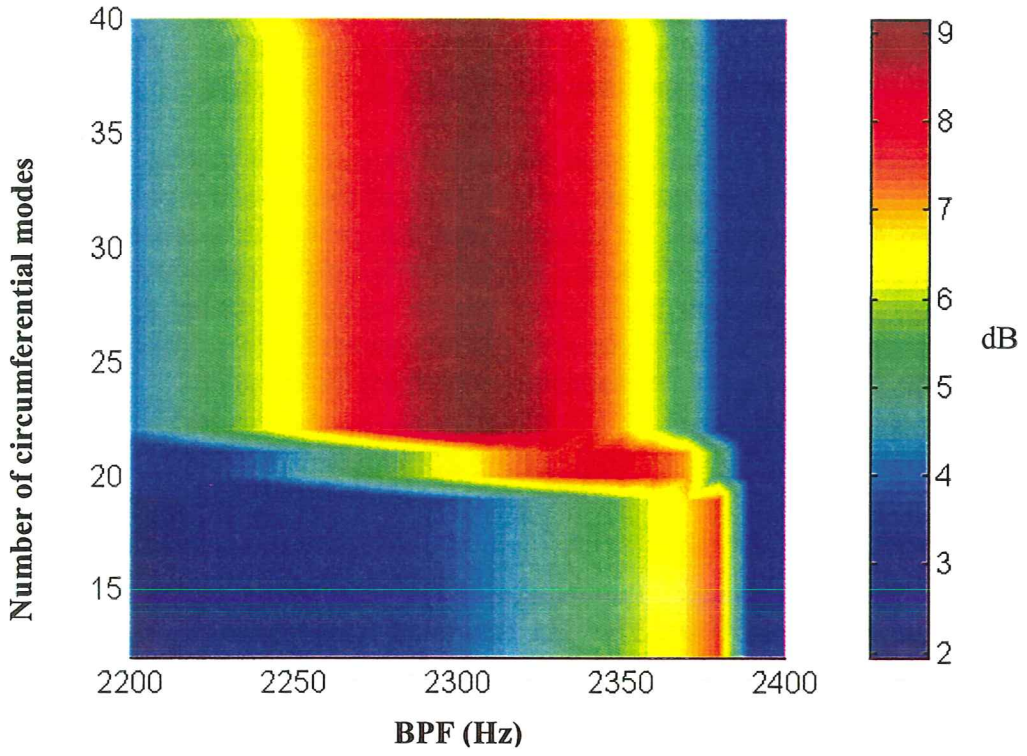

Figure 3.18: Influence of number of circumferential modes on the sound power reduction when 40 radial modes are included in the calculations.

3.5. NOISE CONTROL MECHANISMS

In the previous chapter, the HQ system was shown to be very efficient at reducing BPF tones. Moreover, the modeling approach seems to predict to reasonable accuracy the noise reduction. Therefore, the model will now be used to try to understand the attenuation mechanisms involved in the HQ tubes system.

An impedance study was first performed, where the dynamics of the HQ system were analyzed as a function of the frequency and the resonances of the system were identified. A study of the incident and transmitted modal amplitudes will then illustrate the scattering mechanisms. A HQ system with 20 tubes applied to the JT15D engine first introduced the scattering effect of incident energy between radial modes. A different HQ

system with only 10 tubes is studied next. This system shows that the scattering mechanism not only occurs between radial modes but also among circumferential modes.

3.5.1 Impedance analysis

In this section, an impedance analysis is performed to have a better understanding of the mechanisms involved in the HQ system. The aim of this study is to look at the dynamics of the inlet duct and of the tubes and analyze their interaction. In this study, the HQ tube system consists of a circumferential array of 20 tubes with centerline length 11.8 cm and distance between tube ends 9.2 cm. The engine inlet has a diameter of 0.533 m and the disturbance contains the three modes (1,0), (1,1) and (1,2).

The dynamic of the tubes with perforated screens will first be studied when they are placed in free field conditions. At both ends of the tube, the positive and negative propagating plane waves will be reflected and this reflection mechanism will generate standing waves in the tube. Thus, the HQ tube will exhibit some resonances at discrete frequencies. These resonant frequencies can be computed using the tube impedance matrix in equation (3.3). Due to the pressure release condition assumed at the tube ends, the resonant frequencies are the frequencies satisfying the equation:

$$\det\begin{bmatrix} Z_{ii}^{t\ell} & Z_{io}^{t\ell} \\ Z_{oi}^{t\ell} & Z_{oo}^{t\ell} \end{bmatrix} = 0 \tag{3.25}$$

The first two resonance frequencies of the tube with a perforated screen at both ends are found to be 1370 and 2740 Hz. However, these resonance frequencies are those of a tube placed in free field. In order to investigate the effect of the inlet duct on the tube dynamics, the impedance of the tube placed in the inlet duct was calculated. The following equations allow to compute the impedance at the input and output ends of the ℓ^{th} tube as

$$Z_{\ell i} = \frac{p_{\ell i}^t}{v_{\ell i}^t} = Z_{ii}^{t\ell} + Z_{io}^{t\ell}\frac{v_{\ell o}^t}{v_{\ell i}^t} \tag{3.26}$$

$$Z_{\ell o} = \frac{p_{\ell o}^t}{v_{\ell o}^t} = Z_{oi}^{t\ell}\frac{v_{\ell i}^t}{v_{\ell o}^t} + Z_{oo}^{t\ell} \tag{3.27}$$

where $Z_{ii}^{t\ell}$, $Z_{io}^{t\ell}$, $Z_{oi}^{t\ell}$ and $Z_{oo}^{t\ell}$ are derived in Appendix A and the source velocities $v_{\ell i}^t$ and $v_{\ell o}^t$ are computed from equation (3.5). The tube input impedance is shown in Figure 3.19a as a function of the frequency from 500 to 3500 Hz (the tube output impedance looks very similar). The piston source velocity at this tube end due to the incident modes (1,0), (1,1) and (1,2) is also shown in Figure 3.19b. As seen in Figure 3.19a, the impedance of the piston source drops out at two specific frequencies, at 1040 Hz and 2420 Hz. These frequencies correspond to the resonance of the HQ tube placed in the duct. It can be noticed that the resonant frequencies of this system are different from those of the tube placed in free field (1370 and 2740 Hz). The dynamics of the inlet duct actually changes

the dynamic of the tube, whose resonance frequencies are shifted down. It is clear in Figure 3.19b that the source velocity increases at the resonant frequencies, where the impedance exhibits minimum values. It is important to study how these resonances are affecting the performance of the HQ system. To investigate this, the total sound power reduction provided with 20 HQ tubes was computed and is shown in Figure 3.20.

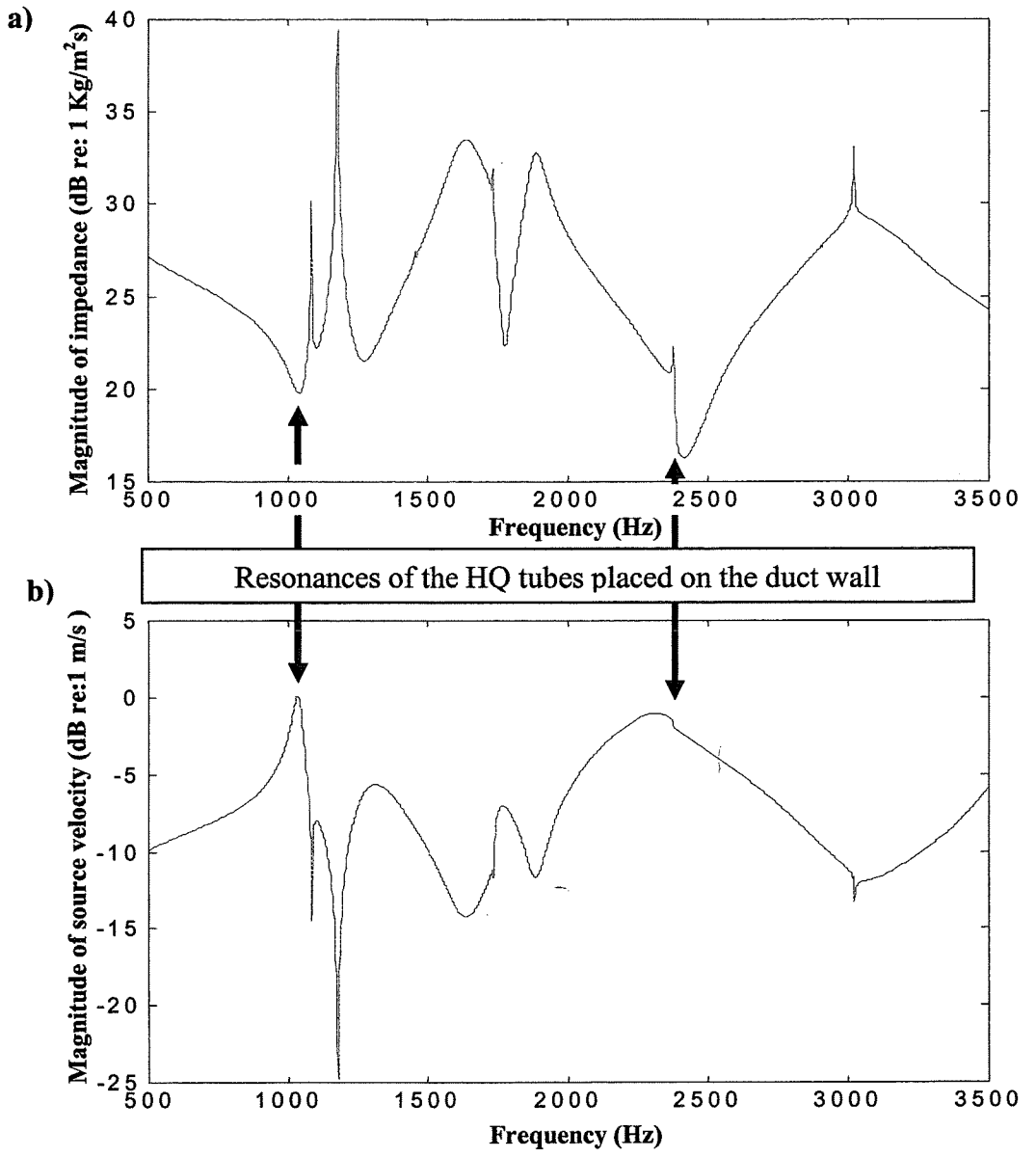

Figure 3.19: a) Input impedance of an 11.8 cm long HQ tube end placed on the duct wall and b) particle velocity of source.

It is interesting to notice in Figure 3.20 that the maximum sound reduction provided by the HQ tube occurs at the frequencies where the source velocity, at the ends of the tubes, shows a maximum, i.e. at 1030 and 2320 Hz. The sound power reduction provided by the HQ tube is 9.5 and 8.6 dB at these two frequencies, respectively. The key idea here is that the HQ system will show good performance at frequencies where the source velocity at the end of the tubes is high, i.e. at the resonant frequencies of the coupled tube-duct system.

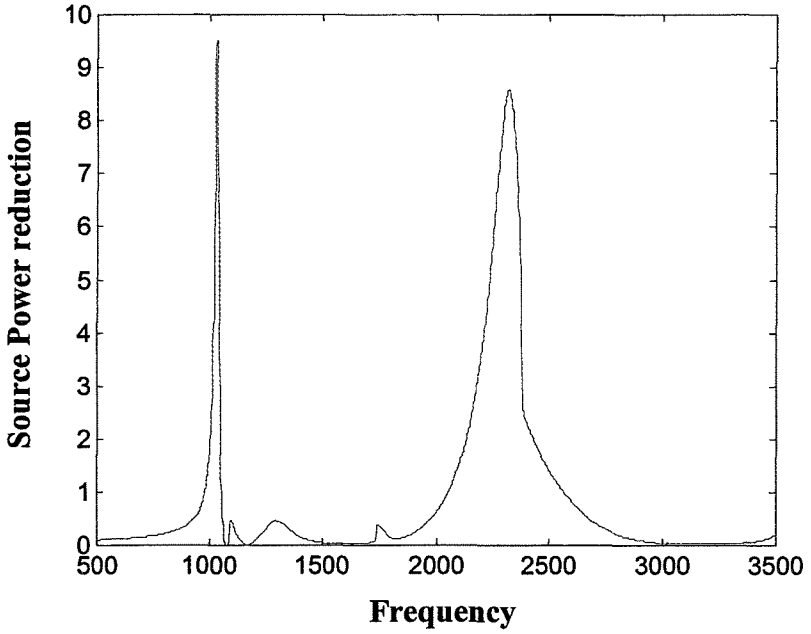

Figure 3.20: Total sound power reduction due to a circumferential array of 20 tubes with three incident modes.

3.5.2 Radial scattering

Previous studies on the control of plane waves with HQ tubes showed that the only attenuation mechanism happening was reflection of the incident energy [7]. The present study focuses on a cylindrical inlet duct in the presence of higher-order modes. In order to have insight into the noise control mechanisms in this case, the modal amplitudes of the incident, reflected and transmitted modes will be investigated.

In this first study, the HQ system consists of a circumferential array of 20 tubes placed 0.4 m upstream from the fan. The incident disturbance is composed of the modes (1,0), (1,1) and (1,2), i.e. all of the same circumferential order m=1, whose complex amplitudes correspond to those measured on the JT15D engine. The effect of the array of 20 tubes on the sound field in the inlet will be investigated here at a BPF frequency of 2320 Hz. The modal amplitudes in Pa are plotted in the complex plane. For the sake of clarity, in the figures showing the modal amplitudes, the black, red and blue colors are

used for the (1,0), (1,1) and (1,2) modes, respectively. These plots allow identifying both the magnitude and phase of the modal amplitudes. Figure 3.21a first shows the amplitudes of the incident fan modes. The transmitted and reflected mode amplitudes due to the HQ system are shown in Figure 3.21b and c, respectively.

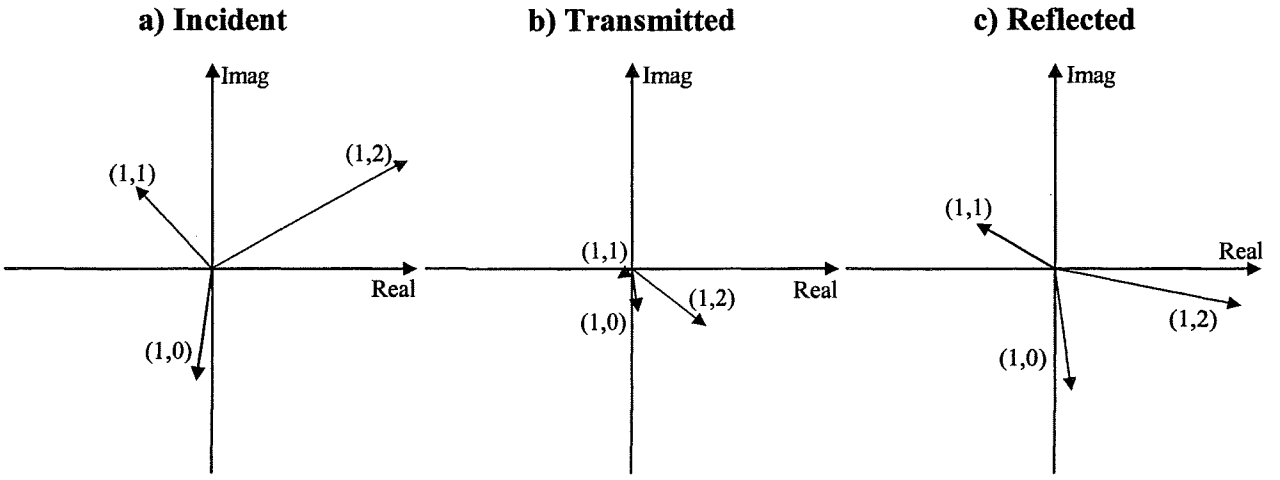

Figure 3.21: Incident, transmitted, and reflected modal amplitudes in the case of 20 HQ tubes applied to the inlet of the JT15D engine.

As seen in Figure 3.21b, the amplitudes of the transmitted modes are reduced as compared to the incident amplitudes in Figure 3.21a. This leads to the reduction of the sound power radiated at the end of the inlet. Since the transmitted mode amplitudes are small, the amount of energy reflected back to the fan is important, as seen in Figure 3.21c. In this case, the HQ tube system is very efficient and provides significant reduction in the sound power. However, an important issue is to investigate how the array of HQ tubes produces the significant reflection of the incident disturbance modes and provides good sound reduction. To this end, a modal breakdown is carried out where the transmitted and reflected mode amplitudes are computed for each of the incident modes propagating individually. The modal breakdowns for each incident mode (1,0), (1,1) and (1,2) are shown in Figure 3-22a, b and c, respectively.

Figure 3.22a shows the incident (1,0) mode amplitude and the resulting transmitted and reflected (1,0), (1,1) and (1,2) mode amplitudes. Figure 3.22b and c show the same breakdown mechanism for incident modes (1,1) and (1,2), respectively. These plots clearly demonstrate that the HQ tube array allows energy in an incident radial mode to be spilled over other radial modes of the same circumferential order. This behavior is referred here as radial scattering effect. These results also demonstrate that there are two mechanisms involved in the reduction of the incident mode. Firstly, the energy in an incident mode is in part reflected back to the fan, and secondly there is some energy scattered into the other radial modes. Figure 3.22 also suggests that there is more energy scattered from the low order into the higher order radial modes than vice versa.

a) Scattering of mode (1,0)

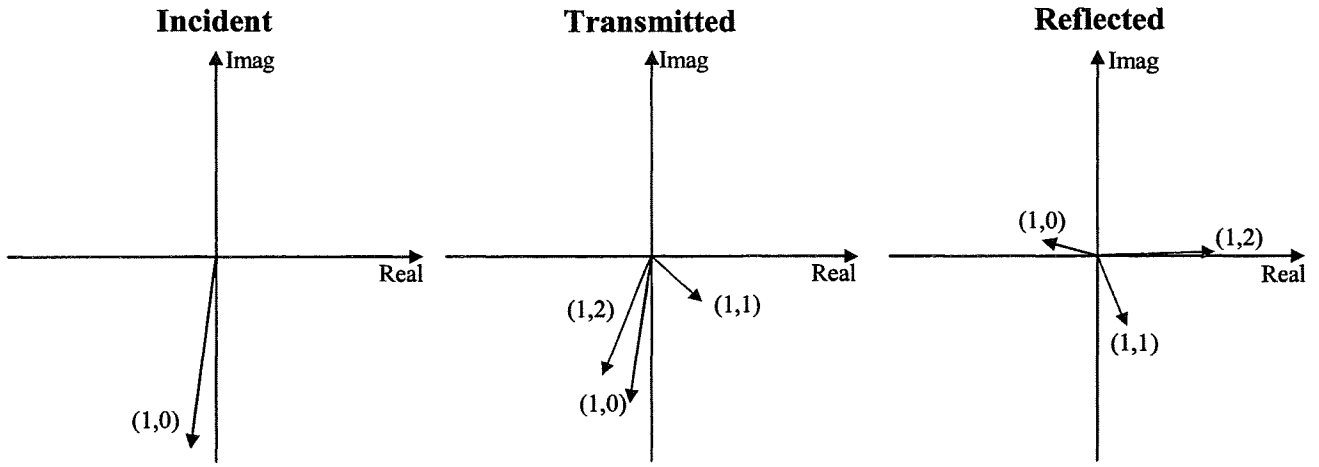

b) Scattering of mode (1,1)

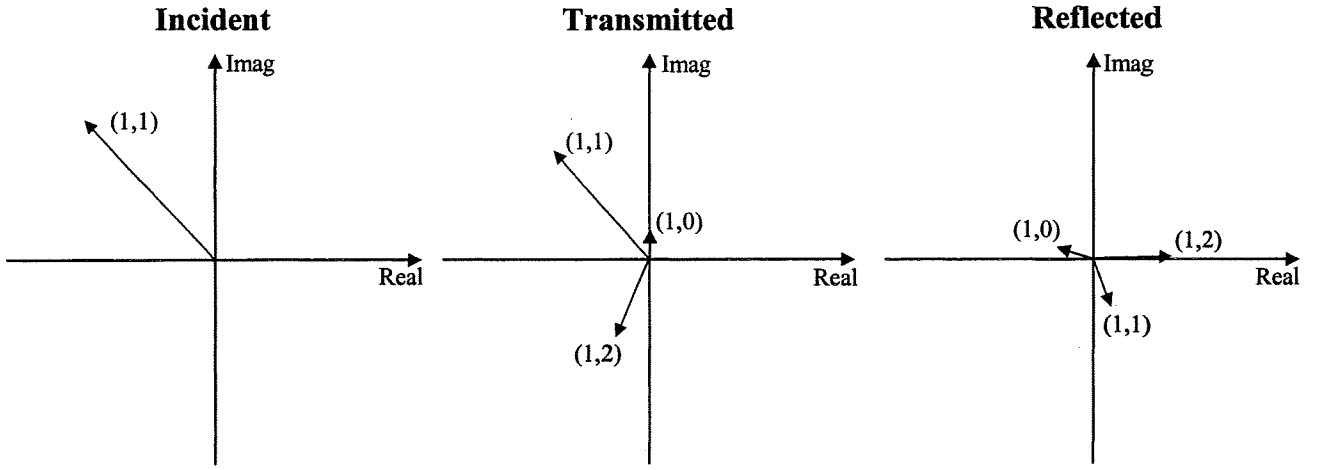

c) Scattering of mode (1,2)

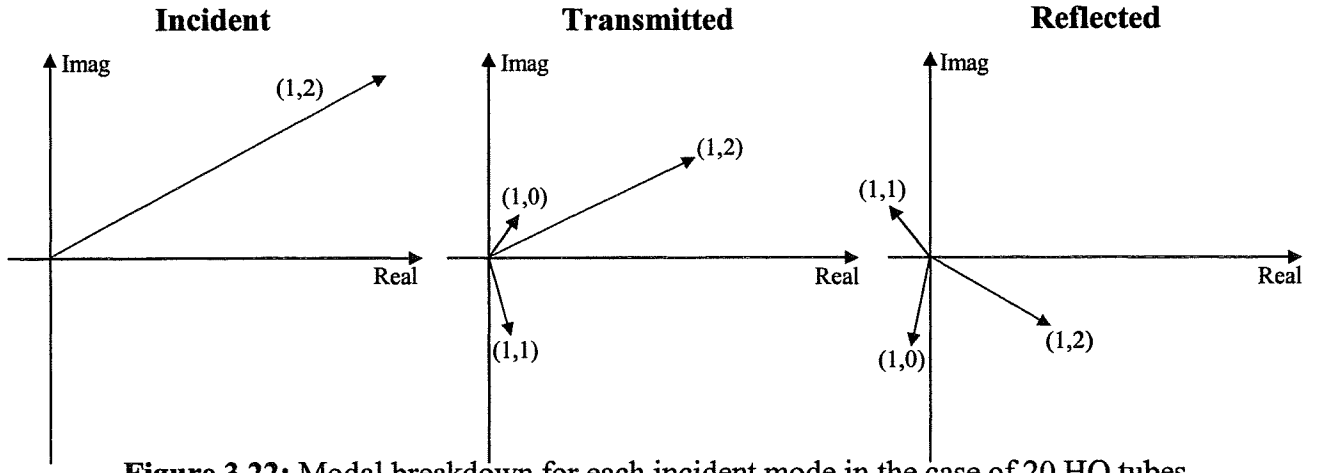

Figure 3.22: Modal breakdown for each incident mode in the case of 20 HQ tubes applied to the inlet of the JT15D engine.

When the three incident modes propagate simultaneously in the inlet duct, the previous scattering effects will happen for each mode and the transmitted and scattered amplitudes will recombine in each mode. Therefore, the suppression of a particular mode is due to the contribution of the scattered energy from other modes. As an example of this mechanism, Figure 3.23 illustrates the suppression of mode (1,1). As shown in Figure 3.23 (enlarged scale), the transmitted component in mode (1,1) recombines with the scattered components from modes (1,0) and (1,2). The total transmitted amplitude in mode (1,1) is simply due to the vector summation of all these components. Therefore, it can be noticed that this recombination occurs in an optimal way and provides large reduction of the incident mode amplitudes.

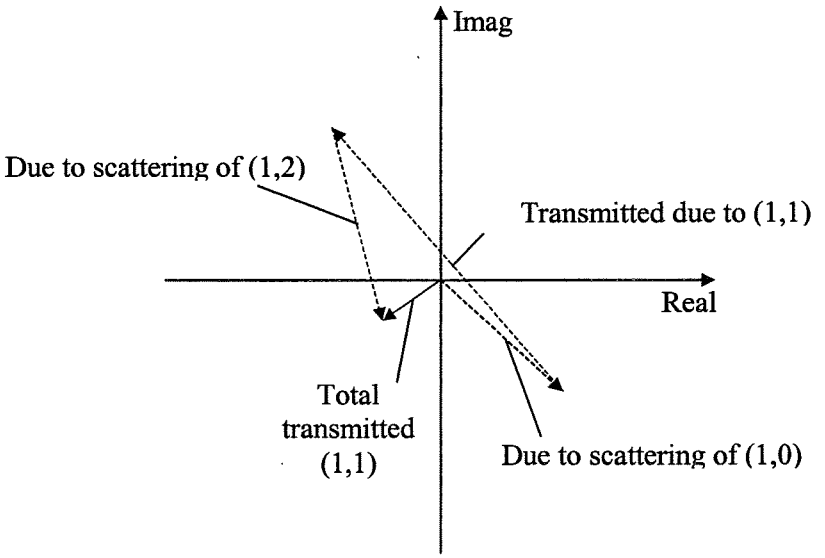

Figure 3.23: Suppression of mode (1,1).

This study allows to show that the main noise control mechanisms involved in the HQ system with 20 tubes are reflection of incident energy and recombination of scattered energy in each radial mode. This behavior should be contrasted to the traditional analysis of the HQ tube to the plane wave where the only noise reduction mechanism that takes place is reflection of the incident wave. Thus, the scattering effect between radial modes and their recombination to yield noise reduction is a new mechanism for HQ tubes in the presence of multiple duct modes.

3.5.3 Circumferential Scattering

In the previous section, it was shown that the noise attenuation mechanisms for an array of tubes involve reflection of the modes back towards the fan, as well as modal scattering and recombination among radial modes of same circumferential order m. It was assumed that all the modes present in the duct had the same circumferential order m_D as the disturbance. However, for a given input disturbance mode with circumferential order m_D, some of the modes present in the duct with the HQ tubes system can have circumferential order different than the disturbance m_D. This effect takes place because of the spatial alliasing due to the discrete number of tubes in the array. The circumferential order of the modes present in a HQ system are predicted by

$$m_{HQ} = m_D \pm kN_T \tag{3.28}$$

where N_T is the number of tubes in the array and k is any integer, i.e. $k=0, 1, 2, 3,\ldots$ Equation (3.28) shows that given an incident disturbance mode of order m_D, acoustic energy will result in modes with circumferential order m_{HQ} (if they are cut-on). Thus, some energy from the m_D disturbance mode will be scattered into m_{HQ} circumferential modes, which is referred to as circumferential scattering.

A simple example can be used to illustrate this circumferential scattering. Assume the disturbance mode is of circumferential order m_D=4 and there are 8 HQ tubes. The tubes will be driven by the disturbance mode and the particle velocity between tubes will have the same magnitude but the phase between adjacent tubes will be 180°. This is shown in the schematic of Figure 3.24. Selecting k=2 from equation (3.28) gives $m_{HQ} = 4 - 2\times 8 = -12$. Therefore, a mode of circumferential order 12 and spinning in the opposite direction as the disturbance mode, will be excited by the HQ system.

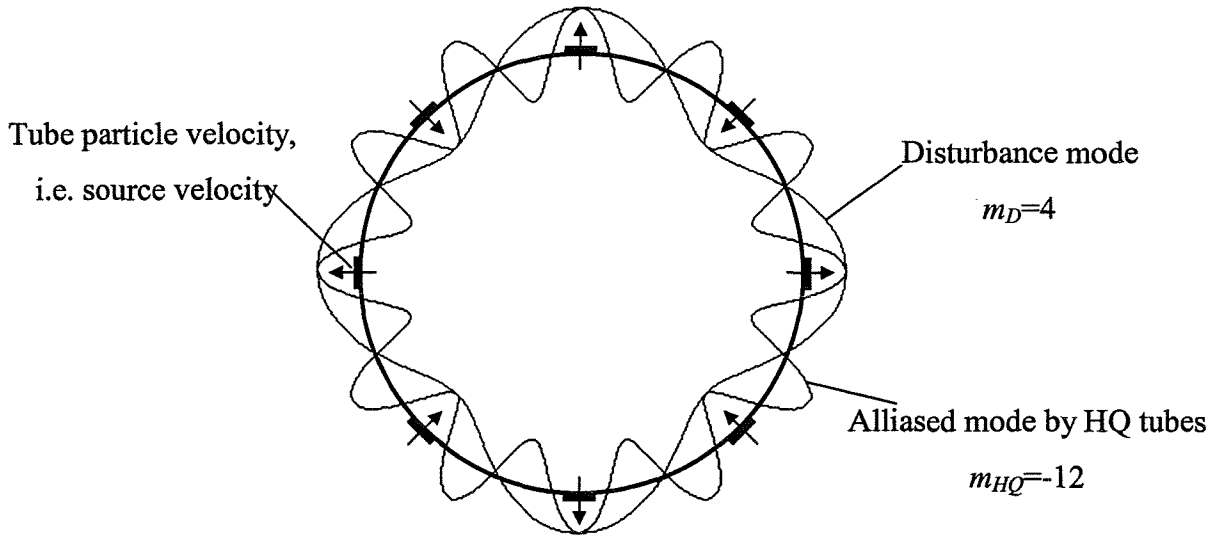

Figure 3.24: Spatial alliasing due to an array of 8 tubes with a disturbance mode of circumferential order m_D=4.

Thus, the previous effect leads to two possible design strategies for the HQ tubes system. First, the number of tubes can be designed to be sufficient enough so that there is no acoustic content scattered into cut-on m-order modes at the frequency of analysis. On the other hand, the number of tubes can be selected such that additional m-orders are excited by the HQ tube system (i.e., m_{HQ} for $k \neq 0$ that are cut-on). Results from these two different design approaches will be investigated here.

In this example, the disturbance again contains modes (1,0), (1,1) and (1,2) at a frequency of 2320 Hz and the mode amplitudes are those measured on the JT15D engine. The sound reduction results provided by two different HQ systems are investigated. The first system contains 20 tubes and the second has only 10 tubes. The efficiency of both

systems is measured in term of the total sound power reduction and is shown in Table 3-5. This table also shows the reduction in each propagating transmitted mode.

Table 3-5: Modal and total Sound Power reduction in dB for arrays of 20 and 10 HQ tubes applied to the inlet of the JT15D engine.

Mode	20 Tubes	10 Tubes
(1,0)	8.0	1.6
(1,1)	16.4	2.6
(1,2)	7.5	4.2
(-9,0)	*Not present*	-113.6
Total	8.6	1.1

The transmitted modal content for the inlet with 20 tubes is shown in the second column of Table 3-5. It shows a sound power reduction of 8.0, 16.4 and 7.5 dB of the three radials, (1,0), (1,1) and (1,2), respectively, for an overall reduction of 8.6 dB. The lowest m-order mode excited by the 20 tubes system is $m_{HQ}=-19$ (see equation (3.28) and Table 3-1), which is cut-off at 2320 Hz. Thus, the only modes present with the HQ tubes system are those modes that were present in the disturbance (no scattering between m-order modes). The noise control mechanisms happening in this case are only the reflection of incident energy and recombination of scattered energy among the three radial modes. As seen in this table, the HQ system is very efficient in this case.

On the other hand, the transmitted modal content for the inlet with 10 tubes is shown in the third column of Table 3-5. In this case, there is energy scattered into mode (-9,0) from the incident modes (1,0), (1,1) and (1,2) ($m_{HQ}=-9$ for $k=-1$ in equation (3.28) and Table 3-1). The results show a power reduction of 1.6, 2.6 and 4.2 dB for the (1,0), (1,1) and (1,2) modes, respectively. Note that there is now 113.6 dB of acoustic content in the (-9,0) mode. The overall noise reduction is now only 1.1 dB. That is, the overall reduction is greatly diminished with only 10 tubes (allowing scattering effects between m-order modes) as compared to 20 tubes (without scattering).

To examine in depth the scattering mechanisms taking place here, the modal breakdown will be shown for both systems. Figure 3.25a and b show the modal breakdown of the incident mode (1,1) in the case of an array of 20 and 10 HQ tubes, respectively. In Figure 3.25, the straight red line represent the amplitude of incident mode (1,1), whereas the dashed lines show the transmitted amplitudes in the scattered modes (1,0), (1,1), (1,2) and (-9,0). By comparing both plots in Figure 3.25a and b, it is clear that a significant portion of the incident mode (1,1) energy scatters into the (-9,0) mode and that the amount of energy scattering from the (1,1) to the other radial modes is very small in the case of 10 tubes. It can also be noticed that the transmitted amplitude in mode (1,1) is smaller in the case of 20 tubes.

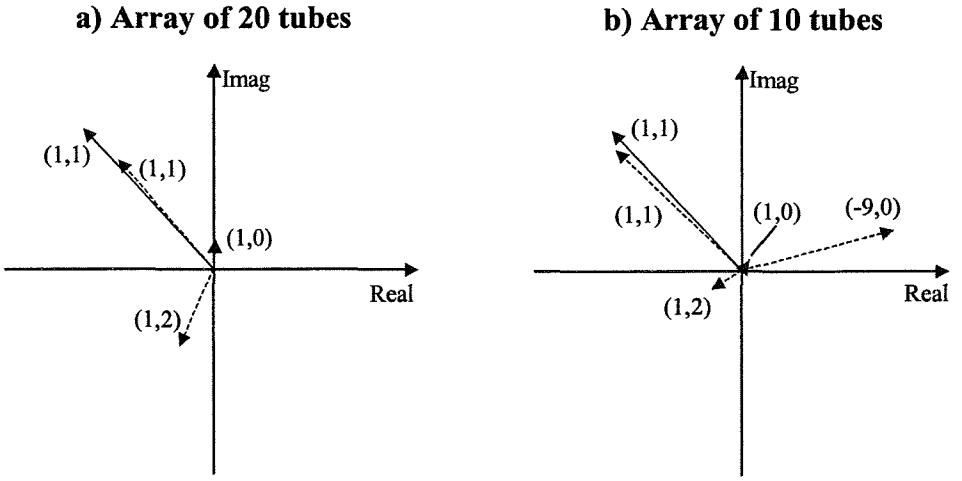

Figure 3.25: Scattering of mode (1,1) with an array of 20 or 10 HQ tubes applied to the inlet of the JT15D engine.

As the scattering mechanism depends on the number of tubes in the system, the recombination of energy in each mode will obviously be different for both systems. The modal recombination of scattered energy for the suppression of mode (1,1) in the case of 20 and 10 HQ tubes is shown in Figure 3.26.

It is clear in Figure 3.26 that the recombination mechanism is less effective with 10 tubes than in the case of 20 tubes. When scattering into other *m*-order modes is allowed, the attenuation mechanism provided by the recombination of scattered energy is severely reduced.

This analysis showed that scattering the acoustic content only among radial modes by using a high number of tubes results in significant cancellation of the radial modes. On the other hand, allowing the energy to scatter to another *m*-order mode by choosing a low number of tubes reduces the effect of the HQ tube's phase cancellation mechanism. Thus, the scattering and recombination of acoustic energy among radial modes of a single circumferential order is shown to be a primary mechanism of attenuation.

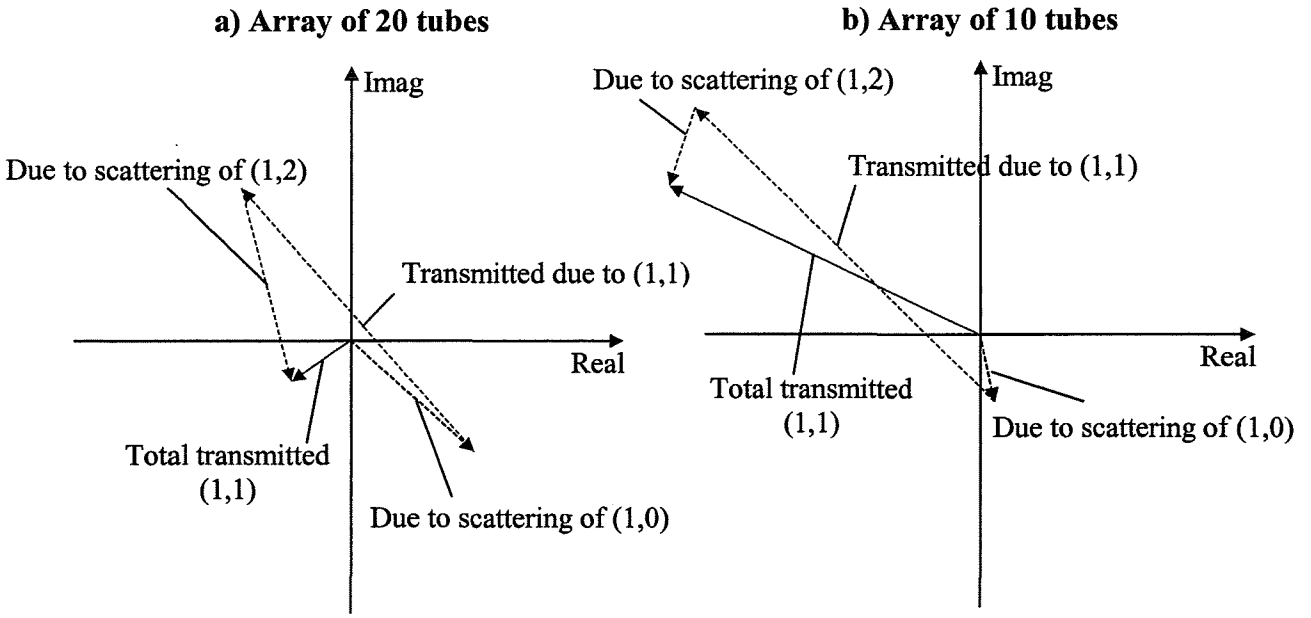

Figure 3.26: Suppression of mode (1,1) with 20 and 10 HQ tubes applied to the inlet of the JT15D engine.

In the previous analysis, the disturbance only contained modes of the same circumferential order $m=1$. In this case, the energy scattered into the other circumferential order mode causes an increase in the sound radiation. An interesting issue would be to investigate the effect of this scattering mechanism in the case of incident modes of different circumferential order. This is the case of the Honeywell engine, where incident modes of circumferential orders –8, 2 and 12 simultaneously propagate at the BPF of 2250 Hz. In this case, an array of 10 tubes would allow scattering of energy from one circumferential mode into the other two and if the recombination of energy in each mode happens optimally, this HQ system could eventually be very effective. Therefore, one can wonder if allowing the scattering into circumferential modes could, in this case, result in better performance than with a system with a high number of HQ tubes. In order to answer this question, a system with 27 tubes will be compared to a system with only 10 tubes. In the case of 27 tubes, there is no scattering of energy between circumferential modes but only into cut-on radial modes. The dimensions of the tubes (centerline length and distance between tube ends) in both cases were optimized using genetic algorithms to provide maximum reduction at 2250 Hz. In the case of 27 tubes, the centerline tube length was found to be 12.3 cm and the distance between tube ends 6.6 cm. In the case of 10 tubes, the centerline tube length is 11.4 cm and the distance between tube ends is 6.2 cm. The tube cross-sectional areas were chosen in both systems to keep the cross-sectional area ratio equal to 0.1. The result of this study is shown in Figure 3.27.

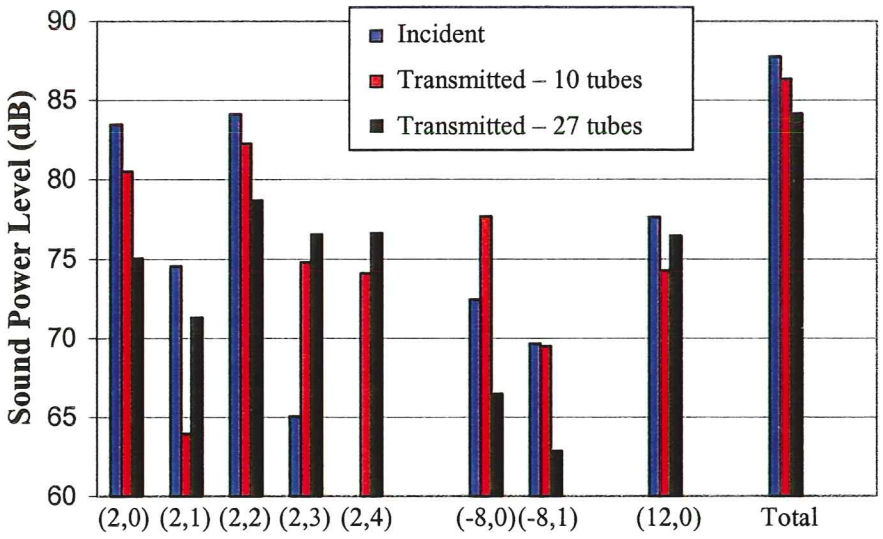

Figure 3.27: Modal and total sound power reduction for arrays of 27 and 10 HQ tubes applied to the Honeywell engine at 2250 Hz.

As seen in Figure 3.27, the total sound power reduction is 1.4 dB with 10 tubes and 3.7 dB with 27 tubes. Therefore, the system with a higher number of tubes (no scattering into circumferential modes) allows to achieve a better total sound power reduction. Although the system with 10 tubes was optimized to provide maximum reduction at 2250 Hz, it still has lower performance than the system with 27 tubes. Therefore, allowing the scattering between circumferential modes did not allow for an increase in the sound power reduction.

After looking at the individual transmitted modal amplitudes, the following conclusions could be drawn. When the number of tubes is high enough to avoid scattering into other m order modes, the reflection of the incident energy is more important as well as the scattering effect between radial modes. On the other hand, when scattering into circumferential modes is allowed (by having a low number of tubes), the reflection effect is less important and more energy tends to be scattered into circumferential modes than in radial modes. Another interesting conclusion is that the scattering into circumferential modes effect tends to be more important from low order into higher-order modes than vice-versa. This mechanism was observed previously in the case of scattering between radial modes. These conclusions were made by investigating the amplitudes of the transmitted modes with only one incident mode propagating at a time. These amplitudes are not shown here to avoid getting into too much complexity. However, these conclusions are illustrated in Figure 3.27 and will be explained next.

As seen in Figure 3.27, modes (2,0) and (2,2) show great reduction with 27 tubes. This is due to the important reflection of the incident energy in these two modes and also to a good recombination of the scattered energy from all the other modes. However, the energy transmitted in modes (2,3) and (2,4) is higher in the case of 27 tubes. This is due to the fact that more energy is scattered into these modes with 27 tubes and the scattered

energy does not recombine optimally. Modes (8,0) and (8,1) show very little reduction or even increase in the transmitted sound power level with 10 tubes. This is mainly due to the important scattering of energy from modes of circumferential order $m=2$. Finally, mode (12,0) shows a better reduction in the case of 10 tubes. In this case, an important part of the incident content in this mode is scattered into all the other lower-order modes, largely reducing the amount of energy left in this mode; whereas with 20 tubes, the only reduction happening is due to reflection.

The previous study illustrated the main noise control mechanisms involved with the HQ system. A new mechanism takes place in the case of higher-order modes, i.e. not only is the incident energy reflected as in the plane wave case, but recombination of scattered energy and phase cancellation also contributes to the noise reduction. The number of tubes was shown to be a determinant criterion governing the scattering process. In general, the HQ system tends to show better performance with a higher number of tubes. In this case, the propagation of energy into other circumferential order modes can be avoided and the only scattering effect occurs between radial modes. However, it is important to remark that these conclusions are applicable only in the case of a hard-wall inlet. If the HQ tubes are combined with a liner, it could be very effective at scattering energy into m-order modes, which the liner can effectively attenuate.

3.6. ADVANCED HQ SYSTEM CONFIGURATIONS

In previous studies, the tubes considered were parallel to the inlet axis and placed in a circumferential array, each tube being at the same axial location upstream from the fan and distributed evenly around the circumference. However, the acoustic field inside the inlet is made up of rotating modes, each of them contributing to the total sound radiation. These modes are spinning as they propagate upstream from the fan; in other words, they are propagating inside the inlet in helix patterns. Therefore, placing the HQ tubes along helixes instead of having a circumferential array of tubes could lead to an improvement in the performance of the HQ system. The effectiveness of the system could eventually be better when the angle of the helical array of tubes matches the angle of propagation of the incident modes. This issue will be investigated in the next sections.

First, the characteristics of the modes propagating along a helix will be explained. The equation relating the value of the helix angle to the mode order and the frequency of analysis will thus be presented. Then, three different systems will be investigated based on this helix propagation idea. First, the HQ tubes will be placed in a helix pattern while the tubes are lined up with the engine axis. The effect of this system will be studied for a range of frequencies. Since the angle of propagation of a mode along a helix is directly related to the frequency of analysis, this will allow the investigation of cases where the angles of propagation of the modes are different. Then, the HQ tubes will be placed in a circumferential array while the tubes are at an angle with respect to the engine axis.

Finally, both systems will be combined and the tubes will be placed in a helix pattern while each tube is rotated at the same angle as the helix.

3.6.1 Propagation of modes along a helix

The propagation characteristics of a mode in the engine inlet are governed by the total wavenumber k_T. The total wavenumber can be expressed as the vector summation of the axial and the circumferential wavenumbers. Figure 3.28 shows the helix along which a mode of circumferential order m will propagate.

For a positive traveling mode, the axial wavenumber takes the form

$$k_z = \frac{-Mk_o + \sqrt{k_o^2 - (1-M^2)k_{mn}^2}}{1-M^2} \tag{3.29}$$

where M is the flow Mach number, k_o is the free field wavenumber ($k_o=\omega/c$), k_{mn} is the eigenvalue written as $k_{mn}=\chi_{mn}/a$, where χ_{mn} are the inflection points of the Bessel's function of the first kind of order m.

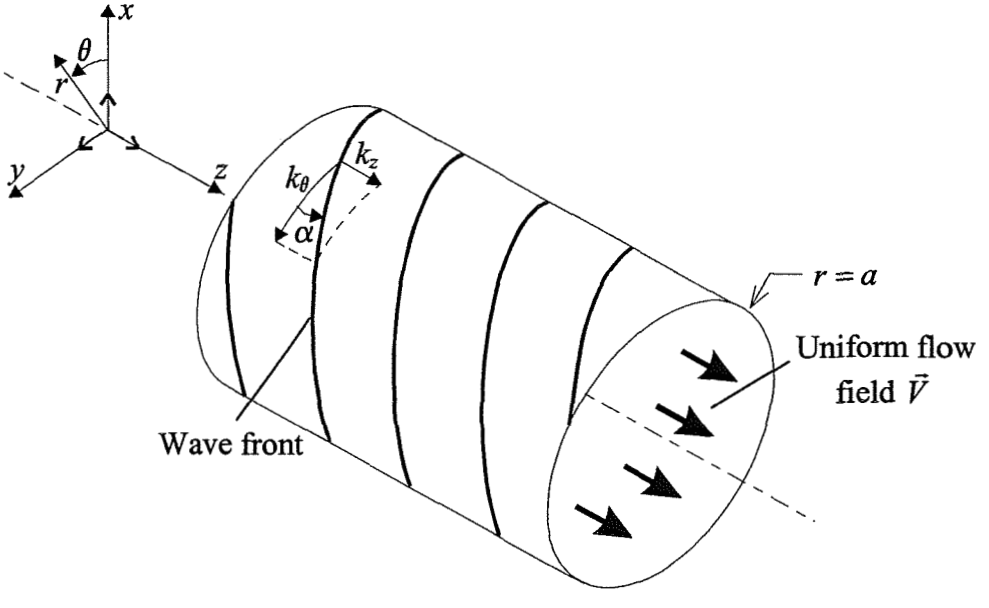

Figure 3.28: Propagation of mode in the inlet along a helix.

On the other hand, the circumferential wavenumber k_θ depends on the circumferential order m of the mode, i.e.the number of pressure lobes along the circumference. Therefore, the circumferential wavenumber is given as

$$k_\theta = \frac{2\pi}{\lambda_\theta} = \frac{2\pi}{\left(\frac{2\pi a}{m}\right)} = \frac{m}{a} \tag{3.30}$$

As defined in Figure 3.28, the angle of the helix α is given as

$$\alpha_{mn} = \tan^{-1}\left[\frac{k_z}{k_\theta}\right] = \tan^{-1}\left[\frac{\left(\frac{-Mk_o + \sqrt{k_o^2 - (1-M^2)k_{mn}^2}}{1-M^2}\right)}{\left(\frac{m}{a}\right)}\right] \tag{3.31}$$

As shown in equation (3.31), since k_z depends on the order of the mode considered, the angle of propagation will be different for each mode. For this study, the HQ system will be applied to the JT15D engine inlet at the frequency of 2320 Hz. At this frequency, there are 21 cut-on modes. The angle of propagation α_{mn} for each mode is shown in Table 3-6 as a function of its circumferential order m and radial order n.

Table 3-6: Angle of propagation α in degree for each cut-on mode at 2320 Hz.

		Radial order n			
		0	**1**	**2**	**3**
Circumferential order m	**0**	90.0	90.0	90.0	90.0
	1	85.4	85.0	83.6	-
	2	80.7	79.2	73.8	-
	3	75.8	72.3	44.2	-
	4	70.6	63.3	-	-
	5	65.0	48.9	-	-
	6	58.8	-	-	-
	7	51.6	-	-	-
	8	42.8	-	-	-
	9	30.3	-	-	-

As modes of circumferential order $m=0$ are not spinning, they are not propagating along a helix, therefore the angle of propagation is 90°, as shown in Table 3-6. It can also be noticed that the angle of propagation of modes is very high and decreases as the order of the mode increases. This is due to the fact that the angle of the helix is directly related to the frequency. When a mode is just cut-on, the angle is 0°, and as the frequency increases, the angle will tend to approach 90°.

3.6.2 Array in a helix pattern with tubes parallel to the engine axis

In this section, the tubes will be placed along the inlet duct such that the array of tubes has a helix shape. As previously explained, the angle of the helix is measured from an axis perpendicular to the engine axis, such that an angle of 0° corresponds to a circumferential array. The angle of the helix defined by the array of tubes will be changed and the effect on the sound power reduction will be observed. The first case investigated here will consist of placing the tubes to form 4 helixes, each of them being made of 5 tubes. The reference system is a circumferential array of 20 tubes of length 11.8 cm. Figure 3.29 shows an unwrapped view of the inlet mounted with a circumferential array of tubes and with the HQ tubes placed in helix patterns. There are several possible options to place the tubes in helixes based on the reference system. Two configurations will be studied here. First the distance between the tubes in the circumferential direction will be kept constant as the angle of the helix changes. Then, the distance between the tube ends is kept constant as the angle of the helix changes. These two cases are illustrated in Figure 3.30a and b and will be referred to as configuration 1 and configuration 2 in the next paragraphs.

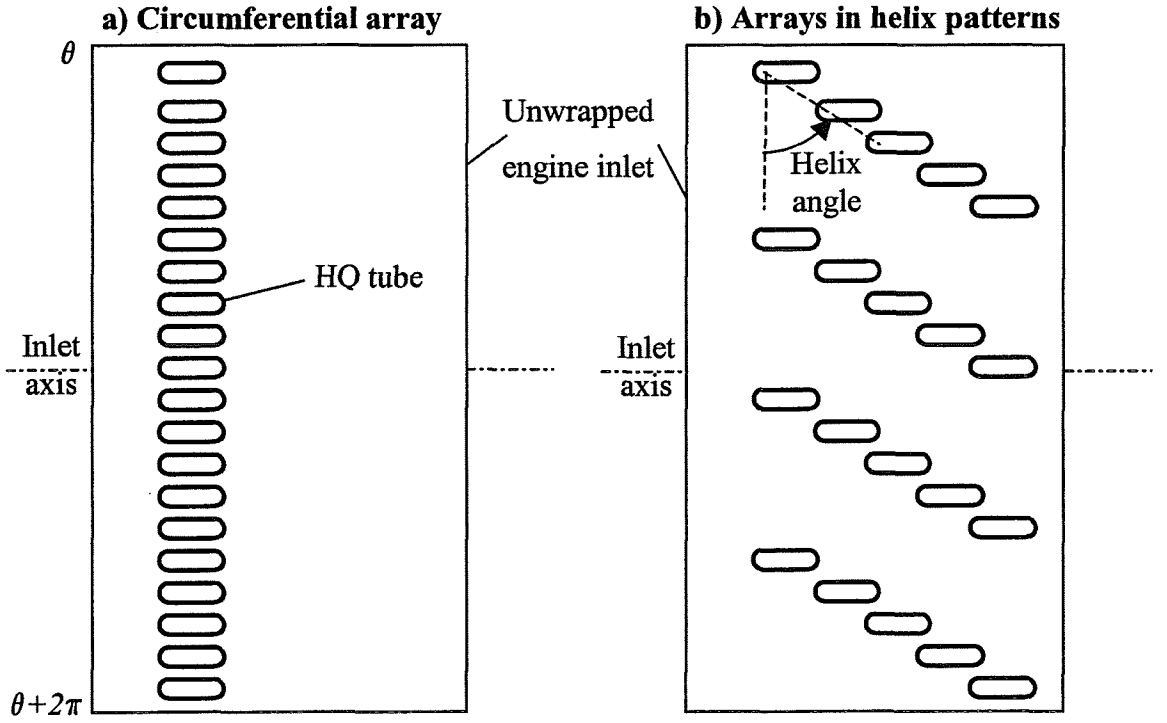

Figure 3.29: Expanded view of the inlet with HQ tubes placed a) in a circumferential array or b) in 4 helixes of 5 tubes.

a) Configuration 1: Constant distance between tubes in circumferential direction

b) Configuration 2: Constant distance between tube ends in same helix

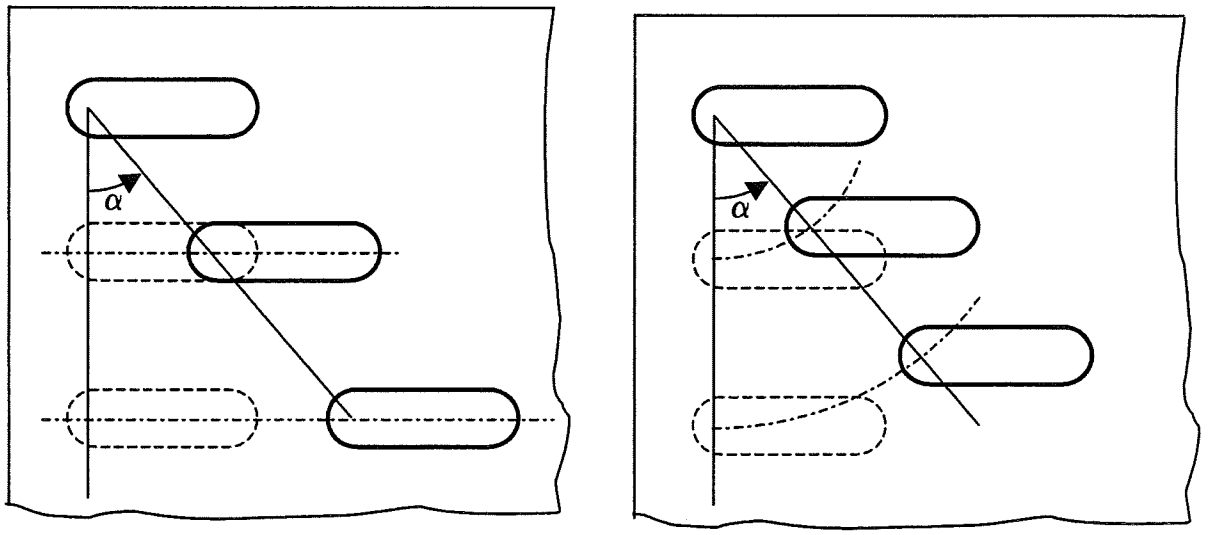

Figure 3.30: Configurations used to place tubes in helix patterns.

For the simulations performed here, the disturbance contains 3 modes, (1,0), (1,1) and (1,2) whose amplitudes are those measured on the JT15D engine at 2320 Hz. However, besides the case of the disturbance containing these 3 modes simultaneously, the effect of the helix angle will be investigated for the three modes individually propagating in the inlet. Results for the configuration 1, i.e. constant distance between tubes in circumferential direction, are illustrated in Figure 3.31. This figure shows the sound power reduction as a function of the helix angle. The angles of the helix range from –85° to 85°. This range was selected to theoretically investigate the effect of the helix arrays on the performance of the system and see if there is a trend. However, the required inlet length for such large angles would not be practical (4 meters for helixes at 85°) making such systems physically unrealizable. Figure 3.31 shows that the maximum sound reduction occurs with a circumferential array of tubes, i.e. when the helix angle is 0°. With the three incident modes, the sound power reduction suddenly drops from 12 dB to less than 2.5 dB when the tubes are placed in helixes. In the case of the incident modes individually propagating in the inlet, there is no improvement of the reduction observed when the tubes are placed in helixes either.

As shown in the previous section, incident modes (1,0), (1,1) and (1,2) propagate through the inlet along helixes of angles 85.4°, 85.0° and 83.6°, respectively, at 2320 Hz. These angles are extremely high and are almost out of the range for the helix angles investigated here. However, placing the tubes at angles of 80° or 85° does not seem to provide any improvement in the sound reduction here. Results for configuration 2, i.e. constant distance between tube ends in the same helix, are shown in Figure 3.14. In this case, the helix angles range from –60° to 60°, which corresponds to the maximum possible range for the system.

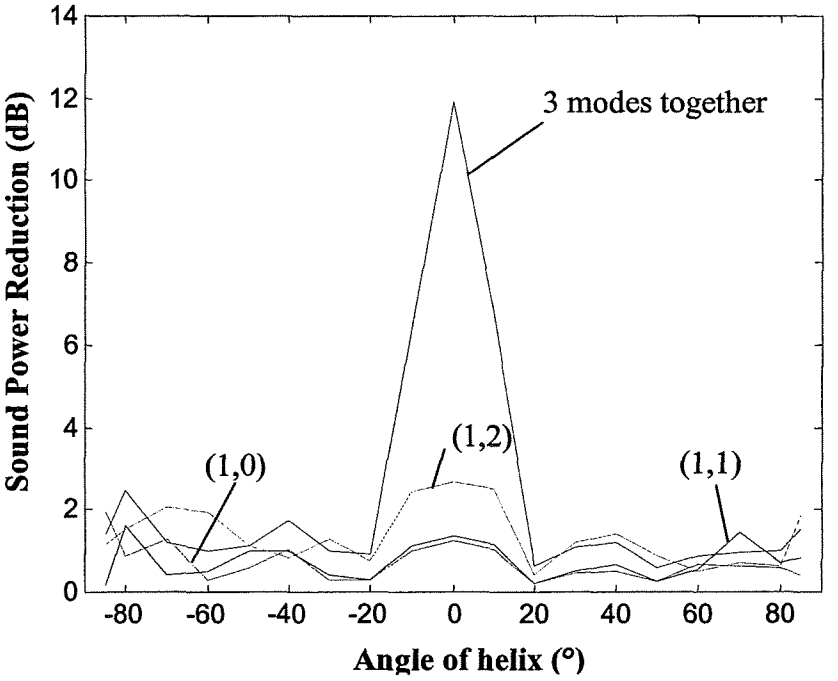

Figure 3.31: Effect of the helix angle on the sound power reduction for 4 helixes of 5 tubes in configuration 1.

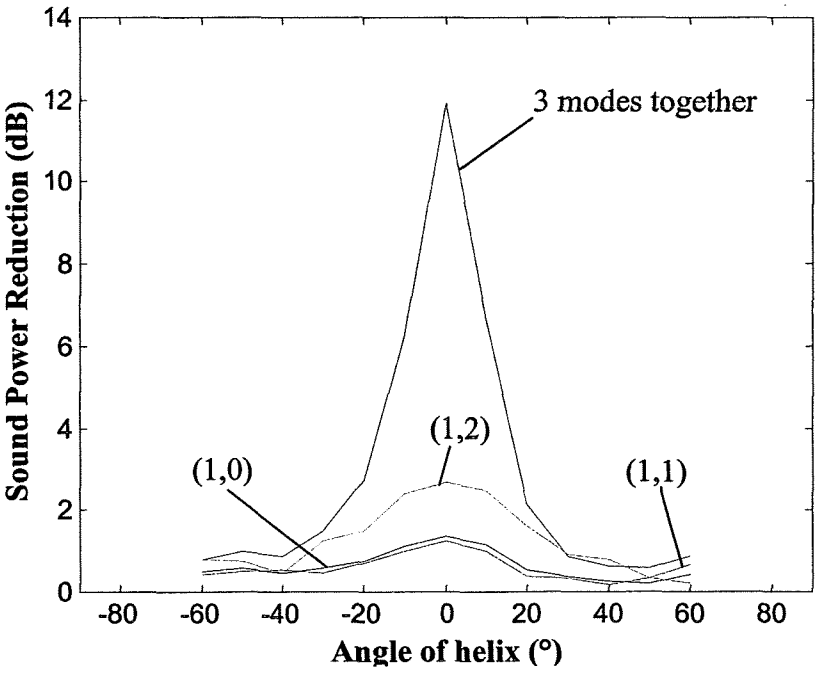

Figure 3.32: Effect of the helix angle on the sound power reduction for 4 helixes of 5 tubes in configuration 2.

Once again, placing the tubes in 4 helix arrays does not achieve any improvement in the sound reduction. The best sound power reduction is obtained with a circumferential

array of tubes whether the modes (1,0), (1,1) or (1,2) are propagating individually or simultaneously through the engine inlet. By looking at the configuration of the system, one can easily understand why the helix concept does not work here. Placing the tubes in 4 helixes of 5 tubes is the same as having 5 successive circumferential arrays of 4 tubes placed at a different angle relative to the top of the inlet duct. Therefore, the scattering effect will cause the incident energy from modes (1,0), (1,1) and (1,2) to be scattered into other circumferential modes that are cut-on. That is, from the scattering equation ($m_{HQ}=m_D\pm kN_T$), energy will be radiated through modes of circumferential orders –7, -3, +5 and +9. Therefore, in order for the HQ system placed in helix patterns to be efficient, the number of helixes must be high enough, such that no energy is scattered into other circumferential propagating modes. This case is presented in the next study where the case of 11 helixes of 2 tubes is investigated. The HQ tubes are now placed such that they form 11 helixes along the engine inlet, each helix being made of 2 tubes. The reference system is then a circumferential array of 22 tubes. Once again, configurations 1 and 2 will be investigated here. Figure 3.33 first shows the effect of helix angle on the sound power reduction for helixes in configuration 1.

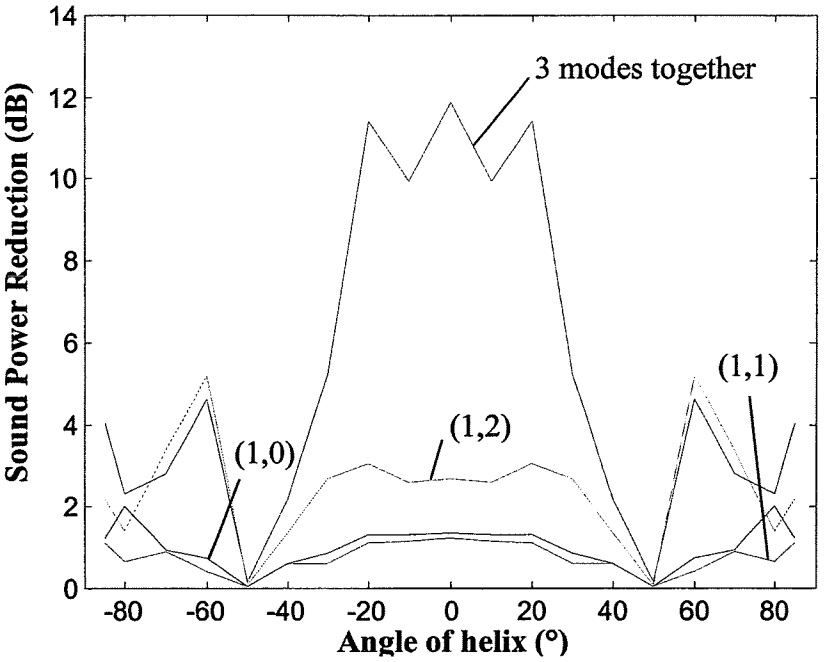

Figure 3.33: Effect of the helix angle on the sound power reduction for 11 helixes of 2 tubes in configuration 1.

It is clear in Figure 3.33 that a better sound reduction is achieved when the angle of the helixes is small. When the 3 modes are in the disturbance, reduction of more than 10 dB is indeed observed with helixes at an angle less than 20°. Figure 3.33 also shows a critical angle, 50°, where the reduction dramatically drops. For higher angles, the reduction increases but remains under 5 dB. Placing the tubes such that the helix angle is 60° seems to reduce the noise propagating through mode (1,2). The sound reduction for this mode is 5.2 dB at this angle, whereas it was only 2.7 dB with a circumferential array.

However, it does not seem to be a relation between the angle of propagation of modes and the angle of the helix. The sound power reduction at angles higher than 80° is indeed much smaller than in the case of a circumferential array. The case of 11 helixes of 2 tubes placed as in configuration 2 is shown in Figure 3.34 for helix angles ranging from – 60° to 60°. As shown in Figure 3.34, the HQ system provides good reduction for helix angles smaller than 20°. However, the sound power reduction decreases as the helix angle increases.

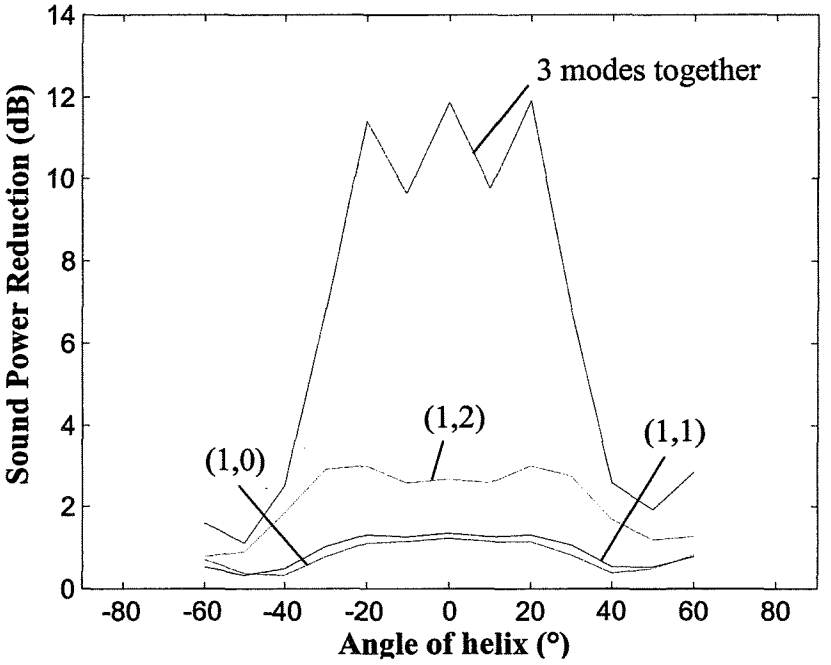

Figure 3.34: Effect of the helix angle on the sound power reduction for 11 helixes of 2 tubes in configuration 2.

The previous results do not really show any correlation between the angle of the tube helixes and the angle of propagation of the incident modes. The best reduction is still achieved with a circumferential array of tubes and there is no real improvement of the HQ system efficiency by placing the tubes in helix patterns. However, in the previous study, the three incident modes (1,0), (1,1) and (1,2) had an angle of propagation higher than 80° at 2320 Hz. In order to know if the helix array concept would be more efficient at lower propagation angles, the frequency of analysis will now be chosen just after a mode is cut-on. The case of mode (1,1) will be illustrated here. This mode is cut-on at 1084 Hz. Table 3-5 shows the angle of propagation of this mode for frequencies just above 1084 Hz. As seen in Table 3-5, at frequencies just above cut-on, mode (1,1) is propagating in the helix at smaller angles. As the frequency increases, the angle of propagation also increases. To further investigate this, the tubes were placed to form 10 helixes of 2 tubes and the effect of the helix angle on the sound reduction was investigated at frequencies just after cut-off. For this study, the HQ tube system was optimized in order to provide maximum reduction with a circumferential array of 20

tubes at 1085 Hz. Thus, the tubes had a centerline length of 14.2 cm and the distance between tube ends was 12.0 cm. Figure 3.35 first shows the sound power reduction as a function of helix angle and frequency in the case of configuration 1.

Table 3-5: Angle of propagation of mode (1,1) at frequencies just after cut-off.

Frequency (Hz)	Angle of propagation (°)
1085	40.4
1089	49.1
1093	53.2
1097	55.9
1101	58.1
1105	59.7

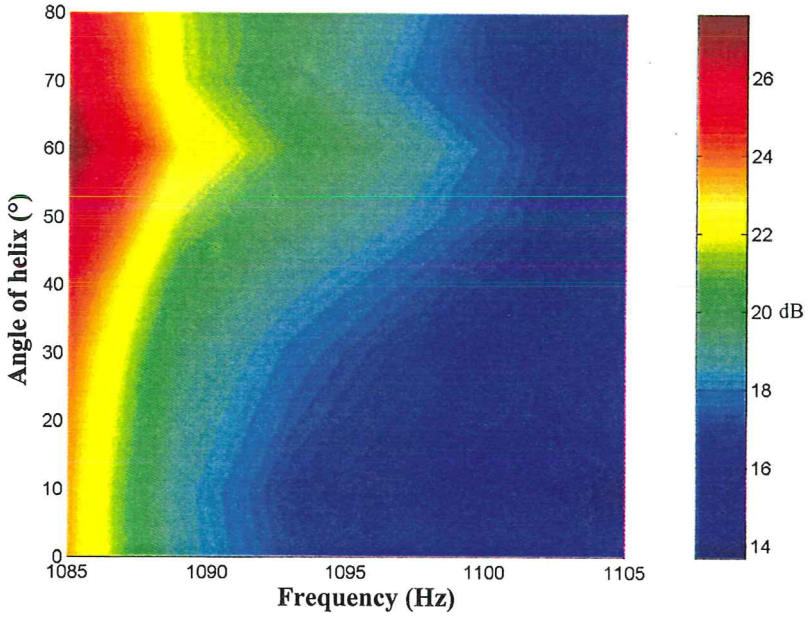

Figure 3.35: Effect of the helix angle for incident mode (1,1) at frequencies just above cut-on – configuration 1.

As seen in Figure 3.35, placing the HQ tubes in a helix with angle ~60° clearly allows an increase the sound power reduction at frequencies just above the cut-off frequency. Moreover, the improvement achieved by the helical array drops out as the frequency increases. At 1105 Hz, which is only 20 Hz above cut-off frequency, the improvement achieved by the HQ system placed in a helix array is indeed quite insignificant.

Figure 3.36 shows the same study applied to configuration 2. The range for the helix angles is now –60 to 60°. Again, placing the HQ tubes in helix patterns provides an increase in the sound power reduction. At 60°, the sound reduction is 25 dB whereas a circumferential array provided 23.5 dB reduction in the sound power at 1085 Hz. The results seem to be identical for positive or negative angles of the helix. However, once again, the sound power reduction very rapidly decreases as the frequency increases. The improvement in the efficiency of the system in helix pattern is only visible at frequencies very close to the cut-off frequency. Therefore, there is no direct relation between the angle of maximum reduction and the angle at which the incident mode is propagating in the inlet.

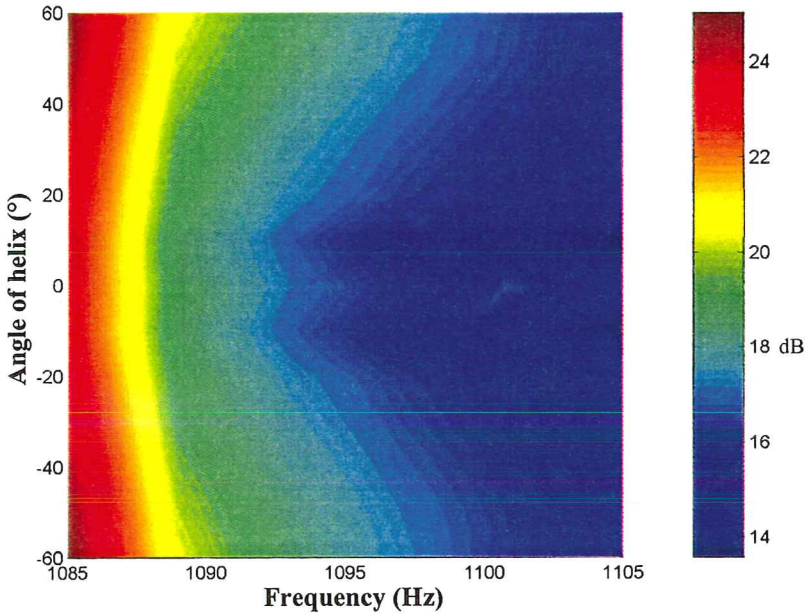

Figure 3.36: Effect of the helix angle for incident mode (1,1) at frequencies just above cut-on – configuration 2.

This study investigated a new configuration for the HQ system based on placing the HQ tubes in helixes. As the modes are propagating in the inlet along helixes, it is possible that the new helix configurations could improve the noise reduction. Although the system with arrays in helix patterns allowed for an increase in the sound reduction of a mode just cut-on, the amelioration in the results was only noticeable on a very short frequency range.

3.6.3 Circumferential array with tubes at an angle with respect to the engine axis

Based on the previous idea that modes are propagating in the inlet along the helix, another configuration was investigated. The HQ tubes were placed in a circumferential array and were rotated such that they formed an angle with respect to the inlet axis.

Unlike the previous configurations where the tubes were placed in helix patterns, this system is very practical and could be easily built. This system is illustrated in Figure 3.37.

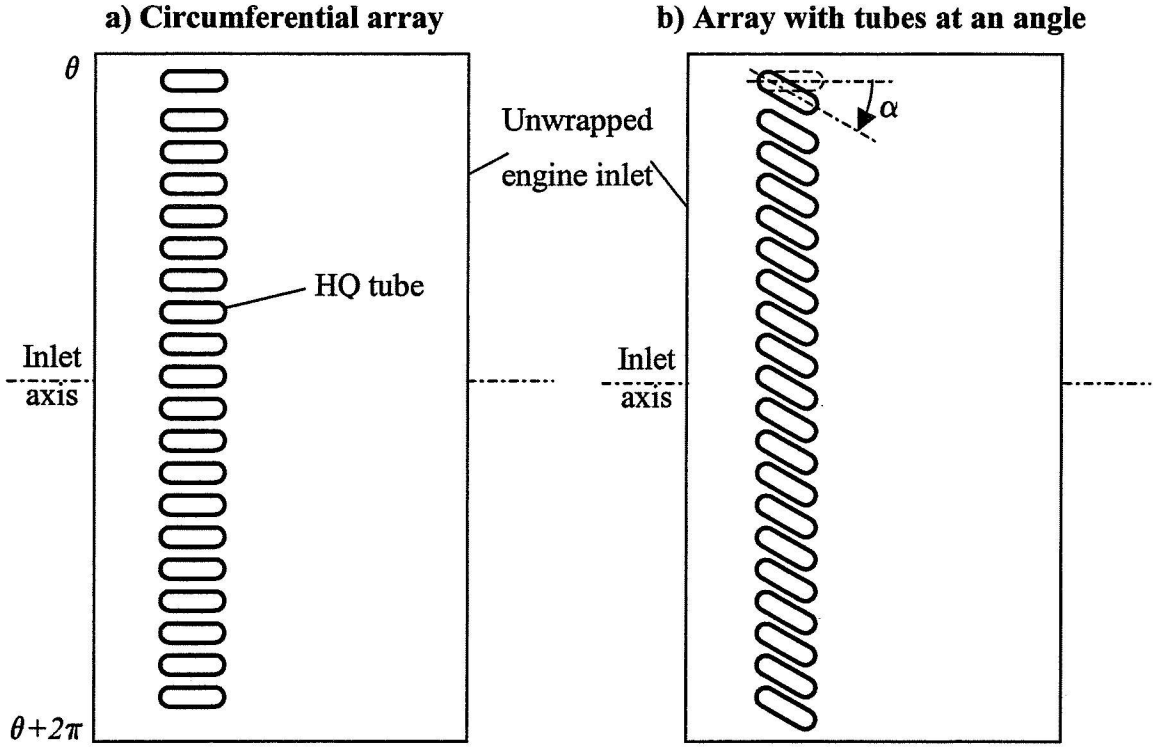

Figure 3.37: Expanded view of the inlet with HQ tubes placed a) in a circumferential array or b) in an array with tubes at an angle with respect to inlet axis.

The angle α is measured from the inlet axis and the positive direction for this angle is chosen to be the same as the direction of rotation of the fan. As in the previous study, the results will be presented for three incident modes of order (1,0), (1,1) and (1,2). The dimensions of the inlet are those of the JT15D engine. The reference HQ tube system consists of a circumferential array of 20 tubes with centerline length 11.8 cm.

The sound power reduction provided by the system as a function of the BPF is shown in Figure 3.38. In this case, the three incident modes (1,0), (1,1) and (1,2) are propagating simultaneously in the inlet. The tube angles range from –65° to 65°, which is the maximum possible range. Figure 3.38 clearly shows that placing the tubes at an angle from 20° to 45° provides a significant increase in sound power reduction as compared to having the tubes parallel to the engine axis (α =0°). Both positive and negative tube angles result in better performance in this range. As the angle of the tubes increases from 0° to -40°, the maximum sound power reduction over the frequency range increases from 12.3 to 14.5 dB. It is obvious that the plot will flip if the modes are spinning in the opposite direction. Although the system with tubes at an angle allows to improve the

sound reduction, the optimum angle does not correspond to the angle of propagation of the three incident modes (1,0), (1,1) and (1,2).

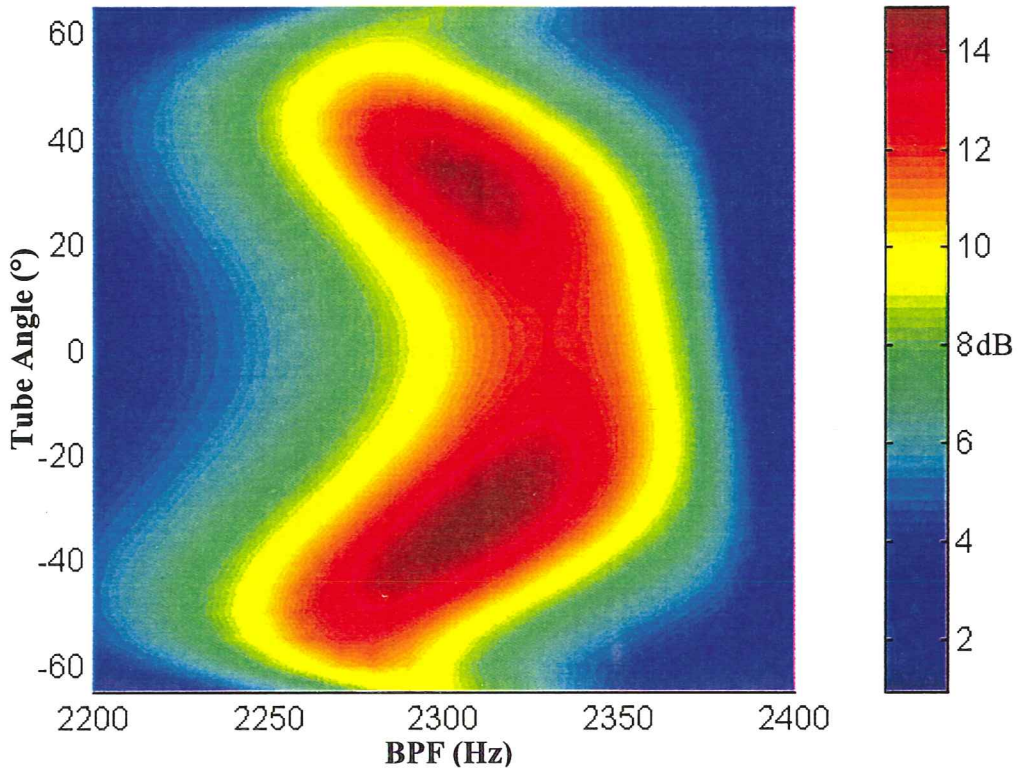

Figure 3.38: Effect of tube angle on sound power reduction for 3 incident modes propagating in inlet of the JT15D engine.

As the angle of the tubes changes up to ±40°, the reduction provided by the tubes increases; however at the same time, the frequency of optimum reduction is shifted down from 2330 to 2300 Hz. To account for this frequency change, the geometry of the tubes needs to be adjusted as the tube angle changes to provide optimum sound reduction at a given frequency. The centerline tube length was previously shown to be the dominant criterion to set the frequency of resonance of the system, therefore this parameter will be adjusted here as an example to provide reduction at 2330 Hz. Figure 3.39 shows the sound power reduction as a function of BPF for an optimum reduction at 2330 Hz with straight tubes and tubes at an optimum angle. In Figure 3.39, the blue curve corresponds to an array of tubes parallel to the inlet axis (α=0°) and of centerline length 11.8 cm. The reduction at 2330 Hz is then 12.3 dB. On the other hand, the red curve corresponds to an array with tubes at an angle of –40°. The centerline tube length was optimized to provide maximum reduction at 2330 Hz and is thus 11.6 cm. Now, the reduction at 2330 Hz is 15.6 dB, so 2.3 dB higher than in the previous case.

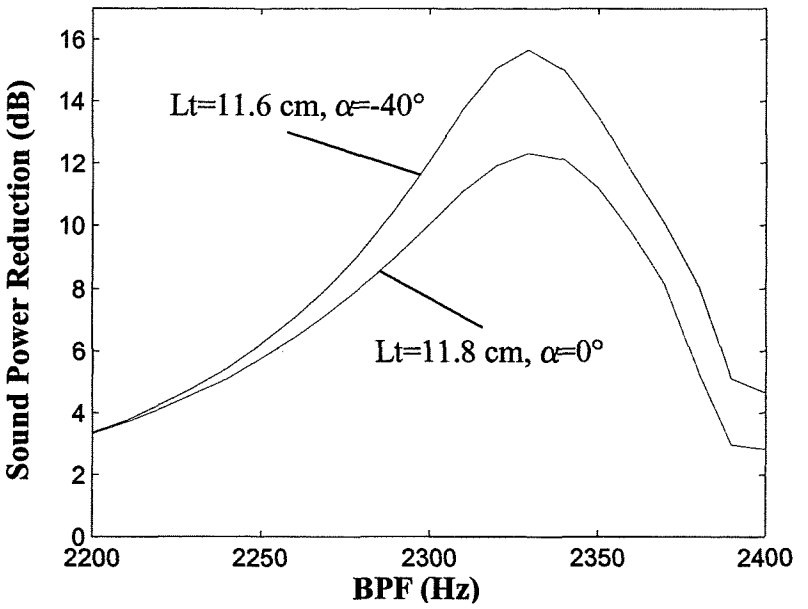

Figure 3.39: Sound power reduction for an array of straight tubes and an array of tubes placed at an angle relative to the inlet axis – 3 modes propagating in the inlet of the JT15D engine.

The previous results showed that placing the tubes at an angle allowed to improve the performance of the system. The transmitted mode amplitudes were looked at and compared in the case of an array of straight tubes and for an array with tubes at the optimum angle of –40°. The values of the modal amplitudes will not be shown here to avoid getting into too much complexity and keep the exposition clear. However, it can be concluded from these results that two noise control mechanisms are involved here. First, the system with tubes at an angle seems to increase the reflection of the incident energy from each individual incident mode as compared to the case with straight tubes. On the other hand, the scattered energy from each incident mode into the two other radial modes tends to be more important when the tubes are placed at an angle. As there is more energy scattered between the three propagating modes, the recombination mechanism and suppression of energy in each mode is more efficient and thus the transmitted acoustic energy tends to be lower.

As seen in the previous results, the system tends to be more efficient when tubes are rotated at a certain angle, regardless if this angle is positive or negative. Therefore, this system could eventually be used in a case where the disturbance includes modes, which are spinning in the positive as well as in the negative direction. Therefore, the same study was performed based on the Honeywell engine. At the BPF of this engine there are incident modes rotating in the positive direction ($m=2$ and $m=12$) as well as in the negative direction ($m=-8$). The effect of the tube angle is shown in Figure 3.40. The reference HQ system is a circumferential array of 27 tubes optimized to provide reduction at 2150 Hz. The centerline tube length is then 12.7 cm. As the number of tubes along the circumference is high and the distance between tube ends will be small for high tube angles, the near-field effect will have a stronger effect. Therefore, the number of

modes included in the Green's function for these simulations is 40 circumferentials and 40 radials.

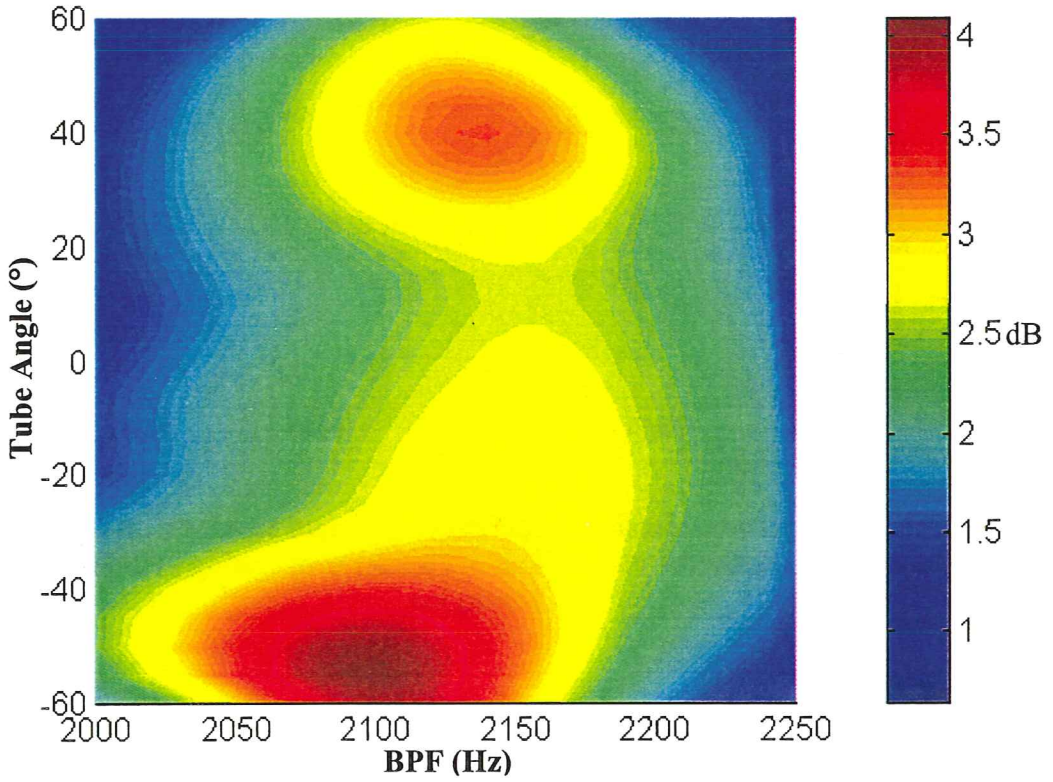

Figure 3.40: Effect of tube angle on sound power reduction for positive and negative rotating modes propagating in the inlet of the Honeywell engine.

As seen in Figure 3.40, a significant improvement in the performance of the system is provided with tubes at an angle of –55°. The maximum reduction at this angle is 4.1 dB whereas maximum reduction achieved with the circumferential array is 2.7 dB. However, as observed previously, the frequency of maximum reduction is shifted down as the angle of the tubes increases. The centerline of the tubes was next optimized to provide maximum reduction at 2150 Hz with tubes at an angle of –55°. The results in this case are shown in Figure 3.41. The blue curve corresponds to an array of tubes parallel to the inlet axis (α =0°) and of centerline length 12.7 cm. The reduction at 2150 Hz is then 2.7 dB. On the other hand, the red curve corresponds to an array with tubes at an angle of –55°. The centerline tube length was optimized to provide maximum reduction at 2150 Hz and is 12.3 cm. Now, the reduction at 2150 Hz is 3.7 dB, so 1.0 dB higher than in the previous case.

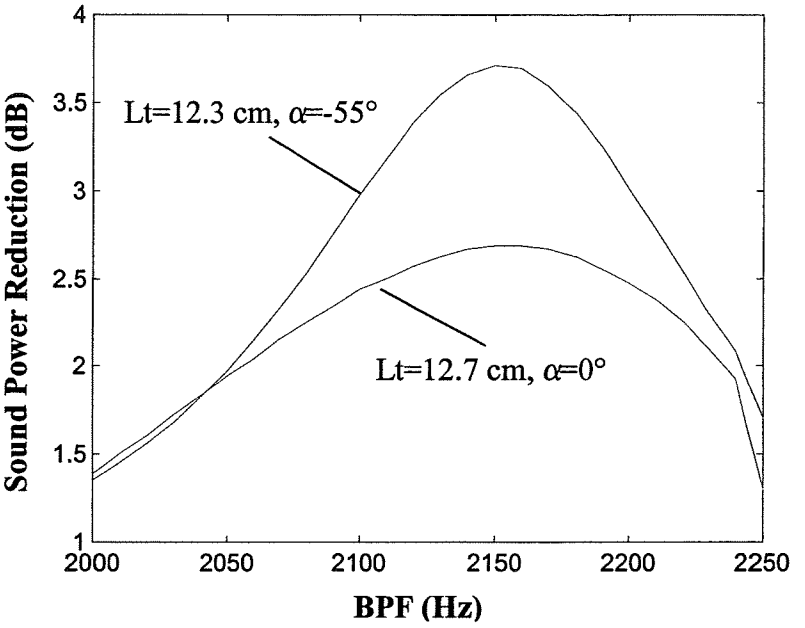

Figure 3.41: Effect of tube angle on sound power reduction for positive and negative rotating modes propagating in the inlet of the Honeywell engine.

3.6.4 Array in a helix pattern with tubes rotated at the same angle

The two previous sections investigated configurations of the HQ tubes based on the helical propagation of modes. The first system consisted of placing the HQ tubes in helix patters and the second of rotating the tubes placed in a circumferential array. Both systems will now be combined in a system where the arrays of tubes are placed at an angle with tubes rotated at the same angle as the helix. The tubes will be placed along the inlet as illustrated in Figure 3.42. In this study, the system was optimized to provide maximum reduction at 2320 Hz in the reference configuration when the incident modes (1,0), (1,1) and (1,2) are propagating in the inlet. The reference system consists of 2 arrays of 11 tubes located at 0.25 and 0.45 m from the fan respectively. The tubes have a centerline length of 11.8 cm and the distance between ends is 9.2 cm. The sound power reduction is shown in Figure 3.43 where the helix angle α as defined in Figure 3.42, and ranges from –60° to 60°. As seen in Figure 3.43, improvement in the sound reduction is achieved with a helix at ±40°. As the helix angle increases from 0° to 60°, the frequency of maximum reduction is shifted down from 2320 to 2250 Hz. This mechanism was already observed when only the tubes were rotated at an angle with respect to the inlet axis. Placing the tubes in a helix with the tubes rotated at the same angle seems to improve the performance of the HQ system. However, the maximum reduction provided by this system is 14 dB, which is not significantly higher than the reduction provided by a circumferential array with 20 tubes. Moreover this system is rather complex and would be very complicated to build. Once again, no relation is shown between the optimum angle of reduction and the angle of propagation of the three incident modes (4.6° for mode (1,0), 5.0° for mode (1,1) and 6.4° for mode (1,2) at 2320 Hz).

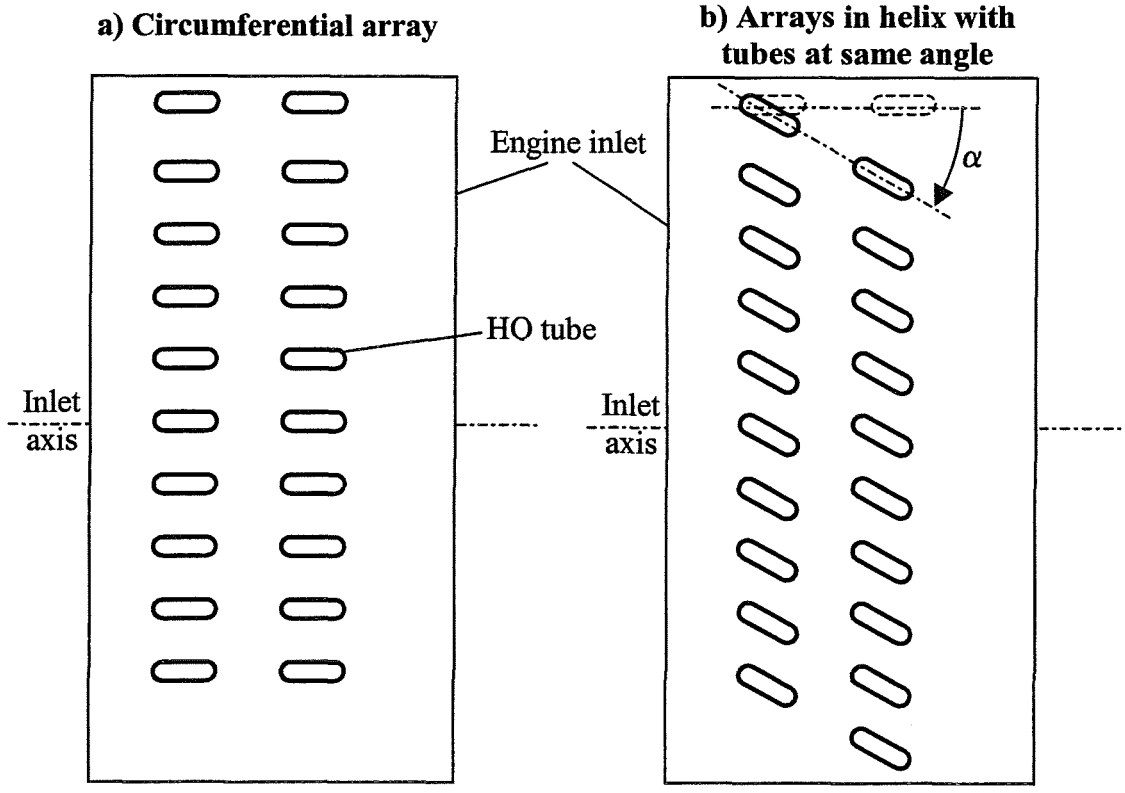

Figure 3.42: Expanded view of the inlet with HQ tubes placed a) in a circumferential array or b) in helixes patterns with tubes at an angle.

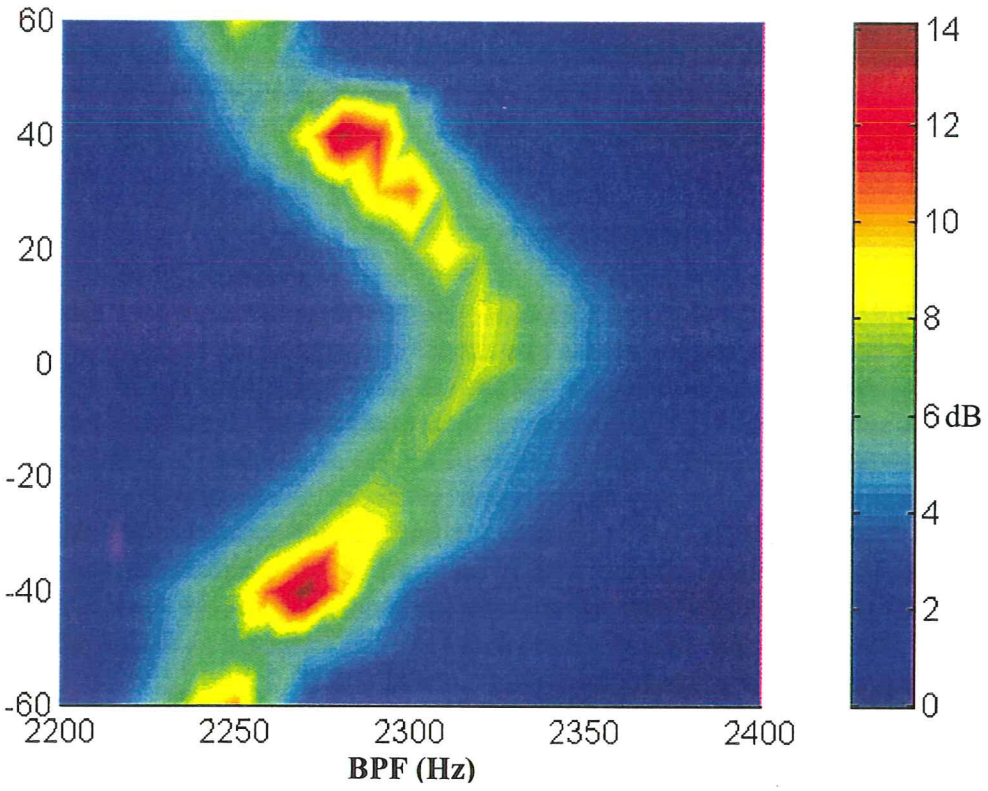

Figure 3.43: Effect of helix angle on the sound power reduction for 11 helixes of 2 tubes at the same angle as the helix.

4. ANALYTICAL MODELING-BOUNDARY INTEGRAL METHOD

This section presents the modeling of the HQ concept based on the modification of the NASA developed TBIEM3D code [2] . A brief description of the TBIEM3D code is presented before the HQ modeling approach is described. The modified code to model the HQ tubes is referred to as HQTBIEM3D.

4.1. DESCRIPTION OF TBIEM CODE

The Boundary Integral Equation Method (BIEM) was developed by Dunn et.al [3] for predicting ducted fan engine noise. The model consists of an engine fan surrounded by an infinitesimally thin, finite length cylindrical duct translating in the axial direction with uniform speed. The BIEM is based on the equations of liberalized acoustics with uniform inflow and predicts the sound scattered by the duct when it is irradiated by the incident sound generated by the fan or other sources. A schematic of the model is presented in Figure 4.1. The duct is assumed to have a hard wall exterior and a lined or hard wall interior. The liner interior wall is assumed to have circumferentially uniform impedance. It can be axially segmented, and positioned anywhere inside the duct. A collection of circumferential evenly spaced point sources, situated in a disc perpendicular to the duct axis, is used to generate the incident sound field.

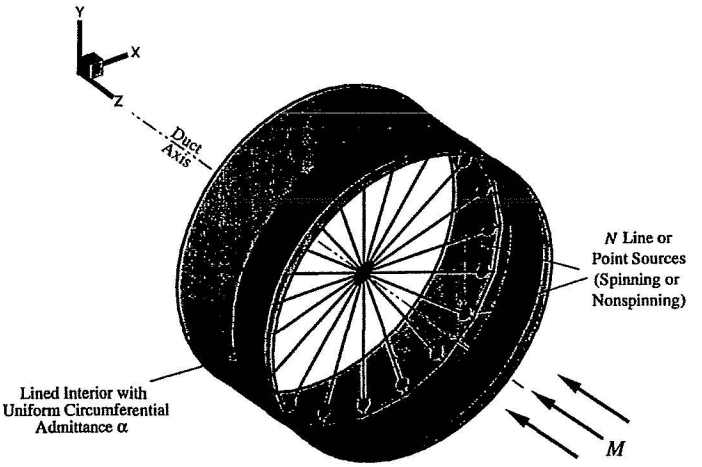

Figure 4.1: BIEM duct geometry (from Dunn [2]). Source plane located at z=0.

The BIEM technique was used to develop the computer code TBIEM3D (Thin duct Boundary Intergal Equation Method, 3 Dimensional) for the prediction of ducted fan noise [2]. This code was later modified by Hutchinson [8] to simulate active noise control of the fan noise. Hutchinson developed and implemented a subroutine for simulation of active noise sources. The control sources were modeled as simple sources on the duct wall.

In this research work, the TBIEM3D code was further modified to model the effect of the HQ-tubes on the noise reduction of the fan noise. The modifications to this code are described in the next section.

4.2. MODELING TECHNIQUE

The modeling approach for the effect of the HQ-tubes on the duct is the same as in the infinite duct model presented in section 3.1. Thus, the modeling of HQ requires the computation the average pressure over a finite source on the duct wall due to another source with unit velocity, i.e. auto and cross impedances. In addition, it is needed to compute the average pressure over the piston sources due to the disturbance fan source. The computation of these parameters using the TBIEM3D code is described in the next sections.

4.2.1 Auto and Cross Source Impedance

The key step in the modeling is to find an expression for the acoustic pressure due to a finite source positioned at $\vec{r}_S = (z_S, r_S, \theta_S)$ and with radial velocity $\vec{V}_S$ as shown in Figure 4.2. The dimensions of the source are defined by b and α.

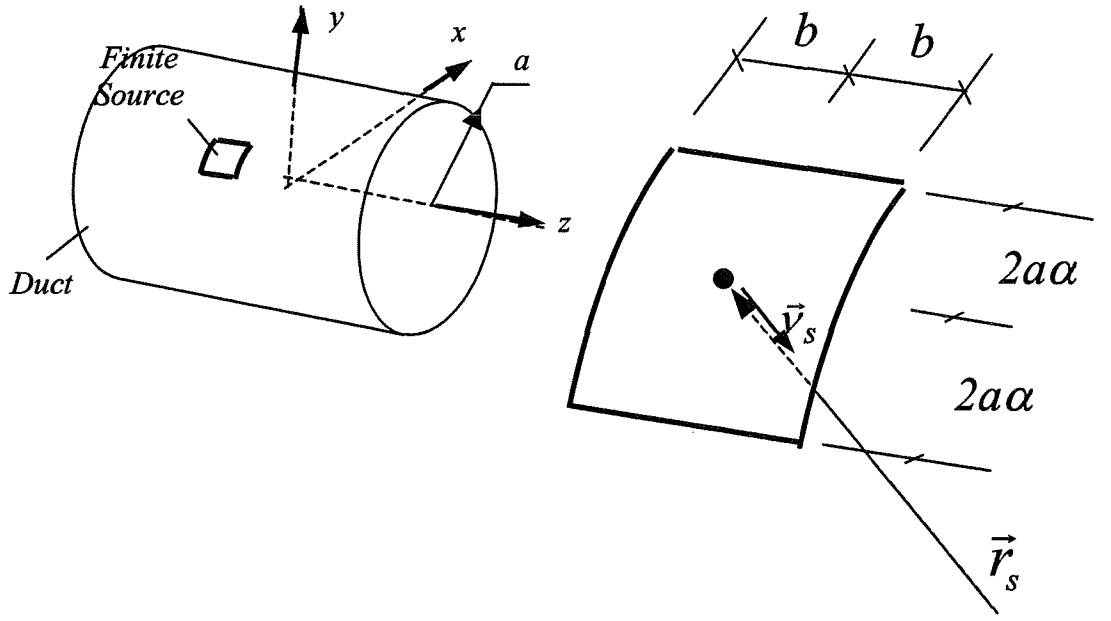

Figure 4.2: Piston source radiating into the finite length duct.

Once again this can be obtained by integrating the Green's function over the surface of the piston that represent the tube-duct interface. That is

$$p(\vec{r}\,|\,\vec{r}_s) = ik_o \rho c v_s \int_{z_s-b}^{z_s+b} \int_{\theta_s-\alpha}^{\theta_s+\alpha} g(\vec{r}\,|\,\vec{r}_\ell)\, dz_\ell\, a\, d\theta_\ell \tag{4.1}$$

where $g(\vec{r}\,|\,\vec{r}_\ell)$ is the Green's function that relates the pressure at $\vec{r}_\ell$ due to the point source located at $\vec{r}$ depicted in figure 4.3.

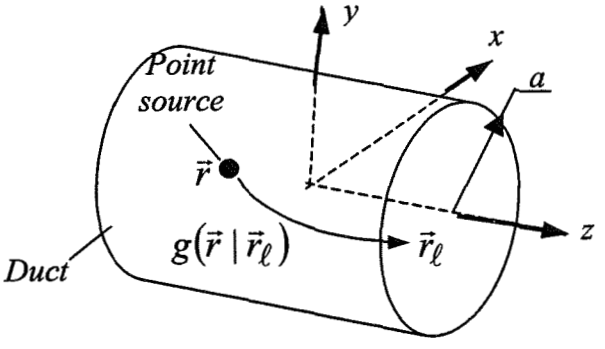

Figure 4.3: Green's function $g(\vec{r}\,|\,\vec{r}_\ell)$.

Due to the symmetry of the sound field with respect to the plane defined by the duct axis and the point source, the Green's function can be expanded in terms of the circumferential modes as follows

$$g(\vec{r}\,|\,\vec{r}_\ell) = \sum_{m=0}^{\infty} g_m(z, r\,|\,z_\ell r_\ell) \cos\left[m(\theta - \theta_\ell)\right] \tag{4.2}$$

where now the function $g_m(z, r\,|\,z_\ell, r_\ell)$ represents the radial pressure distribution of the Green's function due to the m^{th} order circumferential mode. This function is computed by the HQTBIEM based on the subroutine developed by Hutchinsong [8].

Replacing (4.2) into (4.1) and assuming the point source is at the duct wall, i.e. $r=a$, yields

$$p(\vec{r}\,|\,\vec{r}_s) = ik_o \rho c v_s \sum_{m=0}^{\infty} \int_{z_s-b}^{z_s+b} g_m(z, r\,|\,z_\ell, a)\, dz_\ell \int_{\theta_s-\alpha}^{\theta_s+\alpha} \cos\left[m(\theta - \theta_\ell)\right] a\, d\theta_\ell \tag{4.3}$$

The second integral can be easily solved in closed form to give

$$\int_{\theta_s-\alpha}^{\theta_s+\alpha} \cos\left[m(\theta-\theta_\ell)\right] a d\theta_\ell = 2a\alpha \frac{\sin(m\alpha)}{m\alpha} \cos\left[m(\theta-\theta_s)\right] \tag{4.4}$$

On the other hand, the first integral needs to be solved numerically. The physical interpretation of this integral is that it represents the integration of a line source of length *2b*. Here, this integral is solved by assuming the line source is replaced by *N* evenly distributed point sources as illustrated in Figure 4.4. That is

$$\int_{z_s-b}^{z_s+b} g_m(z,r\,|\,z_\ell,a)dz_\ell \approx \sum_{n=1}^{N} g_m(z,r\,|\,z_{\ell n},a)\Delta z \tag{4.5}$$

where $z_{\ell n}$ is the axial coordinate of the n^{th} (n=1,2,...N) point source and $\Delta z = 2b/N$ is shown in Figure 4.4. Note that $z_{\ell n}$ is a function of the source center position z_s.

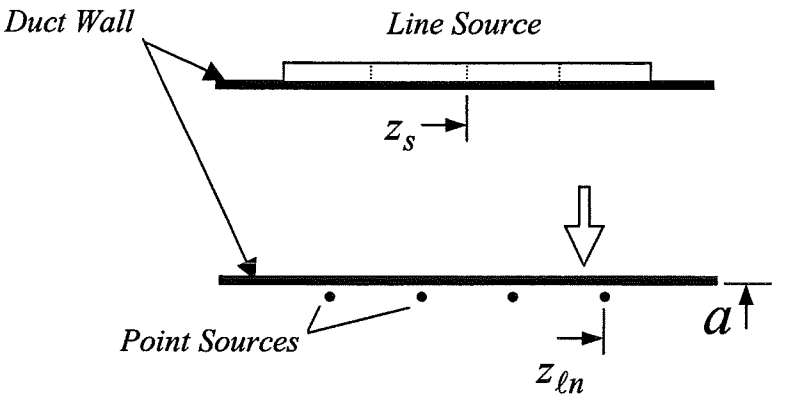

Figure 4.4: Approximation of a line source by a finite number *N* of point sources.

Thus, the pressure at an arbitrary point $\vec{r}$ in the acoustic field due to a source at $\vec{r}_S = (z_S, a, \theta_S)$ is

$$p(\vec{r}\,|\,\vec{r}_s) \approx ik_o\rho c v_s \sum_{m=0}^{\infty} \left\{ \left(\sum_{n=1}^{N} g_m\left(z,r\,|\,z_{\ell n},a\right)\frac{2b}{N} \right) \frac{2a\alpha \sin m\alpha}{m\alpha} \cos m(\theta-\theta_s) \right\} \tag{4.6}$$

In the modeling of the HQ-tubes, it is required to compute the auto and cross impedances between the piston sources representing the tube-duct interfaces. This is illustrated in Figure 4.5 for the case of two arbitrary piston sources. The average pressure at the o^{th} "observation" source due to the s^{th} piston source is obtained by integrating (4.6) over the surface of the o^{th} piston source

$$\overline{p}(\vec{r}_o \mid \vec{r}_s) = \frac{1}{(2b')(2a\alpha')} \int_{z_o-b'}^{z_o+b'} \int_{\theta_o-\alpha'}^{\theta_o+\alpha'} p(\vec{r} \mid \vec{r}_s) dz a d\theta \tag{4.7}$$

where the dimension of the observation source is defined by b' and α' as shown in Figure 4.5.

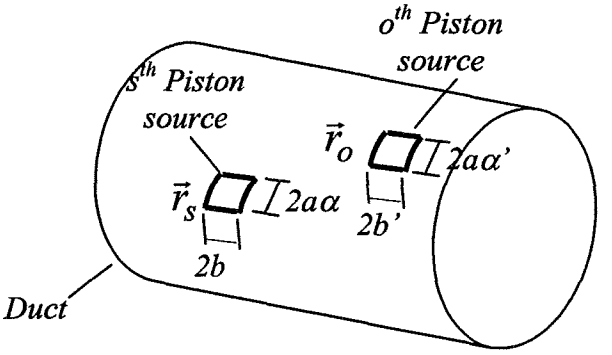

Figure 4.5: Illustration of radiating and observation pistons for computation of auto and cross impedances.

Replacing (4.6) into (4.7) gives

$$\overline{p}(\vec{r}_o \mid \vec{r}_s) = ik_o \rho c v_s \sum_{m=0}^{\infty} \left\{ \frac{1}{(2b')} \int_{z_o-b'}^{z_o+b'} \sum_{n=1}^{N} g_m(z, r \mid z_{\ell n}, a) \frac{2b}{N} dz \right. \\ \left. \frac{2a\alpha \sin m\alpha}{m\alpha} \frac{1}{(2a\alpha')} \int_{\theta_o-\alpha'}^{\theta_o+\alpha'} \cos m(\theta - \theta_s) a d\theta \right\} \tag{4.8}$$

Again the second integral is solved in closed form to yield

$$\frac{1}{2a\alpha'} \int_{\theta_o-\alpha'}^{\theta_o+\alpha'} \cos\left[m(\theta - \theta_s)\right] a d\theta = \frac{\sin(m\alpha')}{m\alpha'} \cos\left[m(\theta_s - \theta_o)\right] \tag{4.9}$$

The second integral is equivalent to computing the average pressure over a line source due to another line source as illustrated in Figure 4.6. Following the same approach as before gives

$$\frac{1}{(2b')}\int_{z_o-b'}^{z_o+b'}\sum_{n=1}^{N} g_m(z,r\,|\,z_{\ell n},a)\frac{2b}{N}dz \approx \frac{1}{(2b')}\sum_{j=1}^{(N+1)}\varepsilon_j\left(\sum_{n=1}^{N} g_m(z_{oj},a\,|\,z_{\ell n},a)\frac{2b}{N}\right)\frac{2b'}{N} \tag{4.10}$$

with

$$\varepsilon_j=\begin{cases}1/2 & for \quad j=1 \;\; and\, N+1\\ 1 & for \quad j=2,3,...,N\end{cases}$$

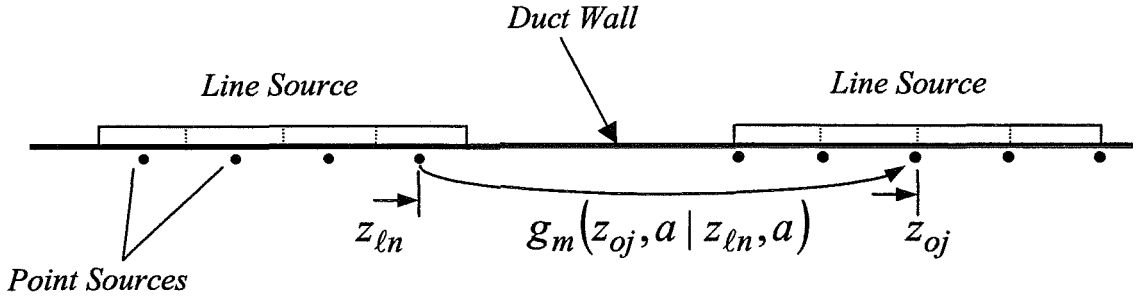

Figure 4.6: Illustration of line source and equivalent point sources, e.g. $g_m(z_{oj},a\,|\,z_{\ell n},a)$ Green's function between point sources.

The auto and cross impedance are then computed by replacing (4.9) and (4.10) into (4.8) that yields

$$\bar{p}(\vec{r}_o\,|\,\vec{r}_s)=ik_o\rho c v_s\sum_{m=0}^{\infty}\left\{\left[\frac{1}{N}\sum_{j=1}^{(N+1)}\varepsilon_j\left(\sum_{n=1}^{N} g_m(z_{oj},a\,|\,z_{\ell n},a)\frac{2b}{N}\right)\right]\left[2a\alpha\frac{\sin m\alpha}{m\alpha}\frac{\sin m\alpha'}{m\alpha'}\cos m(\theta_s-\theta_o)\right]\right\} \tag{4.11}$$

It is important to remark that the TBIEM assumes the duct to be an infinitely thin cylinder and thus there is an acoustic pressure discontinuity across the duct surface, i.e. the pressure is not uniquely defined on the duct wall. To avoid this ambiguous pressure prediction, in the previous development the pressure is computed at a small distance off the duct wall towards the interior [2].

4.2.2 Average pressure due to fan.

The principal component of tonal fan noise in a turbofan engine is the aerodynamic interaction between the fan blades and the vanes and struts downstream the duct. The fan noise in the TBIEM3D code is modeled using a collection of spinning point dipoles as illustrated in Figure (4.7). An array of dipoles is positioned along the radial direction. The axes of the dipoles are oriented parallel to the duct axis.

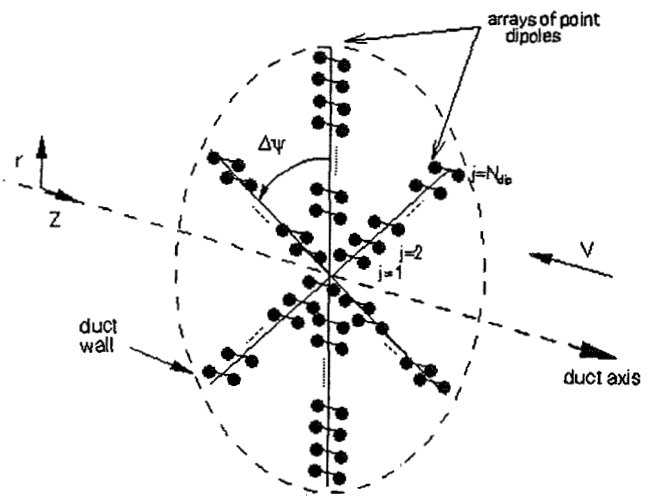

Figure 4.7: Schematic of fan noise model using radial array of spinning dipoles (taken from Hutchinson [8].

In the case where the complex amplitude of the modes propagating in the duct are known, the complex strength of the radial array of dipoles can be determine to generate these known modes. Recently, a complex line source model has been developed and implemented in the TBIEM formulation by Hutchinson [8]. In the work presented here only dipole sources are used to model the fan noise.

4.2.3 Transmitted sound power.

The output of the TBIEM code as well as of the modified code to model HQ tubes is the complex pressure at any point in the domain. Thus, to compute the performance of the HQ system, the acoustic power radiated from the duct inlet is obtained by integrating the far-field pressure radiated over the 0° to 90° sector. Though analysis of the inlet duct modes is made possibly by post-processing the pressure results computed inside the duct, it was not carried out in this research effort.

4.3. NUMERICAL RESULTS

In this section, the capability of the model for the HQ-concept using the TBIEM formulation is demonstrated by a few numerical examples. The parameters of the JT15D engine are used in these numerical simulations. The first simulation consisted of considering a single array of 20 HQ-tubes mounted on the hard wall inlet duct as shown in Figure 4.8. The length of the inlet is 0.6 m, which matched the actual inlet length in the experiments. The duct is extended towards the back of the fan 1.2 m. The tube dimensions are also the same as used in the experiments and the BPF is assumed to be 2320 Hz. Section 3.4.2 described both the engine and HQ-tube parameters.

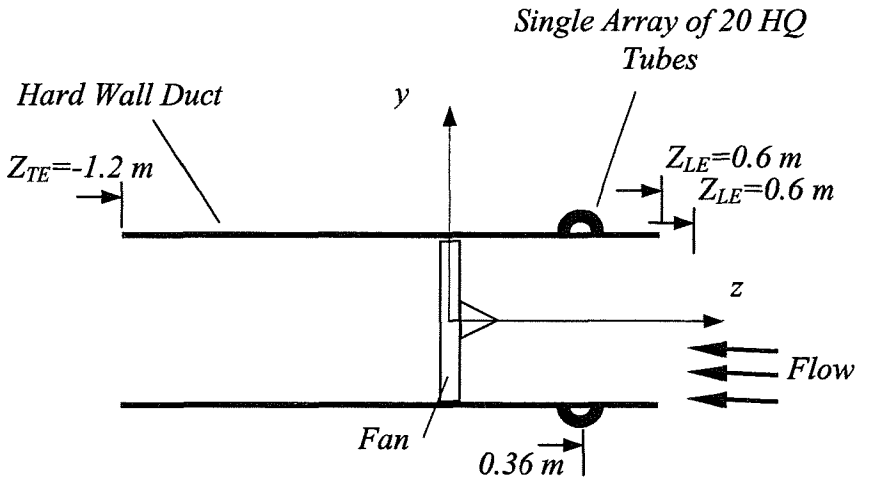

Figure 4.8: Modeling of JT15D engine inlet using TBIEM3D – Single array of 20 HQ-tubes and hard wall duct.

The radiation directivities with and without the HQ-array are presented in Figure 4.9. The results clearly show the HQ-system is effective at attenuating the sound radiation from the inlet. Integrating the far-field sound intensity over the 0° to 90° sector shows a sound power reduction of 5.1 dB. This predicted sound power reduction is similar to the experimentally measured power reduction of approximately 5.6 dB (see Figure 3.10).

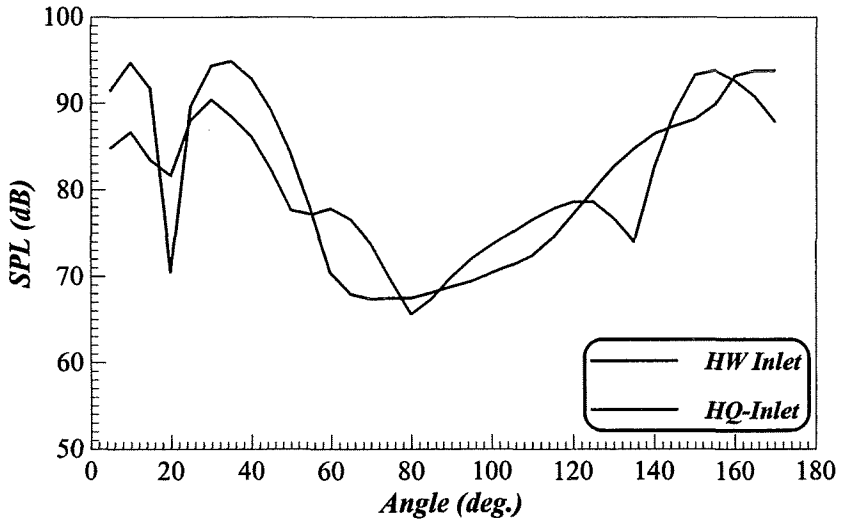

Figure 4.9: Radiation directivity of BPF tone at 2320 Hz using HQTBIEM3D. Inlet power reduction of 5.1 dB.

One of the main advantages of the HQTBIEM3D formulation is that it can easily model the effect of liners. Thus, it is important to determine the performance of the HQ-concept against that of a liner. To this end, the inlet was treated with a liner as shown in Figure 4.10. The length of the liner was selected to be 0.5 m (~83% of inlet length) and centered between the fan and the inlet opening. The liner admittance was optimized to yield the maximum inlet sound power reduction, i.e. normalized admittance of $\beta=0.2+i$ 0.4.

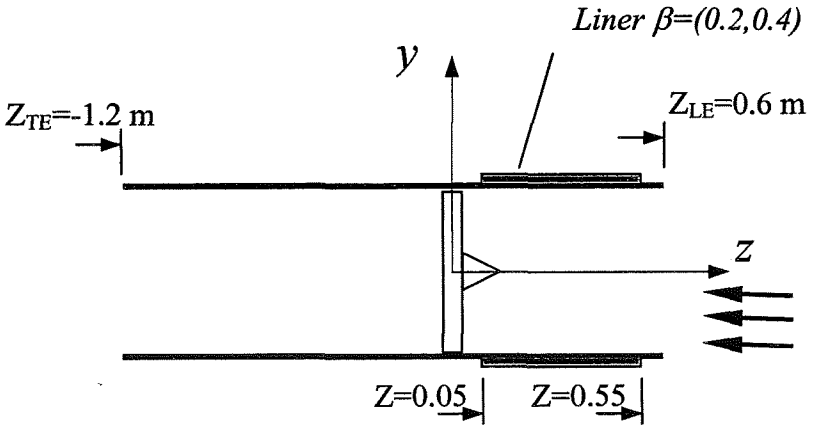

Figure 4.10: Modeling of JT15D engine inlet using TBIEM3D – Optimum liner on the inlet.

The radiation directivities for the hard wall and lined inlets are shown in Figure 4.11. The results again show good attenuation of the inlet radiated noise at the BPF of

2320 Hz. The sound power reduction over the 0° to 90° sector obtained by the liner was 6.4 dB, which shows better attenuation than the 5 dB achieved with the HQ-system. However, the liner attenuation was obtained at the expense of using virtually all the surface area of the inlet duct (83 %). This should be contrasted to the small surface area taken by the HQ-system (~ 4% of inlet area) in Figure 4.8. It is important to mention that the HQ-system is mainly a reactive device that reflects energy back towards the engine fan. This is clear in Figure 4.9, which shows noise level increasing at some angles in the aft sector. On the other hand, the liner is absorbing the acoustic energy as it propagates upstream towards the inlet opening. The implication is that minimum reflection towards the aft probably takes place as shown in the results of Figure 4.11. Thus, the integration of the HQ-tube with a liner has the potential of efficiently incorporating the strength of both systems. This HQ-liner concept is investigated next.

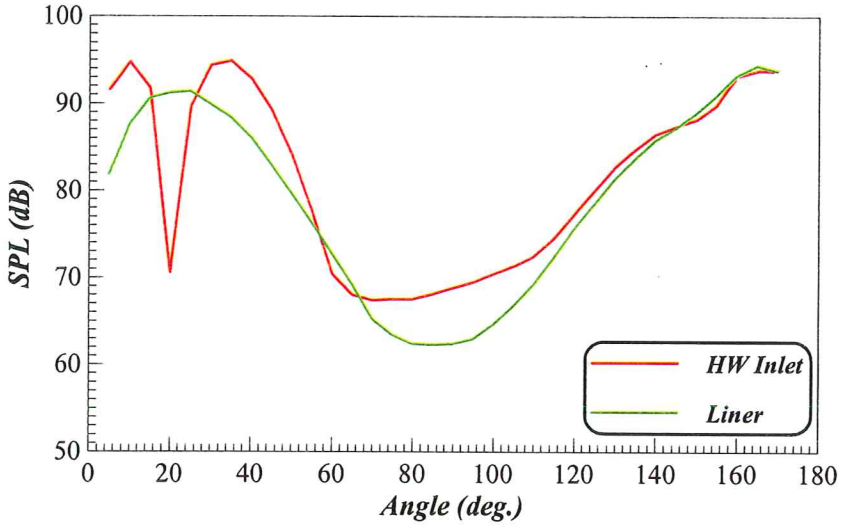

Figure 4.11: Radiation directivity of BPF tone at 2320 Hz using HQTBIEM3D. Inlet power reduction of 6.4 dB due to liner.

To investigate the performance of integrating a HQ-system with a liner, the system shown in Figure 4.12 was considered. The system consisted of integrating a single array of 20 HQ tubes with a liner. The parameters of the HQ-tubes and axial location are the same as used in the simulation of Figure 4.8. The liner was assumed to have the same dimensions and location as used in the simulations of Figure 4.10. However, the liner admittance was optimized to minimize the power radiated over the 0° to 90° sector. In the simulation, it also was assumed that the implementation of the HQ-system did not reduced the effective liner surface area. This assumption seems to be reasonable since the HQ-array takes only 4% of the inlet area. This is small compared to the 83% used by the liner. However, the area taken away from the liner (and thus the potential degradation on the liner performance) by multiple arrays of HQ-tubes integrated with a liner should be considered.

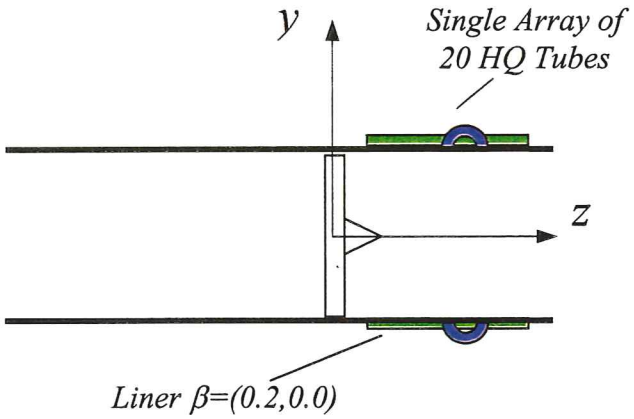

Figure 4.12: Modeling of JT15D engine inlet using TBIEM3D – Optimum liner on the inlet.

The radiation directivities for the hard wall, liner, and HQ-liner systems are shown in Figure 4.13. It is clear that the HQ-liner is more effective at controlling the inlet noise as compared to both the liner and HQ-array. The sound power attenuation achieved by the liner was 4.6 dB as compared to the 6.4 dB obtained by the optimum liner in Figure 4.11. However, the combined HQ-liner system resulted in a 7.2 dB power reduction on the forward sector. It is important to remark that better reduction could be achieved by optimizing the HQ-tube parameters and the liner properties, simultaneously.

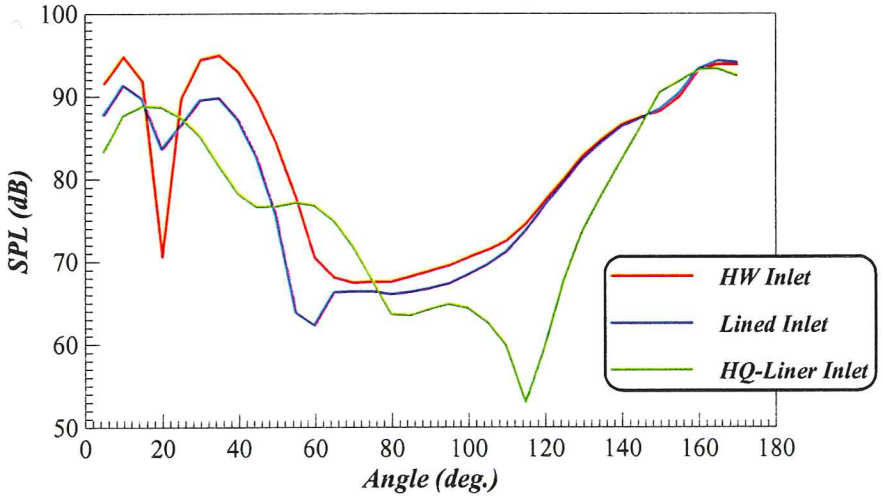

Figure 4.13: Radiation directivity of BPF tone at 2320 Hz using HQTBIEM3D. Inlet power reduction of 7.2 dB due to HQ-tubes and liner.

5. CONCLUSIONS

In this report, two analytical tools were developed to model HQ-waveguides implemented on the inlet of turbofan engines. The first model is based on assuming the inlet to be part of an infinite cylindrical rigid duct. The sound field is expanded in terms of the acoustic modes. The second modeling tool consists of modifying the code TBIEM3D developed at NASA [2] to account for the effect of HQ-arrays. This model has the advantage of considering a finite length duct with the sound field inside and outside the duct to be fully coupled. In addition, the effect of a lined duct is easily incorporated in the analysis. Both of these modeling tools allow for the modeling of HQ-tubes in arbitrary configurations. They are not restricted to circumferential arrays of HQ-tubes.

The infinite duct based model was extensively used in this research. The results provided by the model were compared to experimental data taken on two real engine inlets on which the HQ system was applied. Both tonal and broadband results showed good agreement between the predictions and the experimental results and therefore allowed validating the modeling technique. In particular, the model allows predicting very accurately the frequency of attenuation of the system. It was also found that a high number of modes needs to be included in the calculations in order to get accurate results. Then, the model was used to investigate the noise attenuation mechanisms involved in the HQ system. An impedance analysis first showed that the HQ system provides good reduction at discrete frequencies corresponding to the resonance of the coupled HQ tube-duct system. The dynamics of the inlet duct actually modify the resonance behavior of the tube itself and cause the tube resonant frequencies to shift down. The noise control mechanisms involved in the HQ-concept were investigated by studying the modal amplitudes of the incident, reflected and transmitted modes. This showed that in the presence of the HQ system, incident modes not only are reflected back to the fan but also are scattered into other radial and circumferential order modes. Thus, the reduction of the acoustic energy in a particular mode is due to the recombination of scattered energy due to the other incident modes. It was shown that a preferable design strategy consists of using a higher number of HQ tubes in order to avoid scattering of energy into propagating circumferential modes. It is important to remark that this conclusion is only valid for the case of a hard wall inlet.

Based on the fact that inlet duct modes are spinning forming helixes, new advanced configurations for the HQ system were investigated. Tubes were first placed in helix patterns with tubes parallel to the inlet axis. Then, the HQ system was based on a circumferential array with tubes placed at an angle relative to the inlet duct axis. Finally, both systems were combined and tubes were placed in a helix and rotated at the same angle as the helix. These advanced HQ-configurations showed potential for improving the effectiveness of the HQ system.

The TBIEM3D code was modified to allow for modeling of HQ tubes. The main advantage of this modeling tool is that the effect of a liner can easily be incorporated. A

performance study of combining the HQ-array with a liner was initiated. The results showed that a HQ-liner system outperforms both systems separately.

6. RECOMMENDATIONS FOR FUTURE RESEARCH

In contrast to the absorptive characteristics of liners, the HQ-system is mainly a reactive system with some absorptive properties through the resistive component of the perforated screen used at the interface between the tubes and the inlet duct. Thus, the main drawback of the current models is that they do not take into account the effect of the fan through reflection and scattering of the energy reflected back towards the fan. Therefore, it is important to include the effect of the fan in the modeling to investigate if it affects the performance of the HQ system. This study should be performed for both the HQ-system on a hard walled duct as well as the HQ-system combined with liners.

An interesting extension of this work would consist of combining the HQ tubes system with traditional passive liners. It is also important to investigate how the HQ-system affects the design of the liner from current practice. The optimum integration of the HQ-liner system is a topic currently being investigated at Virginia Tech under a program sponsored by Goodrich Aerospace [9].

This work was focused on the HQ system applied to the inlet of the turbofan engine. However, this concept could be easily applied to the aft of the engine. However, in this case, the modeling approach would have to be modified since the aft radiation consists of a conical duct.

The modeling approach described in this report is valid for frequencies below the first cut-off frequency of the HQ-waveguide. Thus, it is assumed that only plane waves exit inside the waveguides. However, at frequencies higher than the first tube cut-off frequency this assumption breaks down. The modeling at higher frequencies is a research topic of interest because the HQ-tubes at these higher frequencies most probably behave as a "cavity absorber".

Finally, most of the work here concentrated in designing the HQ-system to maximize the acoustic power reduction. However, the cancellation of noise towards a specific sector on the far-field could be more beneficial than the control of the total radiated power. Thus, the relationship of the HQ-parameters in terms of the attenuation of the far-field radiated noise should be investigated.

ACKNOWLEDGEMENTS

This work was supported by the Aeroacoustics Branch of the NASA Langley Research Center and is gratefully acknowledged. The technical monitors for this work are Dr. Carl Gerhold and Dr. Joe Posey.

REFERENCES

[1] Smith, J. P. and Burdisso, R. A., "The Application of the Herschel-Quincke Tube Concept for the Reduction of Tonal and Broadband Noise From Turbofan Engines," VPI report VPI-ENGR.98.167, prepared for NASA under grant # NAG-1-1980 and proposal # 98-0448-10, 1998.

[2] Dunn M.H., "TBIEM3D – A Computer Program For Predicting Ducted Fan Engine Noise", Version 1.1. NASA/CR-97-206232, 1997.

[3] Dunn M.H., Tweed J., and Farassat F., "The Prediction Of Ducted Fan Engine Noise Via A Boundary Integral Equation Method," AIAA Paper 96-1770, May 1996.

[4] Hallez, R. F., "Investigation of the Herschel-Quincke Concept as a Noise Control Device for Turbofan Engines," M. S. Thesis, Virginia Polytechnic Institute and State University, January 2001.

[5] Goldberg, D., "Genetic Algorithms in Search, Optimization and Machine Learning," Addison-Wesley, (1989)

[6] Smith, J. P. and Burdisso, R. A., "Experimental Investigation of the Herschel-Quincke Tube Concept on the Honeywell TFE731-60 Engine," VPI report prepared for NASA under grant # NAG-1-1980 and proposal # 98-0448-10, 2001.

[7] Brady, L. A., Burdisso, R. A., and Smith, J. P., "Investigation of the Herschel-Quincke Tube Concept for the Suppression of Higher-order Modes in a Duct," Proceedings of Internoise 99, pp. 545-550, Fort Lauderdale Florida, December (1999).

[8] Hutchinson F. V., "Advanced Modeling Of Active Control Of Fan Noise For Ultra High Bypass Turbofan Engines," Doctoral Dissertation, Virginia Polytechnic Institute and State University, December 1999.

[9] "Development of a Combined Liner Herschel-Quincke Tube System for Reduction of Inlet Noise From Turbofan Engines," Research project funded by Goodrich, Aerostructures Group (Rohr), 2000-2002.

APPENDIX A

In this appendix, the detail formulation of the modeling of the HQ-tubes on an infinite hard wall duct is presented. This Appendix has several sections as: (i) the eigenvalue problem to determine the cut-off frequencies and the acoustic duct modes, (ii) the development of the Green's function, (iii) the acoustic field generated by a piston source on the duct wall, (iv) the pressure over a piston source due to a unit velocity of another piston, i.e. impedance function, (v) the pressure over a piston due to the fan disturbance, (vi) the acoustic field of the HQ-tubes, and finally (vii) the modal amplitudes and acoustic power upstream of the HQ tube system.

A.1 Eigenvalue problem

The duct considered here is of infinite length and radius a. The cylindrical coordinates system used in the analysis is shown in Figure A.1. The positive z-direction is chosen to be the direction of sound propagation. It is assumed that a uniform flow field with Mach number M is propagating in the positive z-direction. For the particular case of turbofan engine inlets, this Mach number will be negative since the flow is propagating in the opposite direction.

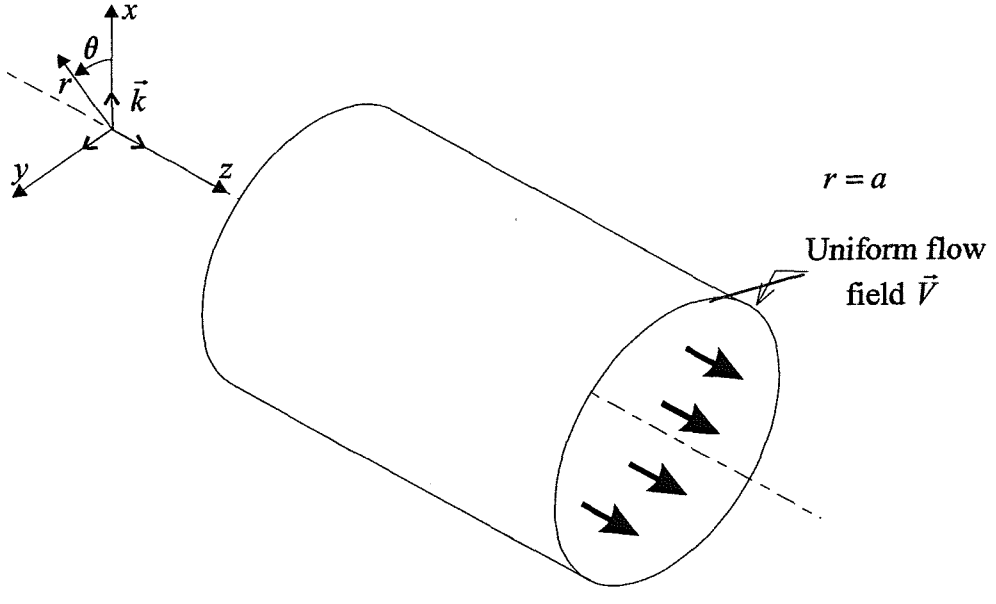

Figure A.1: Model of the infinite cylindrical duct with flow.

The general form of the acoustic wave equation in a moving media is given as

$$\nabla^2 p = \frac{1}{c^2}\left(\frac{\partial}{\partial t} + \vec{V}\cdot\nabla\right)^2 p \qquad \text{(A.1)}$$

where ∇^2 is the Laplacian operator, c is the speed of sound, p is the acoustic pressure, and $\vec{V}$ is the flow velocity field vector. Assuming a uniform flow field in the positive z-

direction (along the duct axis), i.e. $\vec{V} = cM\vec{k}$ where $\vec{k}$ is the unit vector in the z-direction, and considering a harmonic motion, equation (A.1) in cylindrical coordinates becomes

$$\frac{\partial^2 p}{\partial r^2}+\frac{1}{r}\frac{\partial p}{\partial r}+\frac{1}{r^2}\frac{\partial^2 p}{\partial \theta^2}+\frac{\partial^2 p}{\partial z^2}=-k_o^2 p+2ik_o M\frac{\partial p}{\partial z}+M^2\frac{\partial^2 p}{\partial z^2} \tag{A.2}$$

where k_o is the free field wavenumber. The solution to the partial differential equation (A.2) is assumed to be a propagating wave in the z-direction and have the form

$$p(r,\theta,z,t)=\Phi(r,\theta)e^{-ik_z z}e^{i\omega t} \tag{A.3}$$

where k_z is the axial wave number and $\Phi(r,\theta)$ is the acoustic mode shape function. The time function $e^{i\omega t}$ is omitted for the rest of the derivation.

Replacing (A.3) into equation (A.2) and canceling out the term $e^{-ik_z z}$ gives

$$\frac{\partial^2 \Phi}{\partial r^2}+\frac{1}{r}\frac{\partial \Phi}{\partial r}+\frac{1}{r^2}\frac{\partial^2 \Phi}{\partial \theta^2}+\left\{k_o^2-k_z^2\left(1-M^2\right)-2k_o k_z M\right\}\Phi=0 \tag{A.4}$$

The solution of this equation is obtained using separation of variables as

$$\Phi(r,\theta)=R(r)\Theta(\theta) \tag{A.5}$$

Replacing (A.5) into (A.4) and multiplying by $r^2/\left[R(r)\Theta(\theta)\right]$ gives

$$\frac{r^2}{R}\left(\frac{d^2R}{dr^2}+\frac{1}{r}\frac{dR}{dr}\right)+\frac{1}{\Theta}\frac{d^2\Theta}{d\theta^2}+r^2k_{mn}^2=0 \tag{A.6}$$

where

$$k_{mn}^2=k_o^2-k_z^2(1-M^2)-2k_o k_z M \tag{A.7}$$

Each term in equation (A.6) must be a constant and thus implies that

$$\frac{1}{\Theta}\frac{d^2\Theta}{d\theta^2}=-m^2 \tag{A.8}$$

where $\Theta(\theta)$ must be a periodic function with period 2π. Therefore, for stationary modes, the solution of equation (A.8) takes the form

$$\Theta(\theta) = A\cos(m\theta) + B\sin(m\theta) \qquad m=0, 1, 2,\ldots \qquad \text{(A.9)}$$

The solution to (A.8) can also take the form of spinning modes as

$$\Theta(\theta) = Ae^{im\theta} + Be^{-im\theta} \qquad m=0, 1, 2,\ldots \qquad \text{(A.10)}$$

where A and B are the amplitudes of the mode spinning in the negative and positive θ-direction, respectively.

Equation (A.6) is written in term of $R(r)$ as

$$\frac{r^2}{R}\left(\frac{d^2R}{dr^2} + \frac{1}{r}\frac{dR}{dr}\right) - m^2 + r^2k_{mn}^2 = 0 \qquad \text{(A.11)}$$

The solution of this equation takes the form

$$R(r) = CJ_m(k_{mn}r) + DY_m(k_{mn}r) \qquad \text{(A.12)}$$

where J_m is the first kind Bessel function of m^{th} order, Y_m is the second kind Bessel function or Neumann's function of m^{th} order and C and D are constants. Because Y_m has a singularity at the origin and the pressure field has to be bounded for any $r \le a$, the constant D is set to zero. Thus, equation (A.12) can be written as

$$R(r) = CJ_m(k_{mn}r) \qquad \text{(A.13)}$$

For a rigid-wall duct, the radial particle velocity on the wall must vanish. Therefore

$$\left.\frac{\partial p}{\partial r}\right|_{r=a} = \left.\frac{\partial \Phi}{\partial r}\right|_{r=a} = \left.\frac{dR}{dr}\right|_{r=a} = 0 \qquad \text{(A.14)}$$

Thus, replacing equation (A.13) into the preceding boundary condition (A.14) yields

$$\left.\frac{dJ_m}{dr}(k_{mn}r)\right|_{r=a} = 0 \qquad \text{(A.15)}$$

where k_{mn} are the values that satisfy the boundary condition. For each m value, there are actually many roots that satisfy this equation. The k_{mn} values are called the eigenvalues and are written as

$$k_{mn} = \frac{\chi_{mn}}{a} \qquad m=0, 1, 2, \ldots\ n=0, 1, 2,\ldots \qquad \text{(A.16)}$$

defining χ_{mn} as the inflection points of the Bessel's function of the first kind of order m. For each m index, there are many values that satisfy equation (A.16), these values are designated by the index n, where n=0 corresponds to the first value.

Finally, the expression for the mode shapes is

$$\Phi_{mn}(r,\theta) = \Theta(\theta) J_m(k_{mn} r) \qquad m=0, 1, 2, \ldots \; n=0, 1, 2, \ldots \quad \text{(A.17)}$$

where the function $\Theta(\theta)$ corresponds to stationary or spinning waves as shown in equations (A.9) and (A.10) respectively, depending on the actual excitations.

The axial wavenumber k_z is found using

$$k_{mn}^2 = k_o^2 - k_z^2\left(1-M^2\right) - 2k_o k_z M \quad \text{(A.18)}$$

which yields

$$k_z = \left\{-Mk_o \pm \sqrt{k_o^2 - \left(1-M^2\right)k_{mn}^2}\right\} / \left(1-M^2\right) \quad \text{(A.19)}$$

Thus, there are two values for k_z corresponding to positive and negative traveling waves. The modes can also be propagating or decaying depending on the following conditions:

(i) If $k_o > k_{mn}\sqrt{\left(1-M^2\right)}$ the mode will propagate

(ii) If $k_o < k_{mn}\sqrt{\left(1-M^2\right)}$ the mode will decay

The frequency where $k_o = k_{mn}\sqrt{\left(1-M^2\right)}$ is called cut-off frequency and is written as

$$f_{cut-off} = \frac{c}{2\pi} k_{mn}\sqrt{\left(1-M^2\right)} \quad \text{(A.20)}$$

Based on the above conditions, there are four possible cases for the axial wavenumber

i) Positive traveling mode: $$k_z^{(+)} = \left\{-Mk_o + \sqrt{k_o^2 - \left(1-M^2\right)k_{mn}^2}\right\} / \left(1-M^2\right) \quad \text{(A.21)}$$

ii) Positive decaying mode: $$k_z^{(+)} = \left\{-Mk_o - i\sqrt{\left(1-M^2\right)k_{mn}^2 - k_o^2}\right\} / \left(1-M^2\right) \quad \text{(A.22)}$$

iii) Negative traveling mode: $$k_z^{(-)} = \left\{-Mk_o - \sqrt{k_o^2 - \left(1-M^2\right)k_{mn}^2}\right\} / \left(1-M^2\right) \quad \text{(A.23)}$$

iv) Negative decaying mode: $$k_z^{(-)} = \left\{-Mk_o + i\sqrt{\left(1-M^2\right)k_{mn}^2 - k_o^2}\right\} / \left(1-M^2\right) \quad \text{(A.24)}$$

Finally, the pressure field in the duct can be expressed as a sum of circumferential and radial modes traveling in both directions as

$$p(r,\theta,z) = \sum_{m=0}^{N_\theta}\sum_{n=0}^{N_r} A_{mn}^{(+)}\Phi_{mn}(r,\theta)e^{-ik_z^{(+)}z} + \sum_{m=0}^{N_\theta}\sum_{n=0}^{N_r} A_{mn}^{(-)}\Phi_{mn}(r,\theta)e^{-ik_z^{(-)}z} \quad \text{(A.25)}$$

where $A_{mn}^{(+)}$ and $A_{mn}^{(-)}$ are the amplitude of the positive and negative waves, respectively, and N_θ and N_r are the number of circumferential and radial modes used in the expansion, respectively.

A.2 Green's function

Here the Green's function, i.e. the pressure field generated by a point source on the duct wall, is derived. The Green's function will then be used to find the pressure field radiated by a piston source on the duct wall. This will allow to model the effect of the tubes on the duct, since each interface between the duct and the HQ tubes is modeled as a finite piston source. Finally, the average pressure over a source due to another piston source with unit velocity, i.e. impedance function, will be developed.

To find an expression for the Green's function, the following differential equation needs to be solved (see equation (A.2))

$$\frac{\partial^2 g}{\partial r^2} + \frac{1}{r}\frac{\partial g}{\partial r} + \frac{1}{r^2}\frac{\partial^2 g}{\partial \theta^2} + \frac{\partial^2 g}{\partial z^2}\left(1-M^2\right) - 2Mik_o\frac{\partial g}{\partial z} + k_o^2 g = \delta(r-r_o)\delta(\theta-\theta_o)\delta(z-z_o) \quad \text{(A.26)}$$

where $g(r,\theta,z\,|\,r_o,\theta_o,z_o)$ is the Green's function for a point source located at (r_o,θ_o,z_o). The solution to this equation is expanded in terms of the rigid-walled duct mode shapes found in the previous section as

$$g(r,\theta,z\,|\,r_o,\theta_o,z_o) = \sum_{m=0}^{Mg}\sum_{n=0}^{Ng} F_{mn}(z)\Phi_{mn}(r,\theta) \quad \text{(A.27)}$$

where M_g and N_g indicate the number of circumferential and radial modes included in the Green's function, respectively. To satisfy the symmetry of the sound field with respect to the plane defined by the point (r_o,θ_o) and the z-axis, the duct modes are selected as

$$\Phi_{mn}(r,\theta)=\cos\left[m(\theta-\theta_o)\right]J_m(k_{mn}r) \tag{A.28}$$

Replacing equation (A.27) into (A.26) gives

$$\sum_{m=0}^{M_g}\sum_{n=0}^{N_g}\left\{\frac{d^2F_{mn}}{dz^2}(1-M^2)-2iMk_o\frac{dF_{mn}}{dz}-k_{mn}^2F_{mn}+k_o^2F_{mn}\right\}\Phi_{mn}(r,\theta) = \delta(r-r_o)\delta(\theta-\theta_o)\delta(z-z_o) \tag{A.29}$$

where (from equations (A.4) and (A.7))

$$-k_{mn}^2\Phi_{mn}=\frac{\partial^2\Phi_{mn}}{\partial r^2}+\frac{1}{r}\frac{\partial\Phi_{mn}}{\partial r}+\frac{1}{r^2}\frac{\partial^2\Phi_{mn}}{\partial\theta^2} \tag{A.30}$$

By definition, the mode shapes are orthogonal. Thus, the orthogonality condition is written as

$$\int_0^{2\pi}\int_0^a\Phi_{rs}(r,\theta)\Phi_{mn}(r,\theta)rdrd\theta=\pi a^2\Lambda_{mn}\delta_{rm}\delta_{sn} \tag{A.31}$$

where the orthogonality constant is given by

$$\Lambda_{mn}=\begin{cases}J_m^2(k_{mn}a) & \text{if } m=0\\ \frac{1}{2}\left[1-\frac{m^2}{(k_{mn}a)^2}\right]J_m^2(k_{mn}a) & \text{if } m\neq 0\end{cases} \tag{A.32}$$

Thus, premultiplying equation (A.29) by the mode shape $\Phi_{rs}(r,\theta)$, integrating over the duct cross-section, and considering the orthogonality condition gives

$$\frac{d^2F_{mn}}{dz^2}(1-M^2)-2iMk_o\frac{dF_{mn}}{dz}-\left(k_{mn}^2-k_o^2\right)F_{mn}=\delta(z-z_o)\frac{\Phi_{mn}(r_o,\theta_o)}{\pi a^2\Lambda_{mn}} \tag{A.33}$$

Equation (A.33) is an ordinary differential equation in z, which is solved assuming the solutions for positions upstream and downstream of the source as

$$F_{mn}(z)=\mathrm{A}_{mn}e^{-ik_z^{(+)}(z-z_o)} \qquad for\ z\geq z_o \tag{A.34}$$

$$F_{mn}(z)=\mathrm{A}_{mn}e^{-ik_z^{(-)}(z-z_o)} \qquad for\ z\leq z_o \tag{A.35}$$

Note that by selecting the same amplitude A_{mn} for both solutions, the sound field is uniquely defined at $z=z_0$.

To find the unknown amplitude A_{mn}, the following integral needs to be solved

$$\lim_{\varepsilon\to 0}\int_{z_o-\varepsilon}^{z_o+\varepsilon}\left[\frac{d^2F_{mn}}{dz^2}(1-M^2)-2iMk_o\frac{dF_{mn}}{dz}-\left(k_{mn}^2-k_o^2\right)F_{mn}\right]dz=\frac{\Phi_{mn}(r_o,\theta_o)}{\pi a^2\Lambda_{mn}} \quad \text{(A.36)}$$

thus

$$\lim_{\varepsilon\to 0}\left\{(1-M^2)\left[\left.\frac{dF_{mn}}{dz}\right|_{z_o+\varepsilon}-\left.\frac{dF_{mn}}{dz}\right|_{z_o-\varepsilon}\right]\right\}=\frac{\Phi_{mn}(r_o,\theta_o)}{\pi a^2\Lambda_{mn}} \quad \text{(A.37)}$$

Replacing equations (A.34) and (A.35) for the upper and lower limits respectively in (A.37) yields

$$\lim_{\varepsilon\to 0}\left(1-M^2\right)\left[\mathrm{A}_{mn}\left(-ik_z^{(+)}\right)e^{ik_z^{(+)}(+\varepsilon)}-\mathrm{A}_{mn}\left(-ik_z^{(-)}\right)e^{ik_z^{(-)}(-\varepsilon)}\right]=\frac{\Phi_{mn}(r_o,\theta_o)}{\pi a^2\Lambda_{mn}} \quad \text{(A.38)}$$

Taking the limit yields

$$-\mathrm{A}_{mn}i\left(1-M^2\right)\left(k_z^{(+)}-k_z^{(-)}\right)=\frac{\Phi_{mn}(r_o,\theta_o)}{\pi a^2\Lambda_{mn}} \quad \text{(A.39)}$$

Solving for A_{mn} and replacing back into (A.34) and (A.35) and then into (A.27) gives

$$g^{(+)}\left(r,\theta,z\,|\,r_o,\theta_o,z_o\right)=\frac{i}{\pi a^2}\sum_{m=0}^{M_g}\sum_{n=0}^{N_g}\frac{\Phi_{mn}(r,\theta)\Phi_{mn}(r_o,\theta_o)}{\Lambda_{mn}\left(1-M^2\right)\left(k_z^{(+)}-k_z^{(-)}\right)}e^{-ik_z^{(+)}(z-z_o)}\ \textit{for}\ z\geq z_o \quad \text{(A.40)}$$

$$g^{(-)}\left(r,\theta,z\,|\,r_o,\theta_o,z_o\right)=\frac{i}{\pi a^2}\sum_{m=0}^{M_g}\sum_{n=0}^{N_g}\frac{\Phi_{mn}(r,\theta)\Phi_{mn}(r_o,\theta_o)}{\Lambda_{mn}\left(1-M^2\right)\left(k_z^{(+)}-k_z^{(-)}\right)}e^{-ik_z^{(-)}(z-z_o)}\ \textit{for}\ z\leq z_o \quad \text{(A.41)}$$

which are the Green's functions for positive and negative z-propagation direction, respectively.

A.3 Finite piston source sound field

Once the Green's function for a point source on the duct wall is found, the sound field generated by a finite piston source as illustrated in Figure A.2 can be derived. The finite piston source of normal velocity v radiating into the duct is the model of a Herschel-Quincke tube end at the interface with the duct. Note that for modeling purposes, the interface between the tube's end and the inlet is assumed to be of rectangular shape, i.e. the interface is defined by constant values of the coordinates. This shape allows the solution of the equations in closed form.

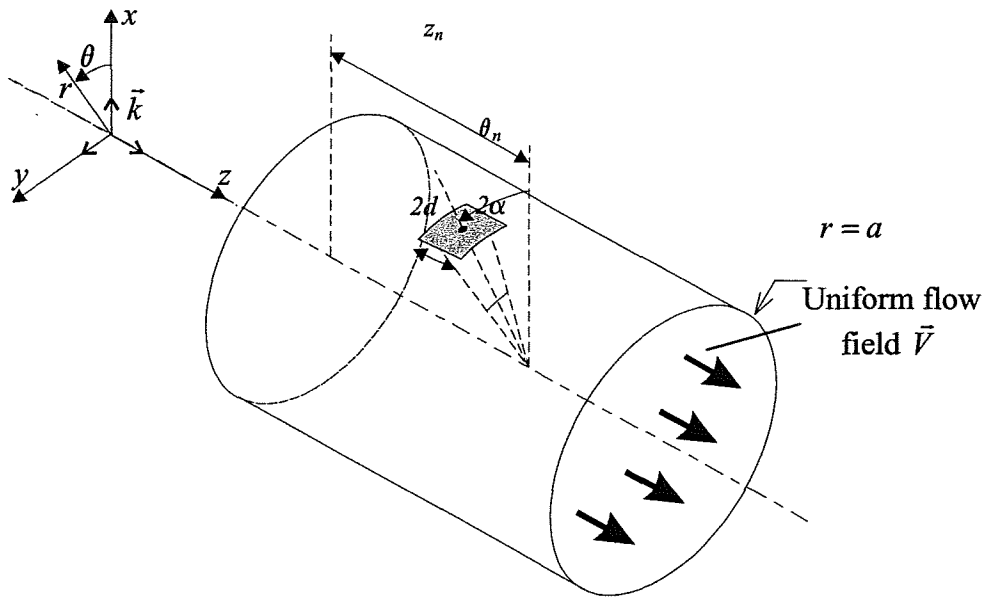

Figure A.2: Piston Source radiating into the duct.

The pressure at a point inside the duct *(r,θ,z)* due to the n^{th} piston source on the duct wall with source velocity v_n is obtained by integrating the Green's function over the surface of the source as

$$p(r,\theta,z|a,\theta_n,z_n) = -i\omega\rho v_n \int_{z_n-d}^{z_n+d}\int_{\theta_n-\alpha}^{\theta_n+\alpha} g(r,\theta,z\,|\,a,\tilde{\theta},\tilde{z})ad\tilde{\theta}d\tilde{z} \qquad \text{(A.42)}$$

where (a,θ_n,z_n) is the location of the source center as defined in Figure A.2. Replacing (A.40) or (A.41) into (A.42), it is clear that there are two integrals that need to be solved. The first one with respect to θ is easily obtained as

$$\int_{\theta_n-\alpha}^{\theta_n+\alpha} \cos m\left(\theta-\tilde{\theta}\right)ad\tilde{\theta} = \kappa_\theta(\alpha)\cos m\left(\theta-\theta_n\right) \qquad \text{(A.43)}$$

where $\kappa_\theta(\alpha) = \dfrac{2a\alpha\sin(m\alpha)}{m\alpha}$

For the special case of m=0 equation (A.43) gives $2a\alpha$.

The solution of the second integral depends on the position of the observation point z relative to the piston source position z_n. Three cases are considered as illustrated in Figure A-3.

CASE 1: The observation point is downstream of the source, i.e. $z > z_n + d$. This case is illustrated in Figure A-3a and implies that $z > \tilde{z}$. Thus, the following integral is solved as

$$\int_{z_n-d}^{z_n+d} e^{-ik_z^+(z-\tilde{z})}d\tilde{z} = e^{-ik_z^{(+)}(z-z_n)}\frac{\sin(k_z^{(+)}d)}{k_z^{(+)}d}2d \tag{A.44}$$

The pressure due to the source positioned at (a,θ_n,z_n) is then

$$\begin{aligned} p(r,\theta,z\,|\,a,\theta_n,z_n) = v_n\frac{k_0\rho c}{\pi a^2}\sum_m^{M_g}\sum_n^{N_g}\frac{\kappa_\theta(\alpha)\cos m(\theta-\theta_n)J_m(k_{mn}r)J_m(k_{mn}a)}{\Lambda_{mn}(1-M^2)(k_z^{(+)}-k_z^{(-)})} \\ \times e^{-ik_z^{(+)}(z-z_n)}\frac{\sin(k_z^{(+)}d)}{k_z^{(+)}d}2d \end{aligned} \tag{A.45}$$

CASE 2: The observation point is upstream of the source, i.e. $z < z_n - d$. This case is illustrated in Figure A-3b and implies that $z < \tilde{z}$. Thus, the following integral is solved as

$$\int_{z_n-d}^{z_n+d} e^{-ik_z^{(-)}(z-\tilde{z})}d\tilde{z} = e^{-ik_z^{(-)}(z-z_n)}\frac{\sin(k_z^{(-)}d)}{k_z^{(-)}d}2d \tag{A.46}$$

The pressure due to the source is then written as

$$\begin{aligned} p(r,\theta,z\,|\,a,\theta_n,z_n) = v_n\frac{k_0\rho c}{\pi a^2}\sum_m^{M_g}\sum_n^{N_g}\frac{\kappa_\theta(\alpha)\cos m(\theta-\theta_n)J_m(k_{mn}r)J_m(k_{mn}a)}{\Lambda_{mn}(1-M^2)(k_z^{(+)}-k_z^{(-)})} \\ \times e^{-ik_z^{(-)}(z-z_n)}\frac{\sin(k_z^{(-)}d)}{k_z^{(-)}d}2d \end{aligned} \tag{A.47}$$

CASE 3: The observation point is on the surface of the source, i.e. $z_n - d < z < z_n + d$. This case is illustrated in Figure A-3c and requires to solve the integral with the two terms

$$\int_{z_n-d}^{z} e^{-ik_z^{(+)}(z-\tilde{z})}d\tilde{z} + \int_{z}^{z_n+d} e^{-ik_z^{(-)}(z-\tilde{z})}d\tilde{z} = \frac{1-e^{-ik_z^{(+)}(z-z_n+d)}}{ik_z^{(+)}} - \frac{1-e^{-ik_z^{(-)}(z-z_n-d)}}{ik_z^{(-)}} \tag{A.48}$$

The pressure due to the source is then written as

$$\begin{aligned} p(r,\theta,z\,|\,a,\theta_n,z_n) = v_n\frac{k_0\rho c}{\pi a^2}\sum_m^{M_g}\sum_n^{N_g}\frac{\kappa_\theta(\alpha)\cos m(\theta-\theta_n)J_m(k_{mn}r)J_m(k_{mn}a)}{\Lambda_{mn}(1-M^2)(k_z^{(+)}-k_z^{(-)})} \\ \times\left[\frac{1-e^{-ik_z^{(+)}(z-z_n+d)}}{ik_z^{(+)}} - \frac{1-e^{-ik_z^{(-)}(z-z_n-d)}}{ik_z^{(-)}}\right] \end{aligned} \tag{A.49}$$

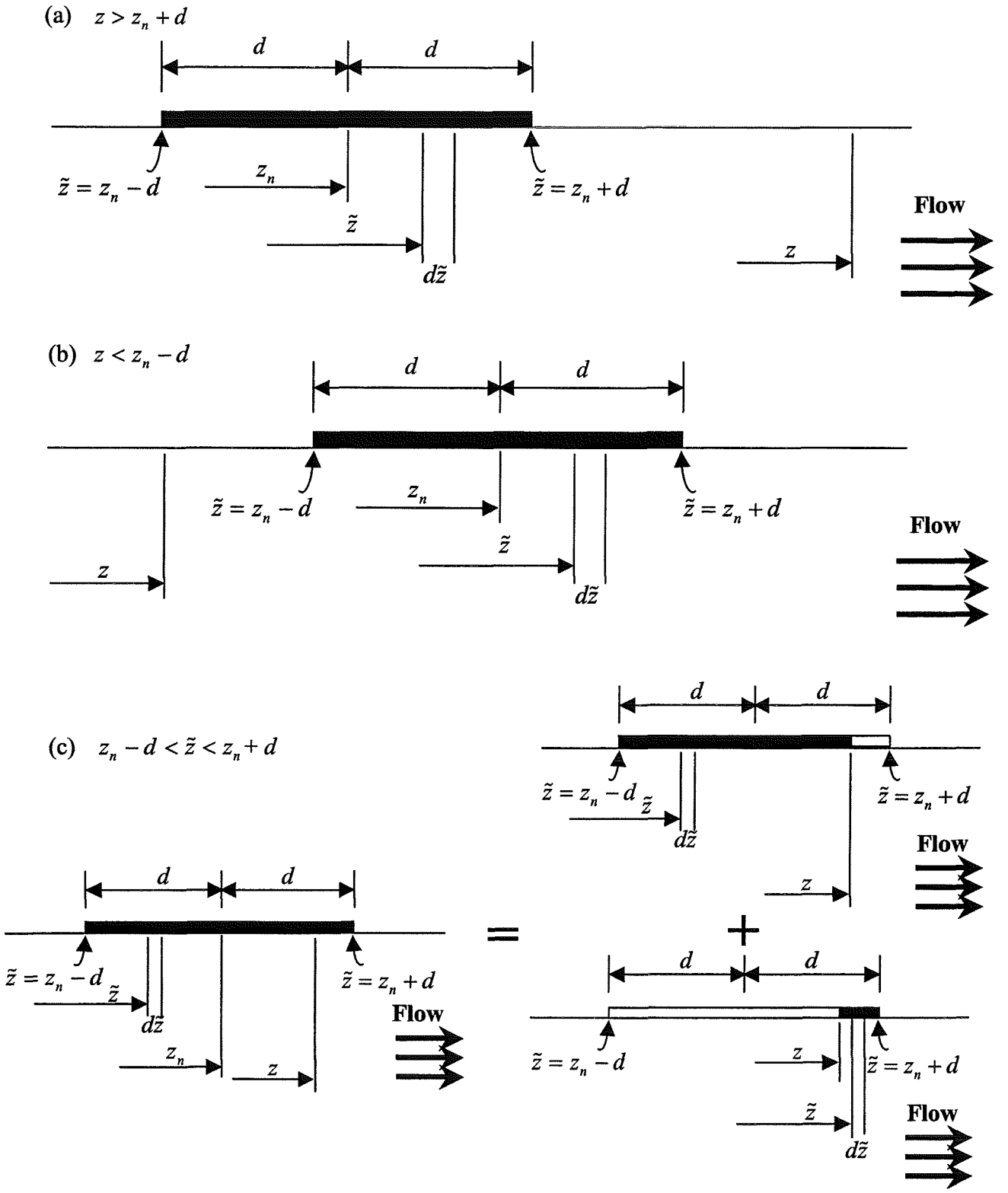

Figure A-3: Elements of integration over the source surface (a) case 1: observation point is downstream of the source, (b) case 2: observation point is upstream of the source, (c) case 3: observation point is on the surface of the source.

In the development of the HQ model, it is also required to compute the average pressure over a source due to another piston source with unit velocity, i.e. impedance function. The average pressure over a piston source "*r*" located at (a,θ_r,z_r) due to another source "*s*" located at (a,θ_s,z_s) with unit velocity is simply given as

$$Z_{rs} = \frac{1}{S_r}\int_{z_r-d_r}^{z_r+d_r}\int_{\theta_r-\alpha_r}^{\theta_r+\alpha_r} p(a,\theta,z \mid a,\theta_s,z_s)\,a\,d\theta\,dz \tag{A..50}$$

where S_r is the area of the piston source "*r*". Once again, two integrals need to be solved separately. The first integral with respect to θ is

$$\int_{\theta_r-\alpha_r}^{\theta_r+\alpha_r} \cos m(\theta-\theta_s)\,a\,d\theta = \kappa_\theta(\alpha_r)\cos m(\theta_r-\theta_s) \tag{A..51}$$

The second integral is with respect to the *z*-coordinate which depends on the location of the observation source "*r*" relative to the "*s*" source. Three cases are again possible as illustrated in Figure A.4.

CASE 1: The observation source "*r*" is downstream of source "*s*", i.e. $z_r - d_r > z_s + d_s$. In this case, equation (A.45) is replaced into (A.50) and the following integral is solved

$$\int_{z_r-d_r}^{z_r+d_r} e^{-ik_z^{(+)}(z-z_s)}\frac{\sin(k_z^{(+)}d_s)}{k_z^{(+)}d_s}2d_s\,dz = e^{-ik_z^{(+)}(z_r-z_s)}\frac{\sin(k_z^{(+)}d_r)}{k_z^{(+)}d_r}2d_r\frac{\sin(k_z^{(+)}d_s)}{k_z^{(+)}d_s}2d_s \tag{A.52}$$

The impedance function in this case is

$$Z_{rs} = \frac{k_0\rho c}{S_r\pi a^2}\sum_m^{M_g}\sum_n^{N_g}\frac{\kappa_\theta(\alpha_r)\kappa_\theta(\alpha_s)\cos m(\theta_r-\theta_s)J_m(k_{mn}a)J_m(k_{mn}a)}{\Lambda_{mn}(1-M^2)(k_z^{(+)}-k_z^{(-)})} \times e^{-ik_z^{(+)}(z_r-z_s)}\frac{\sin(k_z^{(+)}d_r)}{k_z^{(+)}d_r}2d_r\frac{\sin(k_z^{(+)}d_s)}{k_z^{(+)}d_s}2d_s \tag{A.53}$$

CASE 2: The observation source "*r*" is upstream of source "*s*", i.e. $z_r + d_r < z_s - d_s$. In this case, equation (A.47) is replaced into (A.50) and the following integral is solved

$$\int_{z_r-d_r}^{z_r+d_r} e^{-ik_z^{(-)}(z-z_s)}\frac{\sin(k_z^{(-)}d_s)}{k_z^{(-)}d_s}2d_s\,dz = e^{-ik_z^{(-)}(z_r-z_s)}\frac{\sin(k_z^{(-)}d_r)}{k_z^{(-)}d_r}2d_r\frac{\sin(k_z^{(-)}d_s)}{k_z^{(-)}d_s}2d_s \tag{A..54}$$

The impedance function in this case is

$$Z_{rs} = \frac{k_0 \rho c}{S_r \pi a^2} \sum_m^{M_g} \sum_n^{N_g} \frac{\kappa_\theta(\alpha_r)\kappa_\theta(\alpha_s)\cos m(\theta_r - \theta_s) J_m(k_{mn}a) J_m(k_{mn}a)}{\Lambda_{mn}(1-M^2)(k_z^{(+)} - k_z^{(-)})} \times e^{-ik_z^{(-)}(z_r - z_s)} \frac{\sin(k_z^{(-)} d_r)}{k_z^{(-)} d_r} 2d_r \frac{\sin(k_z^{(-)} d_s)}{k_z^{(-)} d_s} 2d_s \quad \text{(A..55)}$$

CASE 3: The observation source "*r*" is at the same axial location as source "*s*". In addition, we assume they have the same dimensions, i.e. d_r=d_s. In this case, equation (A.49) is replaced into (A.50) and the following integral is solved

$$\int_{z_r - d_r}^{z_r + d_r} \left[\frac{1 - e^{-ik_z^{(+)}(z - z_s + d_s)}}{ik_z^{(+)}} - \frac{1 - e^{-ik_z^{(-)}(z - z_s - d_s)}}{ik_z^{(-)}} \right] dz = \frac{2d_r}{ik_z^{(+)}} - \frac{2d_r}{ik_z^{(-)}} + \frac{1 - e^{-ik_z^{(+)} 2d_r}}{\left(k_z^{(+)}\right)^2} + \frac{1 - e^{ik_z^{(-)} 2d_r}}{\left(k_z^{(-)}\right)^2} \quad \text{(A..56)}$$

Thus, the impedance function is

$$Z_{rs} = \frac{k_0 \rho c}{S_r \pi a^2} \sum_m^{M_g} \sum_n^{N_g} \frac{\kappa_\theta(\alpha_r)\kappa_\theta(\alpha_s)\cos m(\theta_r - \theta_s) J_m(k_{mn}a) J_m(k_{mn}a)}{\Lambda_{mn}(1-M^2)(k_z^{(+)} - k_z^{(-)})} \times \left[\frac{2d_r}{ik_z^{(+)}} - \frac{2d_r}{ik_z^{(-)}} + \frac{1 - e^{-ik_z^{(+)} 2d_r}}{\left(k_z^{(+)}\right)^2} + \frac{1 - e^{ik_z^{(-)} 2d_r}}{\left(k_z^{(-)}\right)^2} \right] \quad \text{(A..57)}$$

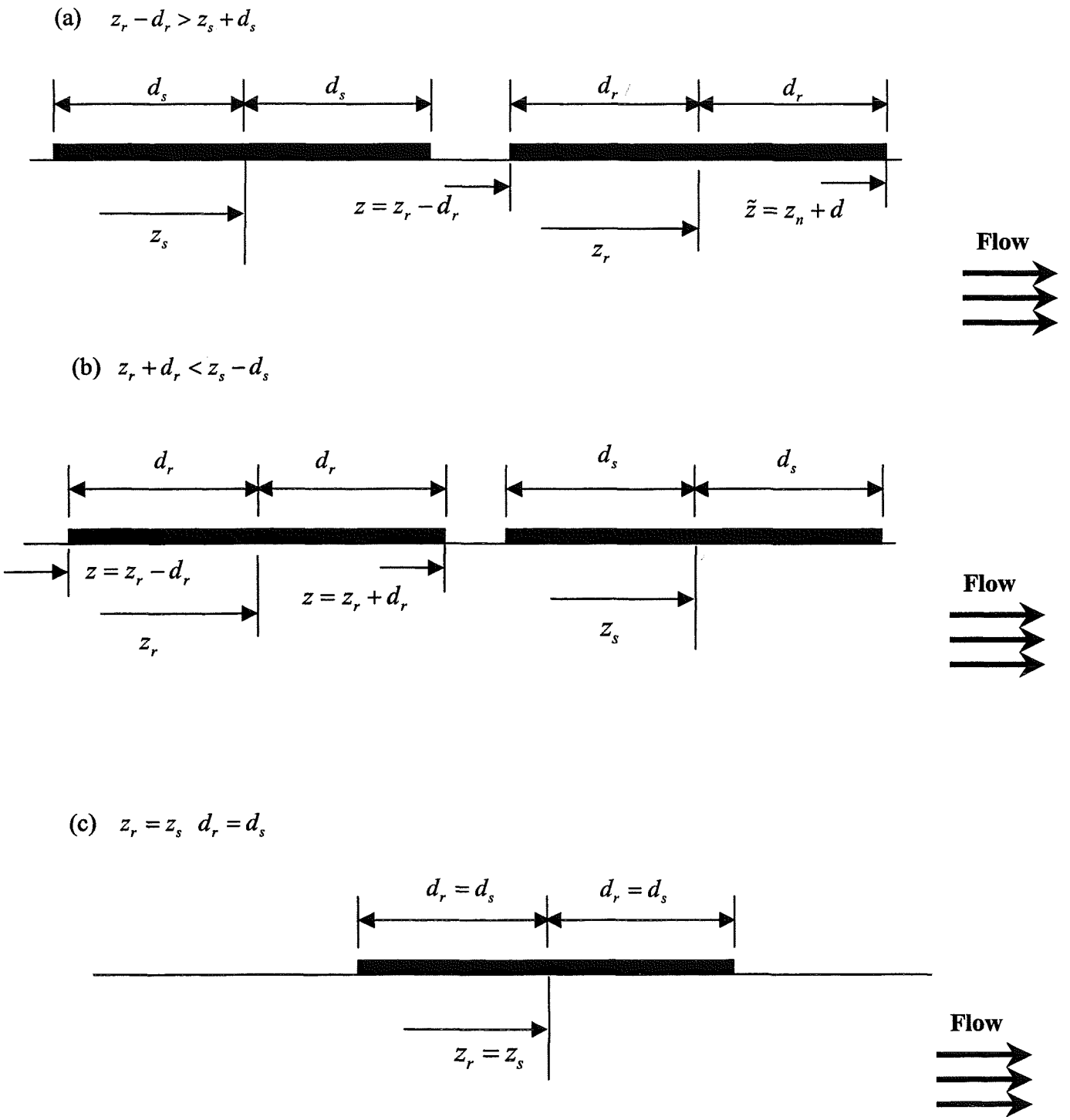

Figure A.4: (a) observation source *"r"* is downstream of the source *"s"*, (b) observation source *"r"* is upstream of the source *"s"*, (c) observation source *"r"* and source *"s"* are at the same axial location.

A.4 Pressure field due to fan

The pressure due to the disturbance p_d, at any point in the duct can be expressed as the sum of a set of positive and negative spinning modes traveling in the positive z-direction as

$$p_d(r,\theta,z)=\sum_{m=0}^{M_d}\sum_{n=0}^{N_d}\left((A_{mn}^d)^{pos}e^{-im\theta}+(A_{mn}^d)^{neg}e^{im\theta}\right)J_m\left(k_{mn}r\right)e^{-ik_z^{(+)}z} \tag{A.58}$$

where A_{mn}^d is the complex amplitude of the disturbance mode (m,n), $k_z^{(+)}$ is the axial wavenumber of a positive z-direction traveling or decaying wave, and M_d and N_d are the number of m and n modes included in the disturbance. The indexes m and n refer to circumferential and radial modes, respectively. The propagation characteristics of the modes are given by the axial wavenumber $k_z^{(+)}$ (see equations (A.21) and (A.22)).

The average pressure over the piston source located at (a,θ_n,z_n) due to the disturbance is given by

$$\bar{p}_d(a,\theta_n,z_n)=\frac{1}{S_n}\int_{z_n-d}^{z_n+d}\int_{\theta_n-\alpha}^{\theta_n+\alpha}p_d(a,\theta,z)ad\theta dz \tag{A.59}$$

Replacing equation (A.58) into (A.59) and solving the integral gives

$$\begin{aligned}\bar{p}_d\left(a,\theta_n,z_n\right)=&\sum_{m=0}^{M_d}\sum_{n=0}^{N_d}\left(A_{mn}^d\right)^{pos}J_m\left(k_{mn}a\right)e^{-ik_z^{(+)}z_n}\frac{\sin m\alpha}{m\alpha}e^{-im\theta_n}\frac{\sin\left(k_z^{(+)}d\right)}{k_z^{(+)}d}\\&\sum_{m=0}^{M_d}\sum_{n=0}^{N_d}\left(A_{mn}^d\right)^{neg}J_m\left(k_{mn}a\right)e^{-ik_z^{(+)}z_n}\frac{\sin m\alpha}{m\alpha}e^{im\theta_n}\frac{\sin\left(k_z^{(+)}d\right)}{k_z^{(+)}d}\end{aligned} \tag{A.60}$$

A.5 HQ tubes dynamics

The dynamic model of the HQ tubes is developed in this section. The goal is to find an expression for the sound field inside each tube. The tube ends are considered to be piston sources with velocity v^t and pressure p^t, as shown in Figure A.5. The model of the sound field in a single tube was first developed in reference [1]. However, for the sake of completeness, it is again included here.

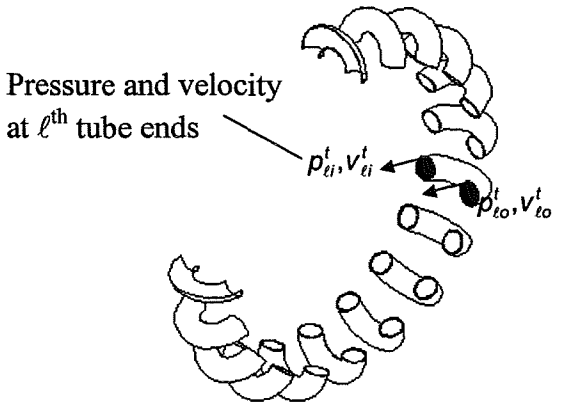

Figure A.5: Model of the HQ tubes.

In practice, the HQ tubes are constructed as a semi-circle or other smooth shapes. However, for modeling purposes they are considered as straight tubes with uniform cross-section as shown in Figure A.6. This assumption does not change the dynamic model of the tube since there are only plane waves propagating in the tube.

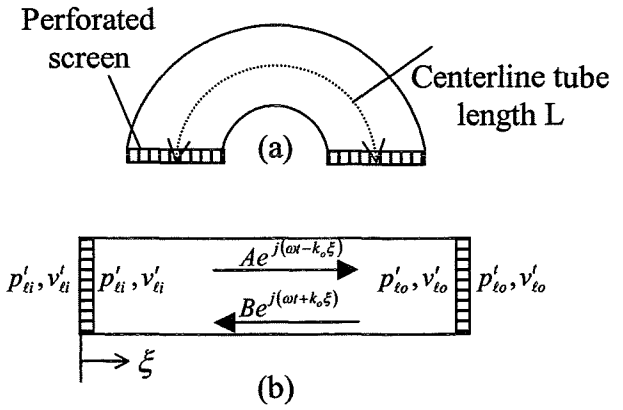

Figure A.6: (a) HQ tube representation. (b) Simplified model.

The sound field inside a tube is assumed to consist of plane waves only, a valid assumption well below the first cut-off frequency of the tube. It is also assumed that there is no flow in the tube. The sound field inside a tube is expressed in terms of a positive and a negative traveling plane wave of amplitude A and B, respectively. If ξ is the local tube coordinate, the pressure and particle velocity inside the tube are given as

$$p'(\xi,t) = Ae^{-ik_o\xi} + Be^{+ik_o\xi} \tag{A.61}$$

$$v'(\xi,t) = \frac{Ae^{-ik_o\xi} - Be^{+ik_o\xi}}{\rho c} \tag{A.62}$$

The acoustic pressure and particle velocity at the ends of the ℓ^{th} tube are expressed in the following matrix form

$$\begin{Bmatrix} p'_{\ell i} \\ \rho c v'_{\ell i} \end{Bmatrix} = [T_t] \begin{Bmatrix} p'_{\ell o} \\ \rho c v'_{\ell o} \end{Bmatrix} = \begin{bmatrix} \cos(k_o L) & i\sin(k_o L) \\ i\sin(k_o L) & \cos(k_o L) \end{bmatrix} \begin{Bmatrix} p'_{\ell o} \\ \rho c v'_{\ell o} \end{Bmatrix} \tag{A.63}$$

where L is the centerline length of the tubes and subscripts "i" and "o" refer to tube input and output, respectively. In practice, the tube is connected to the main duct through a perforated screen. This screen minimizes the potential for flow distortion (vortex shedding) due to the tube opening, which could create additional noise. The effect of these perforated screens is included as

$$\begin{Bmatrix} p^t_{\ell i} \\ \rho c v^t_{\ell i} \end{Bmatrix} = [T_{ps}] \begin{Bmatrix} p'_{\ell i} \\ \rho c v'_{\ell i} \end{Bmatrix} \text{ and } \begin{Bmatrix} p'_{\ell o} \\ \rho c v'_{\ell o} \end{Bmatrix} = [T_{ps}] \begin{Bmatrix} p^t_{\ell o} \\ \rho c v^t_{\ell o} \end{Bmatrix} \tag{A.64}$$

where the transfer matrix of the perforated screen T_{ps} is

$$[T_{ps}] = \begin{bmatrix} 1 & \dfrac{Z_{ps}}{\rho c} \\ 0 & 1 \end{bmatrix} \tag{A.65}$$

Z_{ps} is the impedance of the perforated screen written as [1]

$$Z_{ps} = i\frac{\omega\rho}{\sigma}\left(t_{ps} + 2a_{orif}\frac{8}{3\pi}\right) + \begin{cases} \dfrac{\sqrt{8\mu\rho\omega}}{\sigma}\left(1 + \dfrac{t_{ps}}{2a_{orif}}\right) & \text{linear model} \\ \dfrac{\rho v_{orif}}{\sigma} & \text{non-linear model} \end{cases} \tag{A.66}$$

where t_{ps} is the thickness of the screen, a_{orif} is the orifice radius, σ is the screen open area ratio, v_{orif} is the orifice fluid velocity (acoustic particle velocity divided by σ), ρ is the fluid density and μ is the viscosity coefficient. The linear model for the resistive part of the screen impedance is chosen for small orifice velocity, however if this velocity becomes higher than the critical value, a non-linear model has to be chosen. The critical value for the orifice velocity is given by the equation:

$$v_{orif} = \sqrt{\frac{f}{200}}\left(1 + \frac{t_{ps}}{2a_{orif}}\right) \tag{A.67}$$

where f is the frequency. In the present study, only the linear model will be used for the impedance of the perforated screen since the orifice velocity is small. Including the

effects of the perforated screens, the matrix that relates the pressure and particle velocity at the tube ends is thus

$$\begin{Bmatrix} p_{\ell i}^t \\ \rho c v_{\ell i}^t \end{Bmatrix} = \begin{bmatrix} T_{ps} \end{bmatrix} \begin{bmatrix} T_t \end{bmatrix} \begin{bmatrix} T_{ps} \end{bmatrix} \begin{Bmatrix} p_{\ell o}^t \\ \rho c v_{\ell o}^t \end{Bmatrix} = \begin{bmatrix} T_{11} & T_{12} \\ T_{21} & T_{22} \end{bmatrix} \begin{Bmatrix} p_{\ell o}^t \\ \rho c v_{\ell o}^t \end{Bmatrix} \tag{A.68}$$

Rearranging equation (A.68), the impedance matrix for the ℓ^{th} tube can be expressed as

$$\begin{Bmatrix} p_{\ell i}^t \\ p_{\ell o}^t \end{Bmatrix} = \rho c \begin{bmatrix} \dfrac{T_{11}}{T_{21}} & \dfrac{T_{12}T_{21} - T_{11}T_{22}}{T_{21}} \\ \dfrac{1}{T_{21}} & -\dfrac{T_{22}}{T_{21}} \end{bmatrix} \begin{Bmatrix} v_{\ell i}^t \\ v_{\ell o}^t \end{Bmatrix} = \begin{bmatrix} Z_{ii}^{t\ell} & Z_{io}^{t\ell} \\ Z_{oi}^{t\ell} & Z_{oo}^{t\ell} \end{bmatrix} \begin{Bmatrix} v_{\ell i}^t \\ v_{\ell o}^t \end{Bmatrix} \tag{A.69}$$

where the impedance matrix in (A.69) relates the pressure to the particle velocity at the two ends of the ℓ^{th} tube including the effect of the perforated screen.

It is important to note that in the process of matching the source velocity to the corresponding tube particle velocity, a consistent convention for the positive direction must be kept. To this end, the positive particle velocity in the entrance end of the tube at $\xi = 0$, which is opposite to the positive source velocity, is reversed by changing the sign of the first column of the matrix in (A.69). This will then yield

$$\begin{Bmatrix} p_{\ell i}^t \\ p_{\ell o}^t \end{Bmatrix} = \rho c \begin{bmatrix} -\dfrac{T_{11}}{T_{21}} & \dfrac{T_{12}T_{21} - T_{11}T_{22}}{T_{21}} \\ -\dfrac{1}{T_{21}} & -\dfrac{T_{22}}{T_{21}} \end{bmatrix} \begin{Bmatrix} v_{\ell i}^t \\ v_{\ell o}^t \end{Bmatrix} = \begin{bmatrix} Z_{ii}^{t\ell} & Z_{io}^{t\ell} \\ Z_{oi}^{t\ell} & Z_{oo}^{t\ell} \end{bmatrix} \begin{Bmatrix} v_{\ell i}^t \\ v_{\ell o}^t \end{Bmatrix} \tag{A.70}$$

Equation (A.70) gives the impedance matrix for the ℓ^{th} tube alone. Once the tubes are put together in a circumferential array around the duct, the average pressure over each source is written in matrix form as

$$\begin{Bmatrix} \overline{p}^t_{1i} \\ \overline{p}^t_{1o} \\ \vdots \\ \overline{p}^t_{\ell i} \\ \overline{p}^t_{\ell o} \\ \vdots \\ \overline{p}^t_{Ni} \\ \overline{p}^t_{No} \end{Bmatrix} = \begin{bmatrix} Z^{t1}_{ii} & Z^{t1}_{io} & 0 & 0 & \cdots & 0 & 0 \\ Z^{t1}_{oi} & Z^{t1}_{oo} & 0 & 0 & & 0 & 0 \\ 0 & 0 & & & & & \\ 0 & 0 & & & & & \\ & & & Z^{t\ell}_{ii} \; Z^{t\ell}_{io} & & & \\ & & & Z^{t\ell}_{oi} \; Z^{t\ell}_{oo} & & & \\ 0 & 0 & & & & Z^{tN}_{ii} & Z^{tN}_{io} \\ 0 & 0 & \cdots & & & Z^{tN}_{oi} & Z^{tN}_{oo} \end{bmatrix} \begin{Bmatrix} v^t_{1i} \\ v^t_{1o} \\ \vdots \\ v^t_{\ell i} \\ v^t_{\ell o} \\ \vdots \\ v^t_{Ni} \\ v^t_{No} \end{Bmatrix} \qquad \text{(A..71)}$$

The main impedance matrix consists of the impedance matrices of each HQ tube on its diagonal and of zeros everywhere else since there is no connection between the tubes.

A.6 Modal amplitudes and sound power radiation

The pressure field in the duct downstream of the HQ tubes, i.e. transmitted field, is computed by adding the pressure due to each piston source and due to the incident disturbance. That is

$$p_{trans}(r,\theta,z) = p_d(r,\theta,z) + \sum_{r=1}^{N_s} p\ (r,\theta,z|r_r,\theta_r,z_r) \qquad \text{(A.72)}$$

where the pressure due to the disturbance $p_d(r,\theta,z)$ is given in (A.58) and the pressure due to a unit velocity of the r^{th} source is obtained from equation (A.45) as

$$p\ (r,\theta,z|r_r,\theta_r,z_r) = \sum_{m=0}^{M_g}\sum_{n=0}^{N_g} (A^{(+)}_{mn})_r \cos m(\theta-\theta_r) J_m(k_{mn} r)\ e^{-ik_z^{(+)}z} \qquad \text{(A..73)}$$

The sound field created by the r^{th} piston source is non-spinning and symmetric with respect to $\theta=\theta_r$. However, it can be written as a set of positive and negative spinning modes by using the following trigonometric relationship

$$\cos m(\theta-\theta_r) = e^{-im\theta}\left(\frac{e^{im\theta_r}}{2}\right) + e^{im\theta}\left(\frac{e^{-im\theta_r}}{2}\right) \qquad \text{(A..74)}$$

Thus, equation (A.73) is written as

$$p\ (r,\theta,z|r_r,\theta_r,z_r) = \sum_{m=0}^{M_g}\sum_{n=0}^{N_g}(A_{mn}^{(+)})_r^{pos} J_m\left(k_{mn}r\right) e^{-im\theta} e^{-ik_z^{(+)}z} + \sum_{m=0}^{M_g}\sum_{n=0}^{N_g}(A_{mn}^{(+)})_r^{neg} J_m\left(k_{mn}r\right) e^{+im\theta} e^{-ik_z^{(+)}z} \quad \text{(A.75)}$$

where $\left(A_{mn}^{(+)}\right)_r^{pos}$ and $\left(A_{mn}^{(+)}\right)_r^{neg}$ are the complex amplitude of transmitted modes spinning in the positive and negative direction, respectively, due to source "*r*". These amplitudes are given as

$$(A_{mn}^{(+)})_r^{pos} = \frac{v_r k_o \rho c}{\pi a^2} \frac{J_m\left(k_{mn}a\right)}{\Lambda_{mn}(1-M^2)(k_z^{(+)}-k_z^{(-)})} \frac{2a\alpha_r \sin\left(m\alpha_r\right)}{m\alpha_r} \frac{2d_r \sin(k_z^{(+)}d_r)}{k_z^{(+)}d_r} e^{ik_z^{(+)}z_r} \frac{e^{+im\theta_r}}{2} \quad \text{(A.76)}$$

$$(A_{mn}^{(+)})_r^{neg} = \frac{v_r k_o \rho c}{\pi a^2} \frac{J_m\left(k_{mn}a\right)}{\Lambda_{mn}(1-M^2)(k_z^{(+)}-k_z^{(-)})} \frac{2a\alpha_r \sin\left(m\alpha_r\right)}{m\alpha_r} \frac{2d_r \sin(k_z^{(+)}d_r)}{k_z^{(+)}d_r} e^{ik_z^{(+)}z_r} \frac{e^{-im\theta_r}}{2} \quad \text{(A.77)}$$

The mode of circumferential order $m=0$ is not spinning; therefore, there is no use of defining positive and negative spinning amplitudes for this mode. However, in order to stay consistent with the previous notations and avoid presenting too many equations, it can simply be assumed that, for mode m=0, $(A_{0n}^{(+)})_r^{neg}$ is equal to zero and $(A_{0n}^{(+)})_r^{pos}$ is given by the equation

$$(A_{0n}^{(+)})_r^{pos} = \frac{v_r k_o \rho c}{\pi a^2} \frac{J_0\left(k_{0n}a\right)}{\Lambda_{0n}(1-M^2)(k_z^{(+)}-k_z^{(-)})} 2a\alpha_r \frac{2d_r \sin(k_z^{(+)}d_r)}{k_z^{(+)}d_r} e^{ik_z^{(+)}z_r} \quad \text{(A.78)}$$

Replacing (A.58) and (A.75) into (A.72), the transmitted pressure upstream of the tubes can be written as

$$p_{trans}(r,\theta,z) = \sum_{m=0}^{M_g}\sum_{n=0}^{N_g}(A_{mn}^{(+)})_{hq}^{pos} J_m\left(k_{mn}r\right)e^{-im\theta}e^{-ik_z^{(+)}z} + \sum_{m=0}^{M_g}\sum_{n=0}^{N_g}(A_{mn}^{(+)})_{hq}^{neg} J_m\left(k_{mn}r\right)e^{+im\theta}e^{-ik_z^{(+)}z} \quad \text{(A.79)}$$

where

$$(A_{mn}^{(+)})_{hq}^{pos} = \left(A_{mn}^{d}\right)^{pos} + \sum_{r=1}^{N_s}(A_{mn}^{(+)})_r^{pos} \quad \text{(A.80)}$$

$$(A_{mn}^{(+)})_{hq}^{neg} = \left(A_{mn}^{d}\right)^{neg} + \sum_{r=1}^{N_s}(A_{mn}^{(+)})_r^{neg} \quad \text{(A.81)}$$

are the modal amplitudes of the transmitted mode (m,n) spinning in positive and negative direction, respectively, due to all sources and A_{mn}^{d} is the amplitude of the modes included

in the disturbance (only positive spinning modes). The pressure reflected downstream of the HQ tubes can be similarly computed to give

$$p_{ref}(r,\theta,z)=\sum_{m=0}^{M_g}\sum_{n=0}^{N_g}(A_{mn}^{(-)})_{hq}^{pos}J_m\left(k_{mn}r\right)e^{-im\theta}e^{-ik_z^{(-)}z}+\sum_{m=0}^{M_g}\sum_{n=0}^{N_g}(A_{mn}^{(-)})_{hq}^{neg}J_m\left(k_{mn}r\right)e^{+im\theta}e^{-ik_z^{(-)}z} \quad \text{(A.82)}$$

where

$$(A_{mn}^{(-)})_{hq}^{pos}=\sum_{r=1}^{N_s}(A_{mn}^{(-)})_r^{pos} \quad \text{(A.83)}$$

$$(A_{mn}^{(-)})_{hq}^{neg}=\sum_{r=1}^{N_s}(A_{mn}^{(-)})_r^{neg} \quad \text{(A.84)}$$

are the amplitudes of the reflected mode (m,n), spinning in the positive and negative direction, respectively, due to the radiation of all sources. $\left(A_{mn}^{(-)}\right)_r^{pos}$ and $\left(A_{mn}^{(-)}\right)_r^{neg}$ are the amplitudes of mode (m,n) spinning in the positive and negative direction, respectively, due to an individual source "r" given as

$$(A_{mn}^{(-)})_r^{pos}=\frac{v_r k_o \rho c}{\pi a^2}\frac{J_m\left(k_{mn}a\right)}{\Lambda_{mn}(1-M^2)(k_z^{(+)}-k_z^{(-)})}\frac{2a\alpha_r\sin\left(m\alpha_r\right)}{m\alpha_r}\frac{2d_r\sin(k_z^{(-)}d_r)}{k_z^{(-)}d_r}e^{ik_z^{(-)}z_r}\frac{e^{+im\theta_r}}{2} \quad \text{(A.85)}$$

$$(A_{mn}^{(-)})_r^{neg}=\frac{v_r k_o \rho c}{\pi a^2}\frac{J_m\left(k_{mn}a\right)}{\Lambda_{mn}(1-M^2)(k_z^{(+)}-k_z^{(-)})}\frac{2a\alpha_r\sin\left(m\alpha_r\right)}{m\alpha_r}\frac{2d_r\sin(k_z^{(-)}d_r)}{k_z^{(-)}d_r}e^{ik_z^{(-)}z_r}\frac{e^{-im\theta_r}}{2} \quad \text{(A.86)}$$

The radiated sound power can now be computed. To this end, the acoustic intensity in the z-direction is written as

$$I_z=\frac{1}{2}Real\left[pv_z^*+\rho c|v_z|^2M+\frac{|p|^2}{\rho c}M+v_z p^* M^2\right] \quad \text{(A.87)}$$

or

$$I_z=\frac{1}{2}\left\{Real\left[pv_z^*\right](1+M^2)+\rho cM|v_z|^2+\frac{M}{\rho c}|p|^2\right\} \quad \text{(A.88)}$$

where v_z is the particle velocity in the z-direction and asterisk (*) denotes complex conjugate. To compute the intensity, the particle velocity in the z-direction is obtained from Euler's equation as

$$-\frac{\partial p}{\partial z}=i\omega\rho v_z+\rho cM\frac{\partial v_z}{\partial z} \quad \text{(A.89)}$$

Since, the particle velocity is given as

$$v_z(r,\theta,z) = v_z(r,\theta)e^{-ik_z^{(+)}z} \tag{A.90}$$

equation (A.89) becomes

$$-\frac{\partial p}{\partial z} = i\rho c\left(k_o - k_z^{(+)}M\right)v_z(r,\theta)e^{-ik_z^{(+)}z} \tag{A.91}$$

that can be solved for the particle velocity as

$$v_z(r,\theta,z) = -\frac{1}{i\rho c\left(k_o - k_z^{(+)}M\right)}\frac{\partial p}{\partial z} \tag{A.92}$$

Replacing the transmitted pressure from (A.79) into (A.92) results

$$\begin{aligned} v_z(r,\theta,z) = &\sum_{m=0}^{M_g}\sum_{n=0}^{N_g}\frac{\left(A_{mn}^{(+)}\right)_{hq}^{pos} J_m(k_{mn}r)e^{-im\theta}k_z^{(+)}e^{-ik_z^{(+)}z}}{\rho c\left(k_o - k_z^{(+)}M\right)} \\ &+\sum_{m=0}^{M_g}\sum_{n=0}^{N_g}\frac{\left(A_{mn}^{(+)}\right)_{hq}^{neg} J_m(k_{mn}r)e^{+im\theta}k_z^{(+)}e^{-ik_z^{(+)}z}}{\rho c\left(k_o - k_z^{(+)}M\right)} \end{aligned} \tag{A.93}$$

The acoustic power is obtained by integrating the intensity over the cross sectional area of the duct as

$$W = \int_0^a\int_0^{2\pi} I_z r dr d\theta \tag{A.94}$$

Replacing (A.79) and (A.93) into (A.88) and this into (A.94) and considering the orthogonality condition of the modes

$$\int_0^{2\pi}\int_0^a J_m^2(k_{mn}r)\, r dr d\theta = 2\pi a^2 \Lambda_{mn} \tag{A.95}$$

$$\Lambda_{mn} = \begin{cases} \dfrac{1}{2}J_m^2(k_{mn}a) & \text{if} \quad m = 0 \\ \dfrac{1}{2}\left[1 - \dfrac{m^2}{(k_{mn}a)^2}\right]J_m^2(k_{mn}a) & \text{if} \quad m \neq 0 \end{cases} \tag{A.96}$$

results in the total transmitted power to be given as

$$W = \sum_{m=0}^{M_g} \sum_{n=0}^{N_g} W_{mn}^{T} \tag{A.97}$$

Therefore, the total sound power transmitted upstream of the HQ system is expressed in terms of the modal amplitudes as

$$\begin{aligned} W_{mn}^{T} = & \frac{\pi a^2 \Lambda_{mn}}{\rho c} \left(\left| \left(A_{mn}^{(+)} \right)_{hq}^{pos} \right|^2 + \left| \left(A_{mn}^{(+)} \right)_{hq}^{neg} \right|^2 \right) \\ & \times \left\{ \left(1 + M^2\right) Real \left[\frac{\left(k_z^{(+)}\right)}{\left(k_o - k_z^{(+)} M\right)} \right] + \frac{M \left| k_z^{(+)} \right|^2}{\left| k_o - k_z^{(+)} M \right|^2} + M \right\} \end{aligned} \tag{A.98}$$

REPORT DOCUMENTATION PAGE

Form Approved
OMB No. 0704-0188

1. AGENCY USE ONLY *(Leave blank)*	2. REPORT DATE	3. REPORT TYPE AND DATES COVERED
	March 2002	Contractor Report

4. TITLE AND SUBTITLE
Analytical Modeling of Herschel-Quincke Concept Applied to Inlet Turbofan Engines

5. FUNDING NUMBERS
G NAG1-2137
WU 706-81-12-01

6. AUTHOR(S)
Raphael F. Hallez
Ricardo A. Burdisso

7. PERFORMING ORGANIZATION NAME(S) AND ADDRESS(ES)
Virginia Polytechnic Institute and State University
Department of Mechanical Engineering
Blacksburg, VA 24061

8. PERFORMING ORGANIZATION REPORT NUMBER
VPI-ENGR 4-26483

9. SPONSORING/MONITORING AGENCY NAME(S) AND ADDRESS(ES)
National Aeronautics and Space Administration
Langley Research Center
Hampton, VA 23681-2199

10. SPONSORING/MONITORING AGENCY REPORT NUMBER
NASA/CR-2002-211429

11. SUPPLEMENTARY NOTES
NASA Langley Technical Monitor: Carl H. Gerhold

12a. DISTRIBUTION/AVAILABILITY STATEMENT
Unclassified–Unlimited
Subject Category 71 Distribution: Nonstandard
Availability: NASA CASI (301) 621-0390

12b. DISTRIBUTION CODE

13. ABSTRACT *(Maximum 200 words)*
This report summarizes the key results obtained by the Vibration and Acoustics Laboratories at Virginia Tech over the period from January 1999 to December 2000 on the project "Investigation of an Adaptive Herschel-Quincke Tube Concept for the Reduction of Tonal and Broadband Noise from Turbofan Engines", funded by NASA Langley Research Center. The Herschel-Quincke (HQ) tube concept is a developing technique the consists of circumferential arrays of tubes around the duct. The analytical model is developed to provide prediction and design guidelines for application of the HQ concept to turbofan engine inlets. An infinite duct model is developed and used to provide insight into attenuation mechanisms and design strategies. Based on this early model, the NASA-developed TBIEM3D code is modified for the HQ system. This model allows for investigation of the HQ system combined with a passive liner.

14. SUBJECT TERMS	15. NUMBER OF PAGES
duct propagation, analytical model, turbofan, Herschel-Quincke tube	104
	16. PRICE CODE

17. SECURITY CLASSIFICATION OF REPORT	18. SECURITY CLASSIFICATION OF THIS PAGE	19. SECURITY CLASSIFICATION OF ABSTRACT	20. LIMITATION OF ABSTRACT
Unclassified	Unclassified	Unclassified	UL